5-2018

Particle Streak Velocimetry: A Diagnostic for High Speed Flows

Jared D. Willits
Purdue University

PARTICLE STREAK VELOCIMETRY: A DIAGNOSTIC FOR HIGH SPEED FLOWS

by

Jared D. Willits

A Dissertation

Submitted to the Faculty of Purdue University

In Partial Fulfillment of the Requirements for the degree of

Doctor of Philosophy

School of Aeronautics & Astronautics

West Lafayette, Indiana

May 2018

THE PURDUE UNIVERSITY GRADUATE SCHOOL
STATEMENT OF COMMITTEE APPROVAL

Dr. Timothée L. Pourpoint, Chair
Department of Aeronautics and Astronautics
Dr. Stephen D. Heister
Department of Aeronautics and Astronautics
Dr. Terrence R. Meyer
Department of Aeronautics and Astronautics
Dr. William E. Anderson
Department of Aeronautics and Astronautics

Approved by:
Dr. Weinong W. Chen
Head of the Graduate Program

To my wife, Allison. You push me every day to reach my potential. Your love and encouragement are the foundation for me to stand on through the struggles and successes of this journey and those to come. Everything I have and will accomplish is only possible with you beside me.
And to my parents, Calvin and Tammy, you gave me every resource and unending encouragement to succeed. I will always put it to the best use I can.

ACKNOWLEDGMENTS

I owe my sincerest gratitude to my advisor, Dr. Timothée Pourpoint. You encouraged me to pursue my master's degree out of our interactions in your design, build, test class and then to continue on to a Ph.D. two years later so that we could realize this goal. Your guidance and patience have made me a better student, engineer, and researcher, and I will carry that forward with me wherever I go.

Thank you to my committee for your directions and advice through this process, and thank you to all of the other faculty and staff at Zucrow who make it such an amazing place for students to work and learn.

To the supporting staff within our group, you were essential to overcoming so many hurdles and discovering new ways to build-up and expand this work. Thank you to Jason Gabl, Dr. Robert Orth, Dr. Trenton Parsell, Dr. Michael Drolet, David McMillan, and Benjamin Whitehead. And thank you to my mentors during my on-site experiences at NASA, Chris Burnside and Kevin Pederson, for teaching me from a perspective beyond the lab and classroom. Those first steps out of the comfort and familiarity of Purdue gave me invaluable perspective towards my strengths and weaknesses.

Many students have come and gone from Zucrow who have helped me review designs and analyses, run tests, manufacture parts, or just learn how to use all of the equipment needed for this work. Thank you to Dr. Jacob Dennis, Jonathan Chrzanowski, Chris Zaseck, Brandon Terry, Joshua Mathews, Alicia Benhidjeb-Carayon, Logan Kamperschroer, John Ellis, Jeremy Marcum, Rufat Kulakhmetov, Michael Orth, Taylor Groom, Michael Lagrange, Noah Gold, and everyone else from the group who lent a hand along the way or built up the infrastructure I was fortunate to make use of.

A final thank you to the NASA Space Technology Mission Directorate who funded this work through a NASA Space Technology Research Fellowship.

TABLE OF CONTENTS

LIST OF TABLES

LIST OF FIGURES

NOMENCLATURE

A	= area	[m^2]	r	= resistance	[Ω]
B	= Stokes drag correction factor	[-]	T	= temperature	[K]
a	= acceleration	[m/s^2]	t	= time	[s]
C	= capacitance	[F]	t_s	= temporal scaling factor	[μs/pixel]
C_D	= drag coefficient	[-]	V	= capacitor voltage	[V]
c_p	= heat capacity	[J/K-kg]	v	= velocity	[m/s]
d	= diameter	[m]	W	= discharge power	[W]
E	= lamp discharge energy	[J]	w	= helium mass fraction	[-]
F_D	= drag force	[N]	x	= axial position within nozzle	[m]
f	= frequency	[cyc/pix]	y_s	= spatial scaling factor	[μm/pixel]
h	= distance from nozzle exit	[m]	z	= Mie size parameter	[-]
i	= current	[A]			
K	= lamp impedance parameter	[Ω-$A^{.5}$]	α	= Stokes drag time constant	[s]
L	= inductance	[H]	γ	= ratio of specific heats	[-]
l	= length	[m]	ε	= uncertainty	[-]
M	= Mach number	[-]	ζ	= damping factor	[-]
MW	= molecular weight	[kg/kmol]	η	= cyclone filtering efficiency	[-]
m	= particle mass	[kg]	θ	= angle	[°]
m_{st}	= streak slope	[pixel/pixel]	λ	= wavelength	[m]
$\dot{m}$	= mass flow rate	[kg/s]	μ	= viscosity	[Pa-s]
N	= window size	[m]	ξ	= Riccati-Bessel function of $h_k^{(1)}$	[-]
n	= refractive index	[-]	π_k	= Mie angle dependent function	[-]
P	= pressure	[Pa or Psi]	ρ	= density	[kg/m^3]
p	= Mie scattering coefficient	[-]	τ_{FL}	= discharge peak duration	[s]
Q	= volumetric flowrate	[m^3/s]	τ_k	= Mie angle dependent function	[-]
q	= Mie scattering coefficient	[-]	Υ	= root discriminant of ODE	[-]
R	= specific gas constant	[J/K-kg]	ϕ	= particle to flow velocity ratio	[-]
Re	= Reynolds number	[-]	ψ	= Riccati-Bessel function of j_k	[-]
Ru	= universal gas constant	[J/K-kmol]	ω	= relative refractive index	[-]

Other subscripts

0 : stagnation condition
bo : cyclone block outlet
c : nominal cyclone cylinder
cy : cyclone contraction
e : nozzle exit
f : fluid
FL : flashlamp
h : cyclone inlet height
i : iterative index
k : iterative index
M : Mach wave
m : gas mixture
p : particle
po : cyclone pass outlet
S : Mie scatter
se : seeder
st : streak
t : throat
w : cyclone inlet width

ABSTRACT

Author: Willits, Jared D. PhD
Institution: Purdue University
Degree Received: May 2018
Title: Particle Streak Velocimetry: A Diagnostic for High Speed Flows
Major Professor: Timothée L. Pourpoint

This work describes the development and implementation of a novel velocimetry technique to probe the exhaust flow of a cold gas thruster. The diagnostic combines the advantages of standard particle velocimetry techniques and the ultra-fast imaging capabilities of a streak camera to probe high speed flows near continuously with improved spatial and velocity resolution compared to Particle Image Velocimetry. This "Particle Streak Velocimetry" technique tracks illuminated seed particles at up to 4.2 GHz allowing time-resolved measurement of one-dimensional flows exceeding 2000 m/s as are found in rocket nozzles and many other applications (US Provisional Patent filed 05/19/16). Single frame images containing multiple streaks are analyzed to find the slope of each incident particle. Tests with inert gas have been performed to validate and develop the technique in supersonic flows without background noise due to combustion. Exhaust centerline flow velocities of a cold gas nozzle flowing pure nitrogen have been probed with 300 nm titanium dioxide seed particles and a 450 nm, continuous-wave laser diode. Measured velocities on the order of 500 m/s were validated against schlieren images of the plume and stagnation temperature measurements, which can also be correlated to velocity for known flow compositions. Further tests using a mixture of helium and nitrogen have been performed with measured velocities of over 1100 m/s that are shown to agree with predicted behavior from isentropic flow analyses.

1. INTRODUCTION

The following chapter explains the motivations for completing the work described in this dissertation. Flow and combustion diagnostics are ever improving, and the specific objectives to aid that progression with a new technique are provided.

1.1 Motivation

Advancements in combustion diagnostics strive to evaluate technologies at the most fundamental scale. The ability to break down components and assess performance at the foundation as opposed to broad, system-level characterizations leads to improved performance, more efficient and focused testing, and enhanced model development. Reaching these principle measurements often drives diagnostics towards higher time resolution and broader detectable scales. As high-speed technologies in the propulsion field develop, the need arises to expand velocimetry measurements beyond the kilohertz temporal range and also into high-temperature, supersonic velocity scales. As examples, new rocket engine architectures with new fuel formulations [1] [2] [3] [4], scramjets [5] [6], and detonation engines [7] are among current technology focuses where such expanded capabilities would provide substantial benefit in aiding validation against theoretical combustion models. The ability to evaluate interactions between a hypersonic inlet flow and the flow field in a scramjet combustor is essential to optimize fuel injection and flame holding components [8]. Likewise, the means by which a local detonation wave can be harnessed by some adaptation of a diverging nozzle to extract maximum thrust is not well understood in detonation engines [9] [10]. Temporally resolved probing of rotating and pulse detonation engine exhaust would inform such nozzle development. Diagnostic capabilities to capture both transient and high-speed flow phenomena are a key element to understanding the governing principles and best utilization of these and many other flow fields. Work detailed in this dissertation focuses on developmental testing of such a diagnostic method to measure nozzle exhaust velocity starting with a cold gas thruster but that could ideally be adapted to provide additional insight into the aforementioned applications.

1.2 Research Objectives

Particle Streak Velocimetry (PSV) is being developed to track illuminated seed particles near continuously in one dimension, which will allow interrogation of high speed flows. The specific objectives to reach this goal are to:

1. Develop a seed delivery system by
    (a) Identifying high melting temperature, high index of refraction seed materials which can be acquired in sub-micron sizes at sufficient quantities,
    (b) Modeling the lag response of particles in the defined flow field based on their density and diameter,
    (c) Building a filtering device to introduce only particles small enough to show low velocity lag relative to the flow, and
    (d) Evaluating delivered seed frequency and size via scanning electron microscope (SEM) images of tape samples swept across the flow.
2. Identify a long pulse or continuous, high power light source capable of illuminating small particles for the measurement duration.
3. Characterize and optimize the streak camera and collection optics used to record the measurement by
    (a) Identifying the necessary components that provide enough degrees of freedom to efficiently capture the scattered light, and
    (b) Expanding and assessing the operational bounds of the streak camera in imaging a one-dimensional measurement region in space.
4. Perform developmental tests of the proposed velocimetry technique to
    (a) Predict exit velocities of the nozzle based on isentropic flow principles,
    (b) Test with nitrogen as a low speed medium,
    (c) Compare results to a proven method for known flow composition and properties, specifically schlieren,
    (d) Test with helium to increase flow velocity and evaluate the range of the PSV technique.

2. BACKGROUND

This chapter discusses velocimetry measurements and some limiting factors in high velocity experiments. It then introduces the fundamental models for the particular experiment and diagnostic being studied. It describes operating principles of the major hardware components and an introduction to the processing of the acquired data.

2.1 Traditional Velocimetry

Several options exist to obtain a flow velocity measurement [11] [12]. Intrusive methods include hotwire anemometry [13], Pitot-static probes, and turbines among others. Due to material constraints, these are generally not viable for high temperature and corrosive flows characteristic of rocket exhausts. Non-intrusive, or minimally so, methods rely on optical techniques often involving high-speed cameras and powerful lasers. Examples include: schlieren imaging where gradients in refractive index can be visualized by passing a collimated beam through the flow [14], Doppler where the spectral shift from a stimulated flame emission or an illuminated particle is recorded [15], and visual object tracking techniques such as Particle Image Velocimetry (PIV) [16] [17] where a seed material either present or added to the flow is illuminated in successive frame pairs or Hydroxyl Tagging Velocimetry (HTV) where the tracer object is generated in-situ by dissociating water present in the flow and exciting the hydroxyl radical causing it to fluoresce [18] [19].

A key distinction among the non-intrusive methods is the requirement of known flow composition. Features observed by schlieren can provide Mach number, but still require the context of molecular composition and temperature information to convert to velocity. Doppler methods using laser excitation techniques such as Raman spectroscopy are referenced to emission wavelengths of specific species in the exhaust. In contrast, seeded techniques require less stringent knowledge of flow properties making them more ideal for investigation of wholly new propellant formulations or evolving reactions. Particles must simply be sized such that the velocity lag relative to length and time scales in the flow of interest is sufficiently small. Provided that background flame

emissions can be filtered out from the seed signal, seeded techniques can be applied in the exact same manner irrespective of the exhaust plume composition.

For seeded flows, the resolvable length scales and velocities are highly coupled. In PIV, the window length is governed by the maximum velocity to be resolved and the time step between frames, provided the pixel resolution is sufficiently scaled to populate the windows. A conventional metric for PIV, to avoid aliasing, is that the interrogation window must be at least four times larger than the particle displacement across one frame pair [20]. Figure 1 demonstrates how for shorter windows, the likelihood of a particle moving back out of the window before the second image can be captured is high. The image shows an ideal scenario where the particle is initially just within the window edge, but since PIV samples are analyzed for clusters of several particles, a random starting distribution within the window would lead to half or more of the particles exiting the window and entering the next for the first three cases. This would prohibit calculation of the particle shift between the two time exposures. A lower bound of the window length is relevant because the measured velocity is averaged across an entire window. The acceleration of the flow relative to that window length must be constant or linear to produce an accurate mean value at the window center. Otherwise, the tabulated velocities will undergo a smoothing effect and the detailed features cannot be fully resolved.

Pulsed illumination sources can easily reach down to sub-nanosecond separation time, but the shutter speed of commercially available, cutting-edge cameras used to image such flows is typically limited to between 100 and 500 ns [21] [22] [23] at the very best, and this value sets the window length limit. For a theoretical flow of 3000 m/s (relevant to rocket exhaust diagnostics) and a frame pair separation of 250 ns, the minimum window size by the recommended metric would be 3 mm. Indeed, several projects have reported measured velocities with 630 m/s [17], 1,000 m/s [24], 1,500 m/s [25], and even 2,500 m/s [26] using PIV. Spatial resolutions achieved for the latter experiments were 2.5 mm, 3.1 mm, and 1.8 mm respectively using computational cross-correlation techniques between windows. Whether this is sufficient depends entirely on the feature or flow area being analyzed.

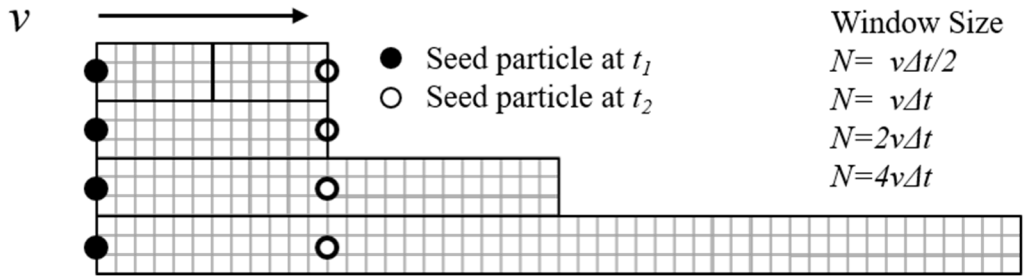

Figure 1. Window Length Relative to Particle Displacement in PIV

2.2 Particle Streak Velocimetry

A novel adaptation of PIV using a streak camera is presented to provide superior velocity limits at the spatial scales required for the exhaust measurement described above. Streak cameras are used to track objects at high velocity in one spatial dimension. On a single CCD frame, the signal on the y-axis is swept across the x-axis at a controlled rate and the effective time step is governed by the dwell time on each pixel [27]. If the y-axis represents a line in space, the slope of the streak signal represents velocity. Streak cameras are traditionally applied to single macroscopic objects such as projectiles [28] and detonation waves [29] or to dispersed spectra of reacting fields [30]. Alternatively, Lawhead [31] [32] provides a study of the overall flow dynamics in a liquid rocket engine using the analog precursor to the digital streak camera. By imaging the field of combusting liquid droplets in the flow, he attempts to characterize spatially dependent gas velocities along the chamber axis and pressure waves caused by instability modes within the chamber.

The PSV technique implemented in this work uses the digital streak camera to track small, inert seed particles introduced to the flow and illuminated by a laser to infer 1-D flow velocity, much in the same manner as PIV. However, through this method, frame straddling of the camera shutter is eliminated, and pulsed laser repetition rate is no longer a factor. The streak camera allows for a single exposure from a continuous light source rather than a dual-pulsed system. In traditional PIV, cameras with sufficient shutter speed can be acquired with sample rates exceeding 1 MHz (at drastically reduced spatial resolution); however, most pulsed laser systems are limited to the 10 kHz range. Experimental work is ongoing to provide bursts of 500 kHz [33] or even 1 MHz [34] pulse trains in a pursuit of Time-Resolved PIV (TR-PIV). By comparison, with a continuous light source, the streak system utilized in this work can operate with effective 1-D sampling rates

from 40 kHz up to 4.2 GHz based on the programmed sweep speeds and pixels allocated on the CCD in the time dimension. This clearly serves the purpose of allowing visualization of faster transient events within the flow structure. Equally as important though, as discussed in the previous section, the streak sweep can be tuned to the given velocity range such that the displacement of the particle across successive samples is one pixel or even lower. The streak sampling rate, analogous to the camera shutter speed, is essentially the inverse of the per sample exposure rate, and at time steps as low as 236 ps, this virtually eliminates the window length limit described for PIV.

With near continuous racking, seeding density can also be lowered as each particle is a sample rather than each filled window. While not a considerable impact in most situations, seed does remove momentum from the carrying flow and a reduction of this effect would reduce intrusion of the measurement. The auxiliary flow rate needed to carry the seed into the test volume may also be reduced which helps preserve the chemical kinetics in reacting flows.

2.3 Flow Behavior and Particle Response

2.3.1 Particle Lag Model

Velocity lag between the flow of interest and seed particles contributes to uncertainty and dictates the length scale of resolvable features such as shocks, boundary layers, eddies, etc. In regard to this experiment, the nozzle must be proven adequate to accelerate the particle to a sufficient fraction of the exit velocity. Seed particle density and diameter must be carefully selected as they affect the degree of acceleration or deceleration under Stokes flow along with the local flow fluid properties [35].

Gilbert [36] describes how particle response can be modeled by iterative application of Stokes drag along a 1-D, linearly accelerating flow. While Gilbert was limited to segmenting a converging-diverging nozzle flow into only three linear regions, modern computers allow a much higher fidelity solution to be easily generated for a particle moving through the domain. At each time step, the program uses isentropic flow to calculate the local Mach number based on the nozzle area at the current location (x_i). Using inputted stagnation properties, the viscosity, density, and speed

of sound can then be used to determine the instantaneous drag force imposed on the accelerating particle in Equation 1. Assuming the time step is sufficiently short to treat the force as constant, the new location of the particle can be calculated. Equation 2 shows the solution to the governing equation over a step in which the flow is linearly accelerating and provides the essential framework of the model when combined with Equation 3. For simplicity, Equations 4 and 5 define the root discriminant (Υ) obtained when solving the second order differential equation from Equation 1 and the time constant (α) derived from Stokes flow for drag on a spherical particle at low Reynolds number (Re).

Key parameters include flow and particle velocity (v_f) and (v_p), the ratio of particle to flow velocity (ϕ), and a correction factor for Stokes drag at increased Reynolds number (B). A full derivation of Equation 2 from basic principles and the code are provided in Appendix C.

$$F_D = m_p \; _p = - \; _D \; _p \rho_f (v_f - v_p) \tag{1}$$

$$v_p = v_f e^{-\frac{\Delta t}{\alpha}} \left[\phi \cosh\left(\frac{t\Upsilon}{\alpha}\right) + \frac{-\phi}{\Upsilon} \sinh\left(\frac{t\Upsilon}{\alpha}\right) \right] \tag{2}$$

$$x_{i+} \; = x_i + v_p \Delta t \tag{3}$$

$$\Upsilon = \sqrt{1 + 2\alpha \frac{dv_f}{dx}\Big|_{x_i}} \tag{4}$$

$$\alpha = B \frac{\rho_p d_p}{9\mu} \tag{5}$$

$$B = \begin{cases} \frac{50}{75Re^{.15}+3Re} & 1 < Re < 2000 \\ 1 & Re \leq 1 \end{cases} \tag{6}$$

$$Re = \frac{\rho_f d_p}{\mu}\left(v_f(x_{i-}) - v_p(x_{i-})\right) \quad 7$$

For a given nozzle geometry, the gas velocity is solved numerically by the area ratio at each location assuming 1-D isentropic flow with knowledge of flow stagnation temperature and ratio of specific heats. This analysis provides an order of magnitude estimation for velocity uncertainty to inform the selection of candidate particle materials and diameters.

Figure 2 shows the nozzle contour with a 4.6 mm throat diameter (d_t) and 5.7 mm exit diameter (d_e) overlain with the corresponding Mach profile derived from the area ratio. Simulations of particles traveling through the center axis were run for a variety of seed materials from 300 to 1500 nm diameters in nitrogen and helium. Figure 3 shows a sample output of the Reynolds number for a representative SiO_2 particle with 1 μm diameter in N_2. Though *Re* does exceed the range for traditional Stokes drag, it remains well within the range for the correction factor used in Equation 5. Nuances occur for faster accelerating flows, different particle sizes, and different fluid properties, but generally, the validity of this correction factor for the experiments presented here is maintained due to the overall goal of particle lag sizing which is to decrease particle size (and thus *Re*) until only small deviations from the local flow velocity are seen.

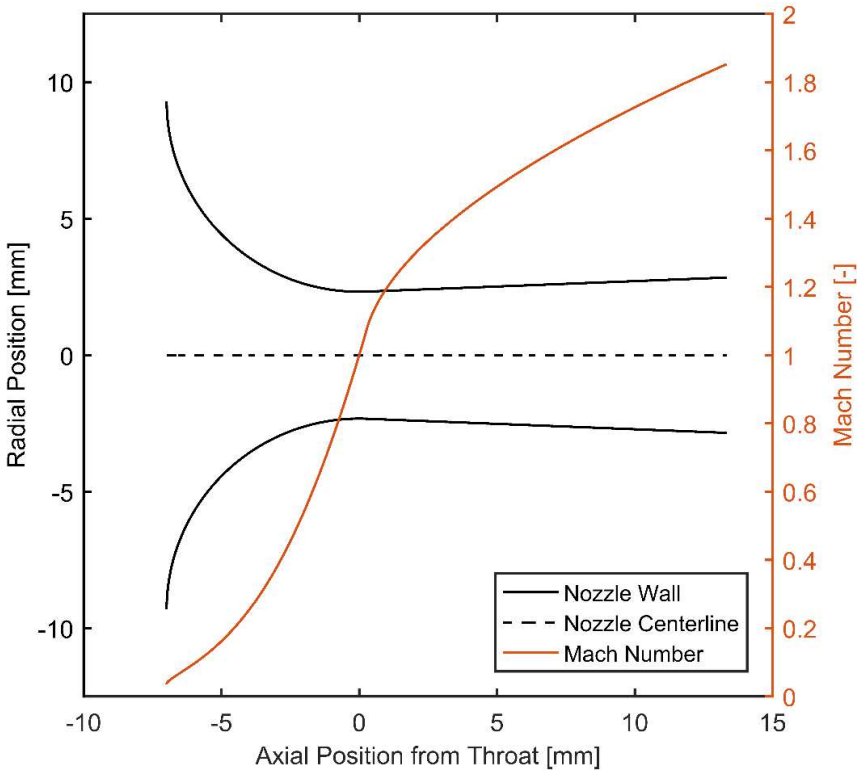

Figure 2. Expanding Nozzle Contour and Mach Number

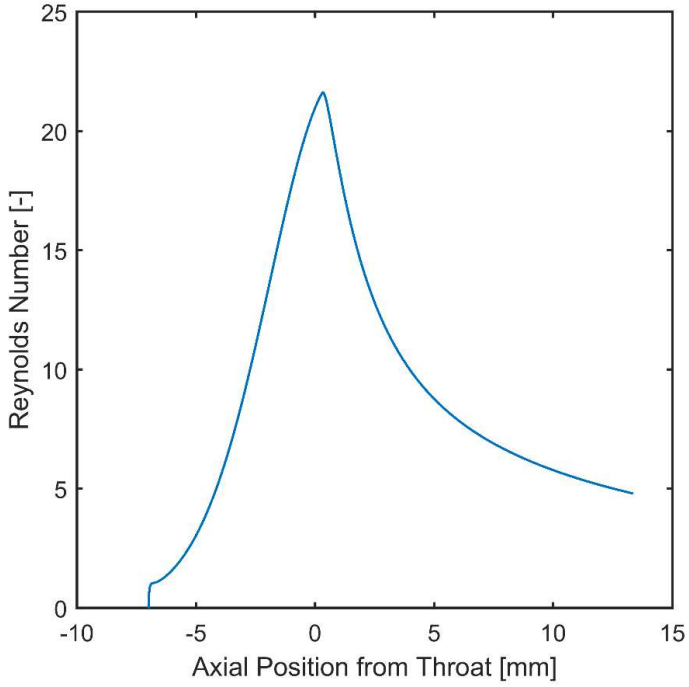

Figure 3. Reynolds Number for 1 μm SiO_2 Particle in N_2 through Nozzle

The time step (Δt) used in Equations 2 and 3 must be small enough to approximate the flow velocity as linearly accelerating with respect to x in Equation 4 (i.e. dv_f/dx is constant). An analysis of mesh convergence for Δt was performed for the case of 300 nm TiO_2 in nitrogen. Time steps of 0.1, 1, 10, and 100 ns were compared. The error in ϕ relative to the 0.1 ns model was used to quantify each mesh's suitability. This error is displayed in Figure 4 and the exit and maxima results are summarized in Table 1. The 10 ns model was deemed suitably accurate to use as a first approximation when surveying potential powder materials and sizes while running in a reasonable amount of time.

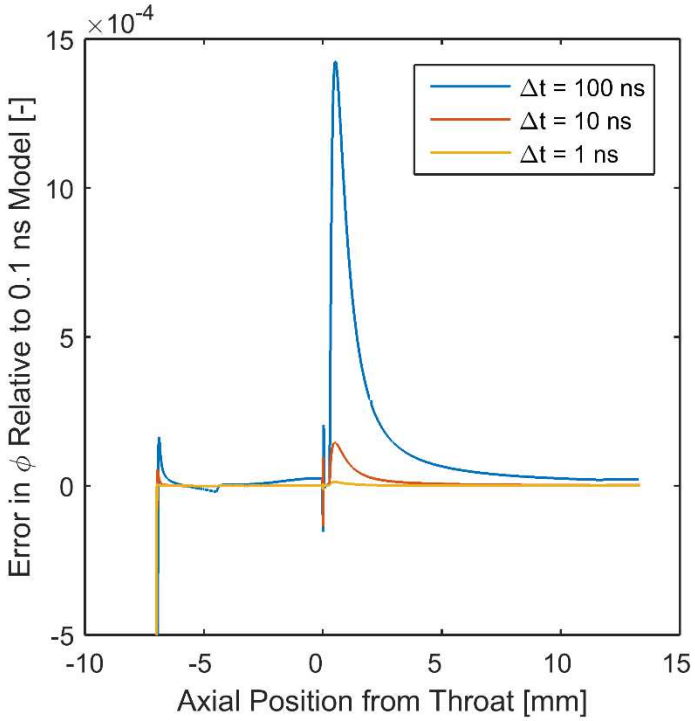

Figure 4. Time Step Sensitivity Plot for Particle Lag Model

Table 1. Time Step Sensitivity Results for Particle Lag Model

Δt [ns]	Max Error [-]	Error at Exit [-]
100	1.43E-3	2.15E-5
10	1.47E-4	2.13E-6
1	1.31E-5	1.95E-7

2.3.2 Gas Mixture Isentropic Flow Model

To develop PSV at velocities beyond that of the cold gas nitrogen flow, helium is used to supplement the nozzle flow due to its higher speed of sound. However, as described later, nitrogen is still used as the carrier gas for the particle seeder. In order to predict the resultant expected velocity based on the available instrumentation data, a system of equations is defined to calculate the total mass flow through the nozzle as a function of the mass fraction (w) of the constituent gases and the measured mixture stagnation properties. Equations 8 to 13 describe how the specific gas constant (R) and ratio of specific heats (γ) are mass averaged to solve the remaining isentropic flow equations. Equation 12 is solved for Mach number (M) using a root finding function after the known nozzle expansion ratio is subtracted.

Mass flow data for the nitrogen can be determined from state data in the seeder and a sonically choked orifice feeding into the bulk helium flow. Identifying the intersection with the model calculated for w from 0 to 1 allows exit velocity to be calculated from γ for the mixture. Figure 5 shows the range of potential mass flows for the mixture, helium, and nitrogen at each mixture ratio and the circled point corresponds to where it intersects with the mass flow calculated from measured data for the nitrogen seeder at the given state. The mass fraction of helium to choke the nozzle would be would be 74% in this instance. Figure 6 displays the corresponding exit velocities based on the isentropic expansion of the mixture through the known nozzle dimensions. The same mass fraction is again denoted by the circle, at which point the exit velocity is 1141 m/s.

$$w = \frac{\dot{m}_{He}}{\dot{m}_{tot}} \tag{8}$$

$$R_m = R_{He}w + R_N\ (1-w) \tag{9}$$

$$\gamma_m = \frac{}{-\frac{R_m}{c_{pHe}w + c_{pN2}(1-w)}} \tag{10}$$

$$\dot{m}_{tot} = \frac{\pi d_t^2 P_0}{4R_m T_0}\left(1 + \frac{\gamma_m -}{}\right)^{\frac{1}{1-\gamma_m}} \sqrt{\frac{\gamma_m R_m T_0}{+\frac{\gamma_m - 1}{2}}} \tag{11}$$

$$\frac{A_e}{A_t} = \frac{\left(\frac{2}{\gamma_m + 1}\left(+ \frac{\gamma_m - 1}{2} M_e^2\right)\right)^{\frac{\gamma_m + 1}{2(\gamma_m - 1)}}}{M_e} \tag{12}$$

$$v_e = M_e \sqrt{\frac{\gamma_m R_m T_0}{+\frac{\gamma_m - 1}{2} M_e^2}} \tag{13}$$

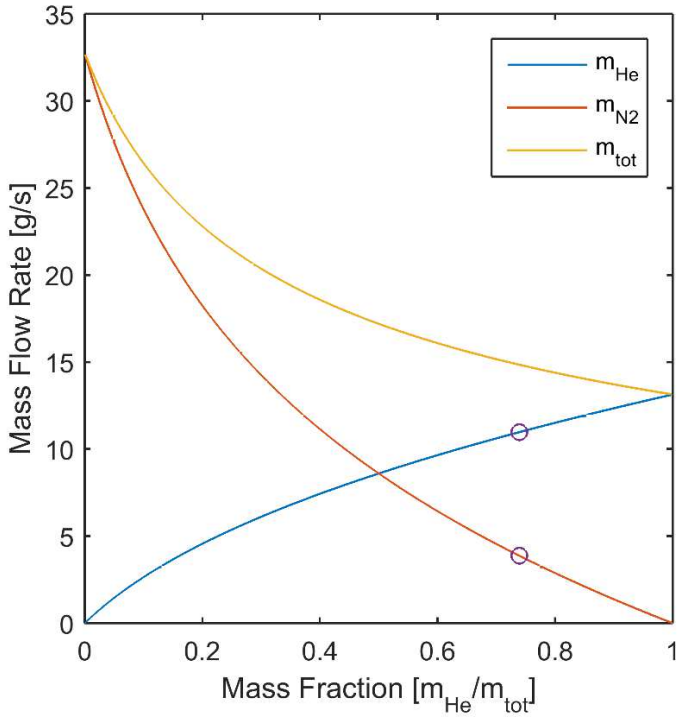

Figure 5. Modeled Helium/Nitrogen Mass Flows
(T_0=290 K, P_0=120 psia, T_{se}=290 K, P_{se}=440 psia)

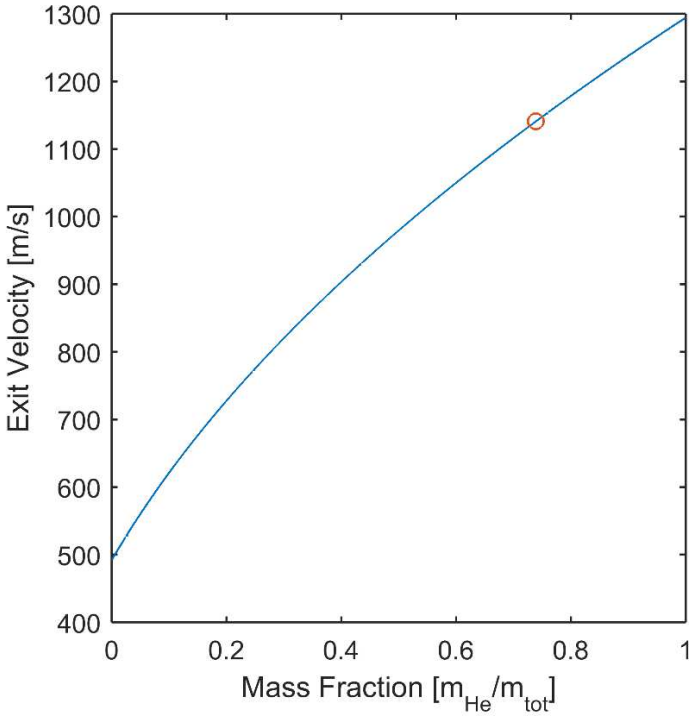

Figure 6. Modeled Helium/Nitrogen Velocity for
(T_0=290 K, P_0=120 psia, T_{se}=290 K, P_{se}=440 psia)

2.4 Collection Optics and Signal Detection

Modern streak cameras record images by directing a 1-D line of collected incident light onto a photocathode, which emits electrons. These are diverted via a ramped electric field inside the streak tube. The rate at which the field changes governs the distribution of the data along the temporal axis. A micro-channel plate (MCP) multiplies the electrons to allow detection of weaker signals. The electrons then strike a phosphor screen, which fluoresces photons at the corresponding locations. This image is captured by a charge-coupled device (CCD) with one axis indicating space and the other time. A diagram of these principles is provided in Figure 7 [27]. Because the electric field can be swept across each pixel much more quickly than a traditional high-speed shutter can cycle, extremely fine temporal resolutions can be achieved at the cost of one spatial axis.

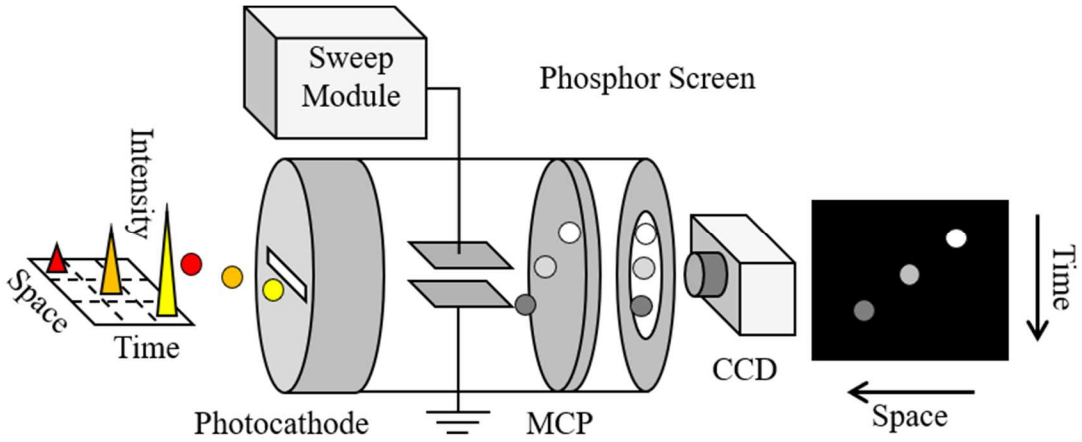

Figure 7. Streak Camera Operating Principles [27]

2.5 Particle Scatter

2.5.1 Illumination Source

The primary benefit of PSV in allowing high repetition measurements stems from the elimination of the shutter. Without the need for frame straddling as used in PIV, a long-pulse or even continuous light source is ideal as opposed to dual-head, short pulse lasers or burst mode lasers. Exposure of the particles over the entire sweep duration (in this work 50-100 μs) provides the maximum sampling rate limited only by the streak camera temporal resolution. Commercially available, high-power systems cannot provide pulses of these lengths, however, the MCP integrated into the streak camera provides a lower particle detection threshold than CCD or

complementary metal-oxide-semiconductor (CMOS) detectors alone which allows for lower power light sources to be considered.

The first system considered for this work, and which was ultimately used for the reported tests, is a laser diode. These diodes use a semiconductor as the laser gain medium which is pumped with electrical current [37]. Generally, they operate in a continuous-wave mode for which the duration is limited only by the ability to dissipate heat. The specific wavelength, which can range from violet to the infrared, is governed by the specific semiconductor material. Diodes provide power conversion efficiencies of 50% or more [37], though beam quality is generally inferior to other laser systems due to the edge-emitting design, which produces two axes diverging at very different rates, as Figure 8 shows. For this application, such a characteristic can actually be beneficial as the inherent collimated output is of an ellipse rather than a circle, which lends itself to producing the laser sheet used to illuminate the measurement region.

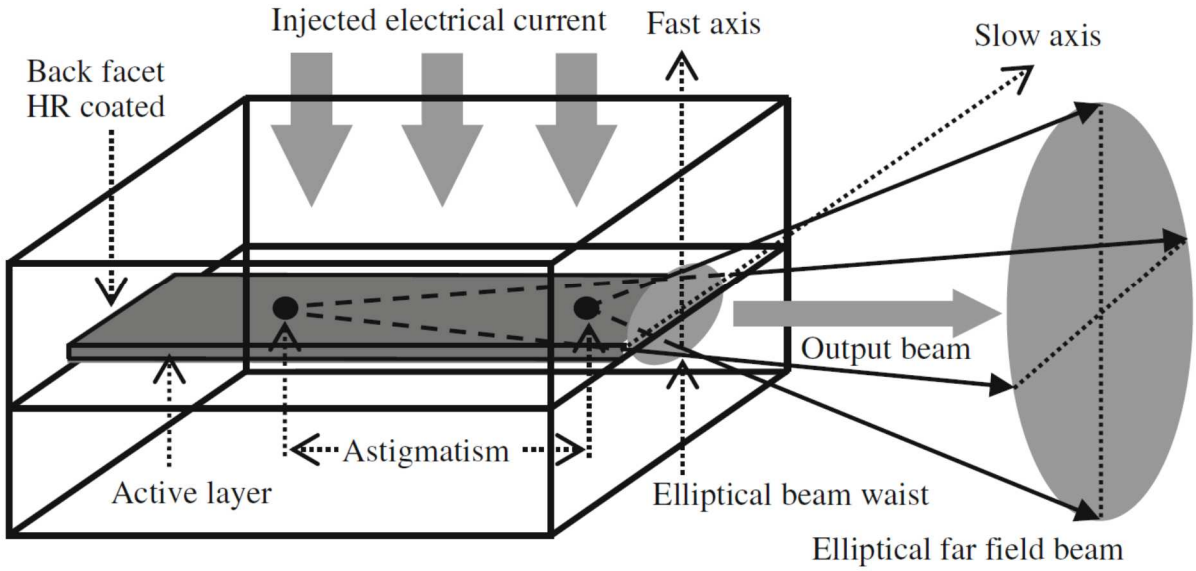

Figure 8. Edge Emitting Laser Diode [38]

The second system which was manufactured, but ultimately not needed to achieve strong scatter signal is a xenon flashlamp. These lamps are used for many high powered, pulsed light applications including as the pump system for many solid-state lasers. They operate by running a trigger of

several kilovolts across the lamp body to begin ionizing the xenon gas inside. As the xenon turns to plasma, its resistance drops dramatically, and it begins conducting an immense current from a capacitor usually charged to a few hundred volts. The electrical to optical energy conversion efficiency of the plasma is near 50% at high enough current densities [39]. The pulse duration is governed by the discharge circuit design and can be tuned from microsecond to second ranges. An RLC circuit can be designed where the lamp serves as the resistor, the capacitor provides the discharged energy, and the inductor limits the discharge rate when properly tuned to the first two components. Equation 14 defines the impedance parameter (K) for a given lamp. Equations 15 to 17 define the proportions for the initial charged capacitor voltage (V), capacitance (C), and inductance (L) for some desired total pulse energy (E) and peak duration (τ_{FL}). The peak duration represents roughly a third of the total RLC discharge duration and is used to specify the portion of the peak with a suitably small enough dynamic range for typical illumination applications. For these PSV tests, that is set at 50 µs to coincide with the streak sweep duration required for higher velocity measurements. Equation 18 gives an estimate for the lamp resistance when ionized (r_{FL}) for τ_{FL} less than 100 ms. Equations 19 and 20 provide the time dependent current (i) and electrical power (W) consumed for an underdamped RLC discharge as the damping factor (ζ) used in Equation 15 is recommended to be 0.8 to achieve a slightly broader and more even response through the peak.

$$K = 1.28\left(\frac{P_{FL}}{60000}\right)^{0.} \; l_{FL}/d_{FL} \tag{14}$$

$$= \sqrt[3]{\frac{E\zeta^4\tau_{FL}^2}{K^4}} \tag{15}$$

$$V(0) = \sqrt{\frac{E}{C}} \tag{16}$$

$$L = \frac{\tau_{FL}^2}{C} \tag{17}$$

$$r_{FL} = \frac{0.06 l_{FL}}{\pi d_{FL}^2} \quad (18)$$

$$i(t) = \frac{V_0 e^{-\frac{r_{FL} t}{2L}}}{\sqrt{r_{FL}^2 - \frac{4L}{C}}} \sinh\left(\frac{t}{L}\sqrt{r_{FL} - \frac{4L}{C}}\right) \quad (19)$$

$$W(t) = i \; r_{FL} \quad (20)$$

Xenon flashlamps produce a broadband spectrum from 200 to 1100 nm [39]. Gas fill pressure and current density affect the distribution within that range, as Figure 9 shows. Higher current densities trend towards a black body radiator at 9500°C. Though the energy is distributed across a wide range as opposed to a laser, this can in some respects be viewed as an advantage. For future application of PSV in reacting flows, a fixed wavelength laser system may avoid the background flame emissions from one propellant sample yet incur interference from another. With a broadband spectrum available, different notch filters can be deployed to utilize the system across any sample with minimal alterations. In initial tests, the spectrometer which is already attached to the streak camera could be used to evaluate the visible range emissions before performing PSV, and then the appropriate filter would be installed for the next test such that collected signal comes only from the scattered lamp light.

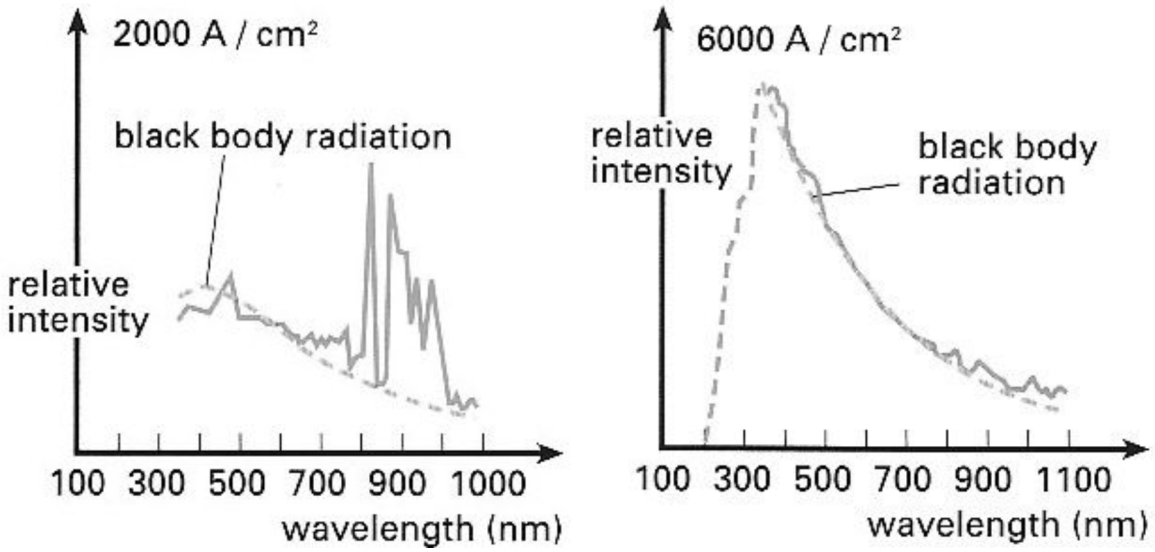

Figure 9. Xenon Flashlamp Emission Spectrum [40]

2.5.2 Mie Scattering of Spherical Particles

An observation angle of 90° relative to the incident laser sheet is typical in most PIV experiments. Depth of field and common length scales in both axes are among the reasons that this is advantageous. However, because the measurement for PSV is of a line rather than a plane, these restraints no longer apply. The collection optics can be positioned around the center axis at any angle relative to the illumination source because the length scale and image depth must only be preserved in the vertical axis. This can be advantageous in collecting maximum signal scattered from small particles. The data in Figure 10 shows that micron-scale particles in visible light fall in the Mie scattering regime. As a result, the magnitude of the scatter is a strong function of particle diameter, polarization, and observation angle.

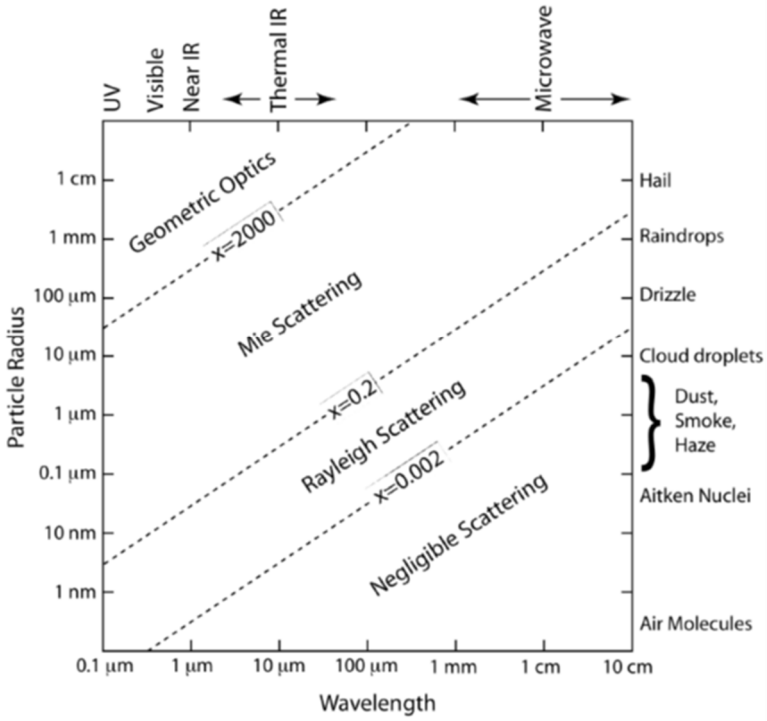

Figure 10. Light Scatter Regimes Indicating Mie Scattering at Relevant Scales [41]

Bohren and Huffman [42] provide a derivation to model the scatter from an infinite, plane wave incident on a spherical particle. The essential components are provided below. Equations 21 and 22 describe the physical system properties with ω representing the relative refractive index between the particle and fluid medium and z acting as a non-dimensional parameter relating the particle size to the wavelength of the light. Equations 23 and 24 designate scattering coefficients for the electric field. The angular dependency of the scatter is driven by π_k and τ_k in Equations 25 and 26, which form alternating, even and odd lobed polar profiles, shown in Figure 11. Finally, I denotes the scattered irradiance for light that is either perpendicular or parallel polarized to the scattering plane.

$$\omega = \frac{n_p}{n_f} \tag{21}$$

$$z = \frac{\pi d_p n_f}{\lambda} \tag{22}$$

$$p_k = \frac{\omega\psi_k(\omega z)\psi_k(z) - \psi_k(z)\psi_k(\omega z)}{\omega\psi_k(\omega z)\xi_k'(z) - \xi_k(z)\psi_k'(\omega z)} \tag{23}$$

$$q_k = \frac{\psi_k(\omega z)\psi_k'(z) - \omega\psi_k(z)\psi_k'(\omega z)}{\psi_k(\omega z)\xi_k'(z) - \omega\xi_k(z)\psi_k'(\omega z)} \tag{24}$$

$$\pi_k = \begin{cases} 0 & k \quad 0 \\ 1 & k = 1 \\ \frac{k-}{k-}\cos(\theta_S)\,\pi_{k-} \quad -\frac{k}{k-}\pi_{k-} & k > 1 \end{cases} \tag{25}$$

$$\tau_k = k\cos(\theta_S)\pi_k - (k+1)\pi_{k-} \tag{26}$$

$$I_\perp = \left|\sum_k \frac{k+}{k(k+\ )}(p_k\pi_k + q_k\tau_k)\right| \tag{27}$$

$$I_\parallel = \left|\sum_k \frac{k+}{k(k+\ )}(p_k\tau_k + q_k\pi_k)\right| \tag{28}$$

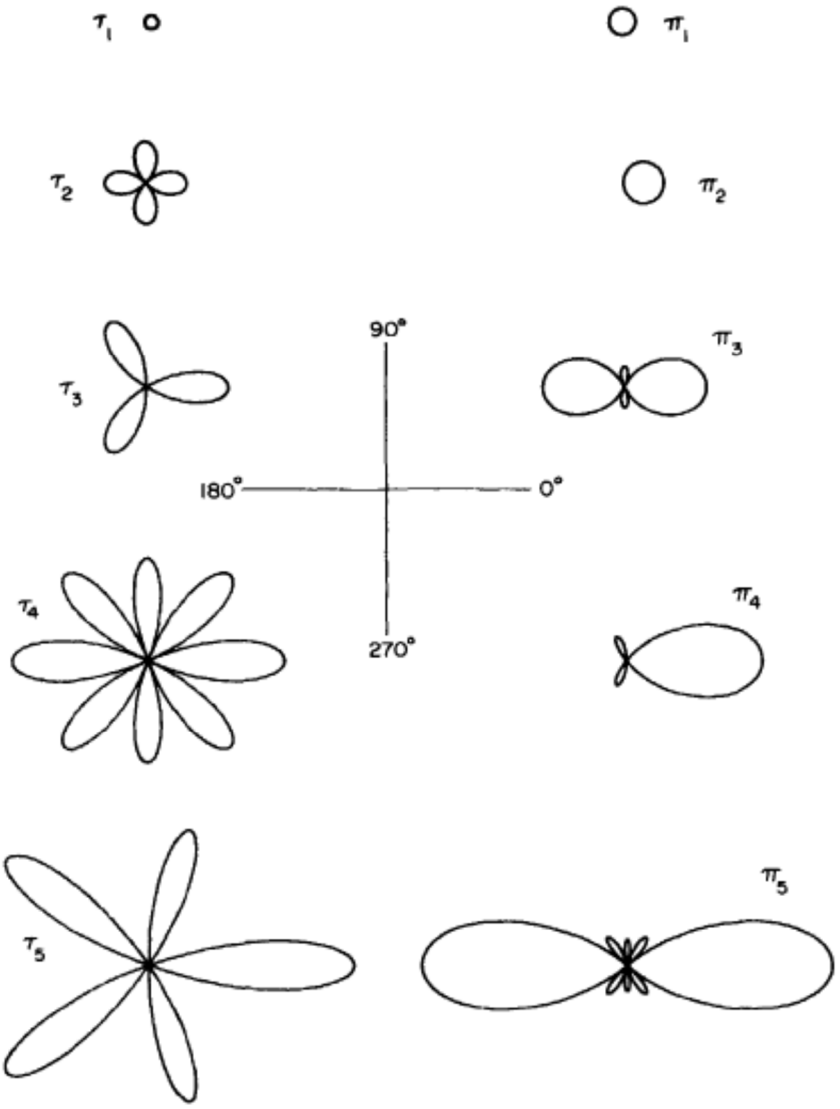

Figure 11. Polar Plots of the First Five Angle-Dependent Functions, τ_k and π_k [42]

This model can be run for all seed materials and powder sizes to visualize how differently each may produce scatter and how viewing angle between the incident light and the collection optics can be exploited to improve signal. Figure 12 shows the log-scale, normalized results for a SiO_2 particle in nitrogen with the incident laser light coming from the left of the diagram and the majority of scattering occurring directly downstream. In contrast, ideally polarized light viewed at 90° produces ~1% of the maximum available intensity. If the viewing angle can be shifted towards 0° while avoiding the directly incident, non-scattered light on the collection optics, the captured particle scatter signal can be increased over tenfold. Furthermore, the high degree to which laser

diodes are polarized may be negated, as the forward scattering node is equal for both parallel and perpendicularly polarized incident light.

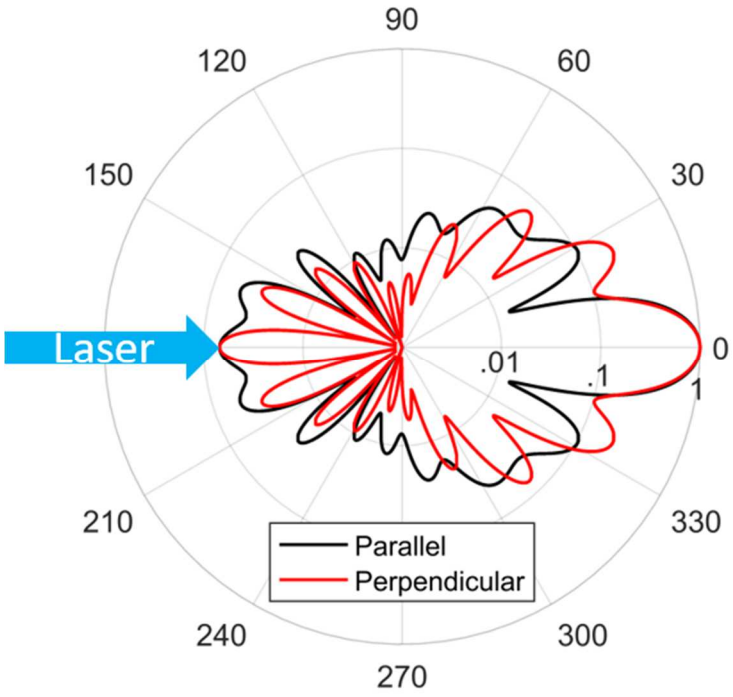

Figure 12. Polarized Mie Scatter of SiO_2 Particle
(d_p = 1.0 μm, n_f = 1.0, n_p = 1.47 [43], λ = 450 nm)

2.6 Streak Data Analysis

In order to extract the particle velocity data, the raw streak images undergo a filtering and peak detection process. The first step, performed in the frequency domain, serves to emphasize the angular orientation of the streak signals present in the image. A two-dimensional continuous space Fourier transform (CSFT) is performed on the region of interest (ROI). As the flow analyzed in this work is steady in time and relatively uniform along the spatial axis (given the short measurement region), the image is cropped to a single, horizontal band and filtered once. However, for flows that are time varying or non-uniform in space, this process can be broken down to smaller windows to better enhance individual velocity components amongst the field.

A one-dimensional Fourier transform breaks a signal down into a series of sinusoidal waves with varying frequencies, phases, and magnitudes. Similarly, in two-dimensions, the CSFT

deconstructs an image into a combination of planar sinusoidal waves of varying frequencies, phases, magnitudes, and angular orientations [44] [45] [46] [47] [48] [49]. Figure 13 depicts the corresponding spatial and frequency domain representations of a single constituent wave. The angle of the two white dots in the frequency spectrum is perpendicular to the peaks of the waveform, and the dots are spaced from the center proportionally to the frequency of the waveform.

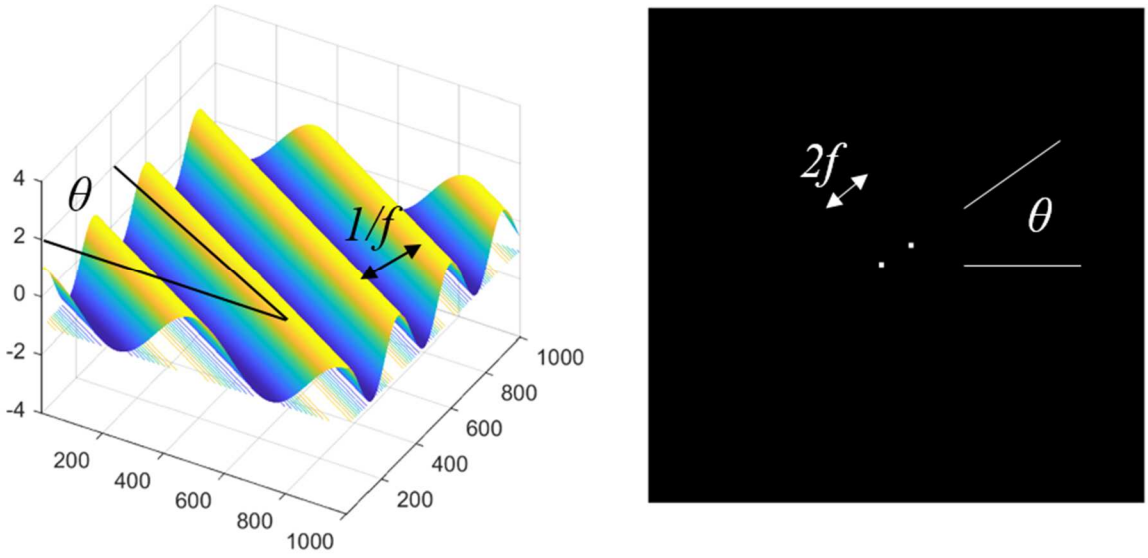

Figure 13. Two-Dimensional Fourier Transform Principle Components

As described Section 2.2, the primary goal in processing of the streak images is to detect the slope of each streak sample, which can then be scaled to represent the instantaneous particle velocity. With the above principles in mind, the ideal filter enhances the image features corresponding to these angles and remove the noise added in other directions. A hyperbolic profile overlain on the obtained frequency spectrum allows limits to be set on a range of preserved angles, shown in Figure 14, while still passing the low frequency components in all direction which form the base of the image. The orientation of the major axis of the hyperbola is set by applying a linear fit to a group of peaks in the initial CSFT. This represents a first approximation of the mean orientation of all components in the image. The asymptotes of the hyperbola define the pass band of angles such that variations from streak to streak are still preserved and a more exact measurement of slope can be detected at each location in the spatial domain later. The hyperbolic filter also maintains a

set separation between vertices at the center to preserve low-frequency components of all orientations.

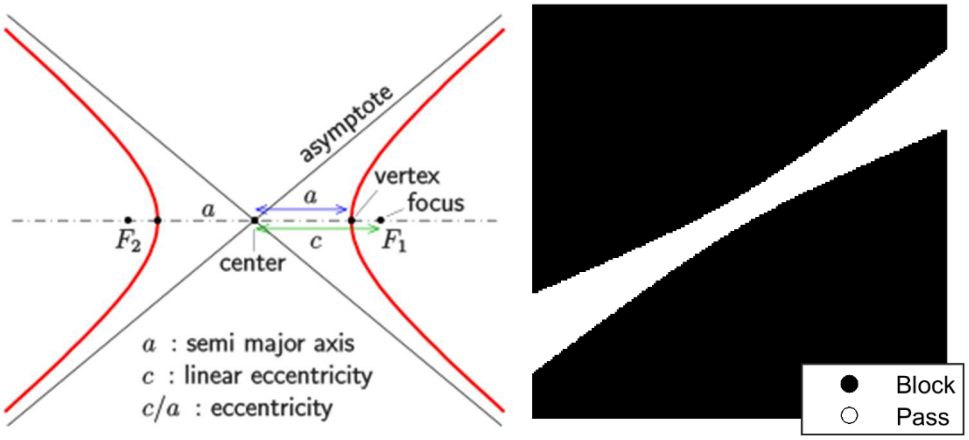

Figure 14. Hyperbola Parameters [50] and Pass Filter Image

Applying the inverse CSFT to the filtered frequency data resumes processing in the spatial domain. The MathWorks Bioinformatics Toolbox is used to further enhance the image and detect peaks from the streak signals [51]. Background adjustment at each time step (pixel column) produces consistent peak intensity across the image using a stepping, windowed procedure with spline approximation of the baseline. Resampling of the image at ten times the frequency then allows interpolation of peak locations between pixels. Local peaks in each row or column are detected using a wavelet decomposition method. The direction of the peak identification step is chosen to be more orthogonal to the streak samples for the given test (i.e. for tests where the slope is greater than one, each row is sampled, and for tests where the slope is less than one, each column is sampled).

After identifying local peaks across the entire domain, the relative shift is analyzed by comparing each peak in a given row to all those in the successive row. To eliminate spurious shift measurements at the end of a given streak, a connectivity threshold is defined between neighboring points in the two rows being compared. If the minimum shift distance falls within this range, the program records the slope at that location as the distance between the rows being compared divided by the detected shift of the given peak between those rows.

3. EXPERIMENTAL SYSTEMS

The following chapter details the hardware used for the experiment and measurement. A cold gas nozzle and particle seeder create the flow system. The illumination source, collection optics, and camera are profiled, and the positioning and calibration of each with respect to the measurement volume is described.

3.1 Test Article

A cold-flow supersonic nozzle test bed has been developed to demonstrate and refine PSV. This allows iterative validation against predictions and existing velocimetry techniques to be discussed in the subsequent sections. The system runs on high-purity, compressed gas from the facility bulk nitrogen supply or portable cylinders of alternative gases. Development testing can be performed rapidly and indefinitely. Cold gases provide the ability to increment the velocity in a predictable manner via selection of inert gases of different molecular weights such as argon, nitrogen, and helium. By using single composition gases, the expected velocities can be determined from fundamental principles.

3.1.1 Nozzle

The nozzle, shown in Figure 15, is machined from stainless steel 304 with a 4.65 mm throat and an expansion ratio of 1.5. It interfaces with a combustion chamber used for prior hypergol characterization research [52], which will be the measurement destination once this concept has been developed. For cold gas testing, a small flow rate of nitrogen is fed through the seeder and is combined with the remaining flow required to choke the nozzle and reach the desired stagnation pressure. An aluminum holder was machined with a 60 mm long by 19 mm diameter settling region to measure stagnation temperature and pressure and allows the flow to straighten before reaching the nozzle.

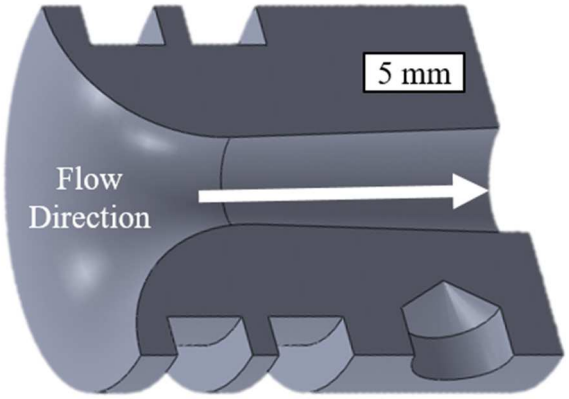

Figure 15. Converging-Diverging Conical Nozzle (Flow direction is from top to bottom) (d_t = 4.65 mm, A_e/A_t = 1.5)

3.1.2 Plumbing and Instrumentation

The P&ID describing the system setup between the facility nitrogen system, the two-stage seeder, and the nozzle test article for nitrogen streak tests is shown in Figure 16. The 6000 psi supply pressure allows MR-N2-03 to provide ample flow to choke the nozzle at the desired stagnation conditions. For helium streak tests, a portable cylinder of ultra-high purity helium is connected to a high-flow 1.0 C_v regulator and 1/2" pneumatic ball valve in lieu of MR-N2-03 and PV-N2-03. The primary instrumentation required for data analysis are TC-MAIN, PT-MAIN, and PT-SEED. For the near-ambient, inert flow, an exposed junction thermocouple can be used to optimize response time. Each transducer provides ±0.25% FSO accuracy, which corresponds to 0.75 psi and 1.25 psi for PT-MAIN and PT-SEED, respectively. Data is recorded at 1000 Hz using an NI SCXI-1001 chassis. While a single cycle is slower than the entire streak camera exposure (100 or 50 μs), the flow is relatively steady by the time the streak measurement is acquired. A Stanford Research Systems DG645 is used to sync the streak camera trigger to the v1212 video and NI DAQ.

Table 2. Fluid System Instrumentation Specifications

Instrument	Manufacturer	Model	Range	Uncertainty
TC-MAIN	Omega	KGSS-18E-6	73-1523 K	2.2 K
PT-MAIN	Druck	PMP-1260	0-300 psi	0.75 psi
PT-SEED	Stellar	GT1800-500G-350	0-500 psi	1.25 psi

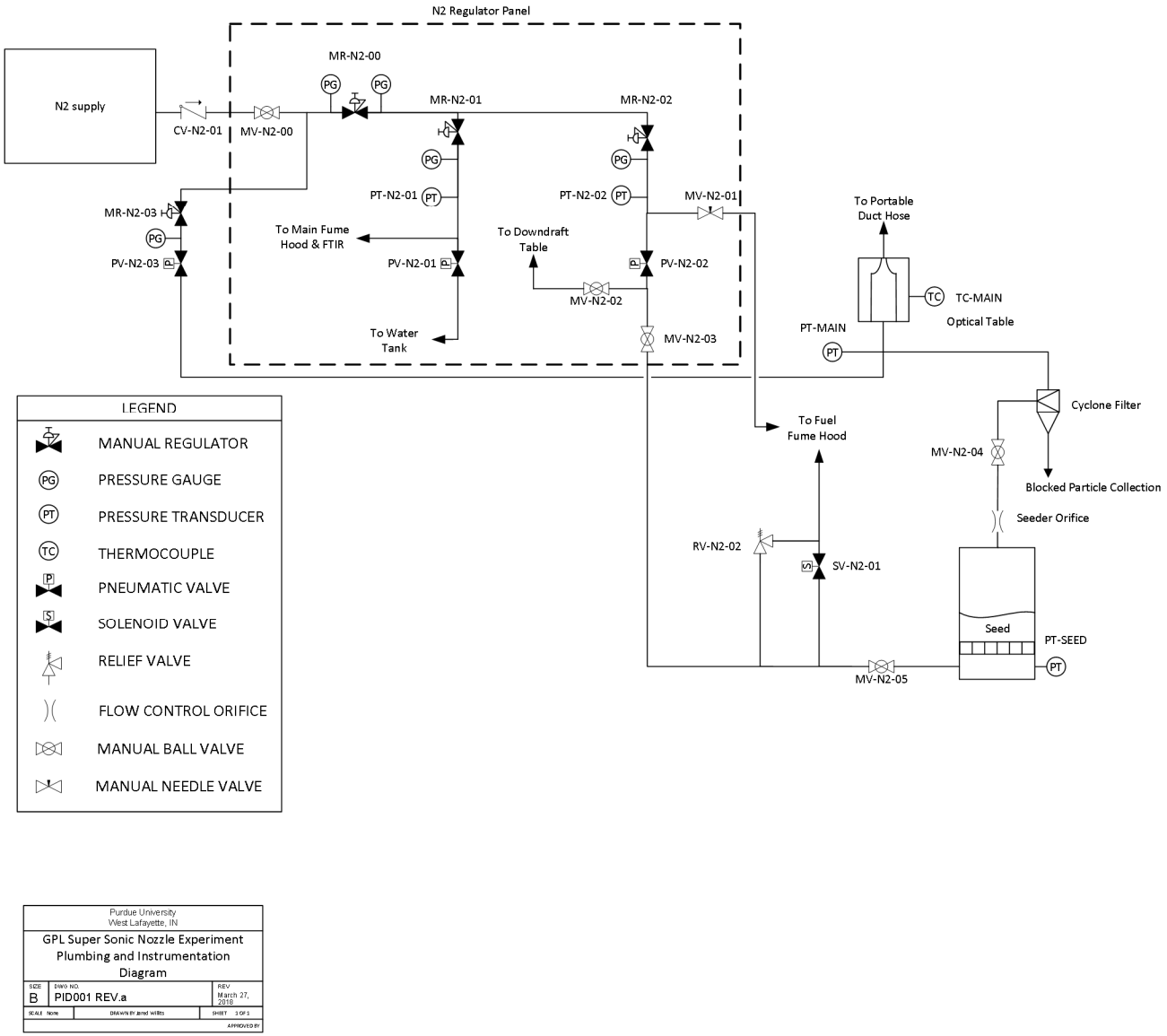

Figure 16. Supersonic Nozzle Experiment Plumbing and Instrumentation Diagram

3.2 Two-Stage Particle Seeder

The seeder, shown in Figure 17, uses two stages in series to filter the particles through elutriation. The first stage is a vertical elutriator where sedimentation of larger particles is caused by gravity acting counter to the lifting flow. The design is adapted from a similar device used by DLR [53] [54]. A sintered disk at the bottom of a 3 inch diameter pipe produces a fluidized bed of seed. At the exit of the first stage, a sonic orifice is used to limit the flow rate such that the gas velocity in the pipe is higher than the terminal velocity for particles of the desired seed size. Any larger particles for which the terminal velocity is greater than the flow velocity remain settled on the bottom of the system. The orifice also serves as a high shear region to break up particle agglomerates.

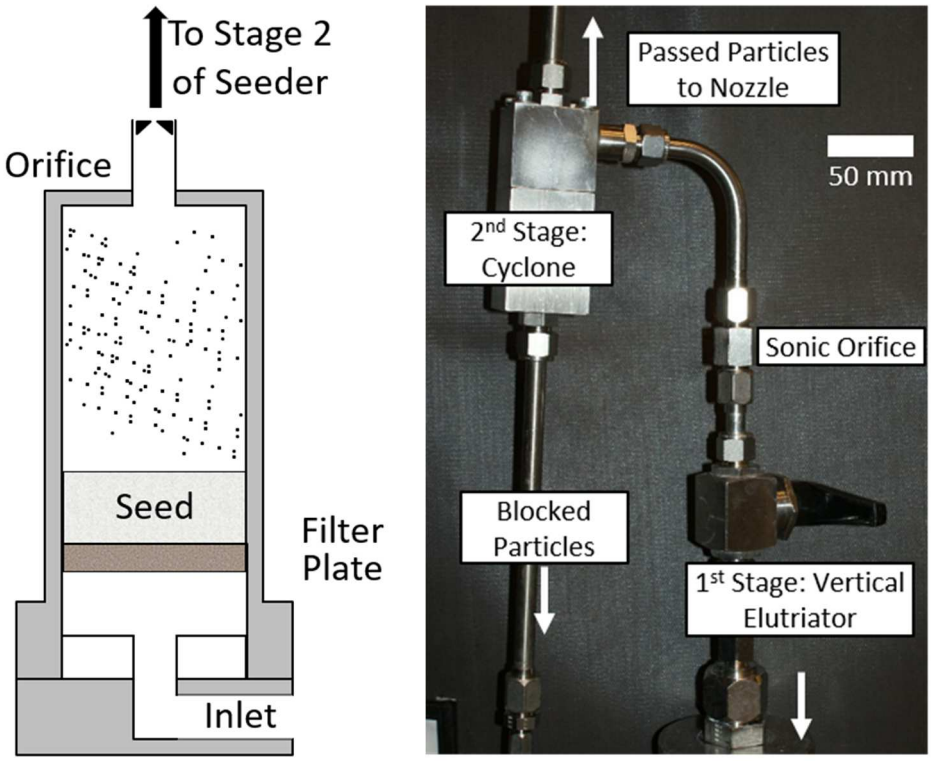

Figure 17. First and Second Stage Seeder Layout

The second stage is a cyclone filter, also shown in Figure 18, which takes flow from the first stage and further separates the particles using centrifugal elutriation [55]. The figure shows a welded tube connection, but within the cyclone, a rectangular inlet is machined to direct the flow along

the circumference of a cylinder. As the flow angularly accelerates along a conical contraction, the momentum of larger particles forces them outward towards the wall until they fall to the collection tube below. Particles of smaller diameter remain entrained in the flow along the entire pat. Because the outlet tube at the bottom of the contraction where large particles collect is closed at the other end, eventually, the flow turns and exits the top of the device carrying only the smallest diameter particles to be combined with the bulk nozzle flow.

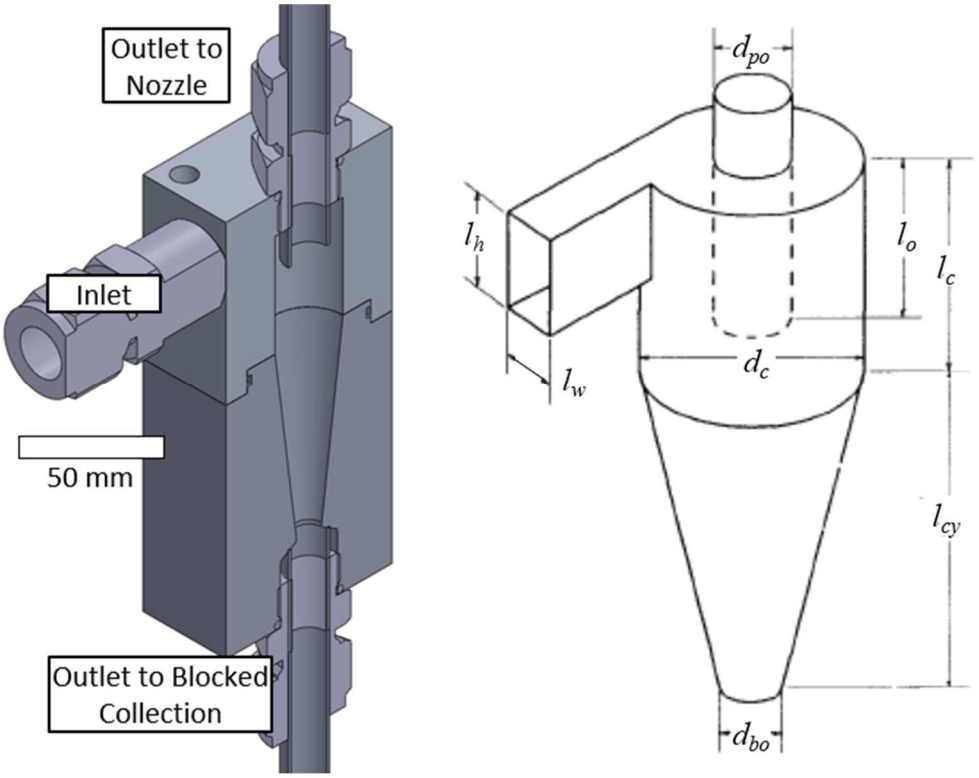

Figure 18. Cyclone Cross Section and Non-dimensional Parameters [55]

The dimensions of the device, shown in Table 3, are approximately scaled from the non-dimensional design proportions for a Stairmand high efficiency cyclone [56]. A nominal cylinder diameter (d_c) of 20.8 mm provided an ideal cutline for the initial flow rates and particle sizes investigated and closely corresponds to system inlet and outlets matching a ½-inch tube inner diameter.

Table 3. Stairmand Cyclone Filter Dimensions

Parameter	Non-dimensional Size [Parameter/d_c]	Length [mm]
Cylinder Diameter, d_c	1	20.8
Pass Outlet Diameter, d_{po}	1/2	10.2
Inlet Height, l_h	1/2	10.4
Inlet Width, l_w	1/5	4.2
Outlet Length, l_{po}	1/2	10.4
Contraction Height, l_{cy}	5/2	52.1
Cylinder Height, l_c	3/2	31.2
Block Outlet Diameter, d_{bo}	3/8	7.9

The second stage filtering performance uses an approximation of Barth's efficiency model for a Stairmand cyclone, shown in Equation 29 [55] [57]. Figure 19 shows one example of the calculated velocity ratios in stage 1 and filtering efficiency in stage 2 for SiO_2 particles with nominal diameter of 1 μm. For this 0.53 mm sonic orifice, the first stage filters all particles and agglomerates larger than 10 μm and provides a velocity ratio of the flow to the particle terminal velocity greater than 100 for particles at or below the nominal diameter to produce sufficient seeding density [58]. The second stage then provides a cutoff line between 1 μm and 4 μm for any agglomerates that pass through the sonic orifice. Exact tuning of these parameters for the reported test conditions is discussed in Chapter 4.

$$\eta = \frac{}{1+\left(\frac{117\rho_p d_p^2 Q}{\mu d_c^3}\right)^{-3.2}} \tag{29}$$

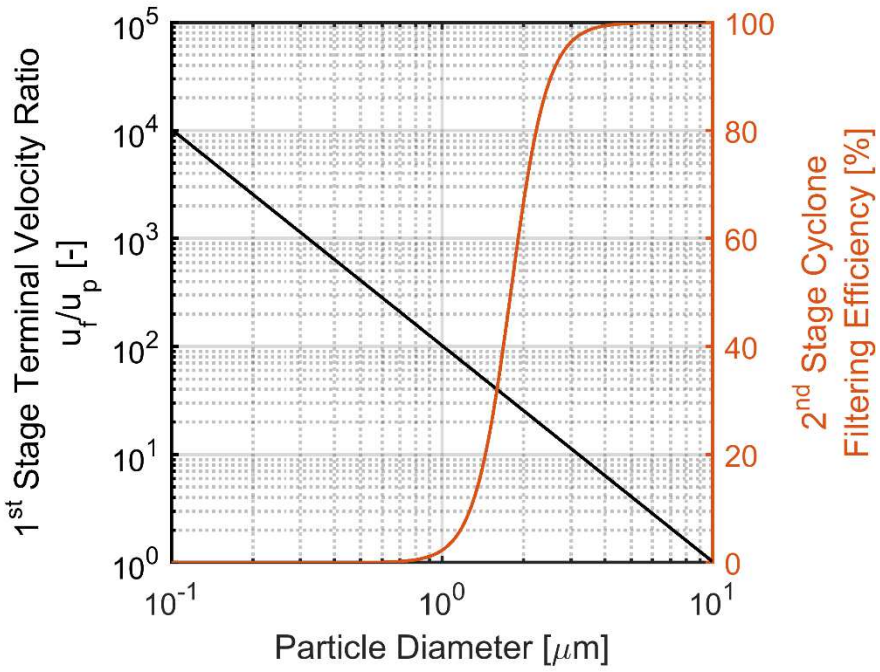

Figure 19. Predicted SiO_2 Seeder Filtering Results
(P_{se} = 300 psia, d_t = 0.53 mm)

3.3 Seed Characterization

A Phenom ProX desktop SEM is used to characterize seed particle size [59]. The system provides up to 100,000x electron optical magnification and 12x digital zoom at resolution down to 17 nm. Powders can be examined when initially received, after treatments such as baking, vacuuming, or ball milling, and upon collection from the seeder or from measurement volume flows. This allows continuous assessment to improve the seed powder handling, loading procedures, and system operation to ensure the ideal particle size is consistently met.

3.4 Illumination

3.4.1 Laser Diode

The illumination source used for this experiment is a Nichia NUBM44 laser diode. The nominal wavelength of the emission is 450 nm. Most tests were performed at a set current of 3 A corresponding to a rated power output of 4.5 W. The diode is mounted in a brass heat sink, and a small fan is used for forced convective cooling to permit intermittent operation for the durations

necessary to prepare and run each test. A collimating lens mounted onto the diode housing provides initial focus of the beam to 4 mm x 1mm, and an additional 150 mm focal length cylindrical lens further focuses the sheet to a width of approximately 200 μm at the sample location. Figure 20 shows samples using thermal sensitive alignment paper to profile the beam at the measurement location. A protected silver, plane mirror in a 2-axis kinematic mount allows steering of the beam to the measurement region.

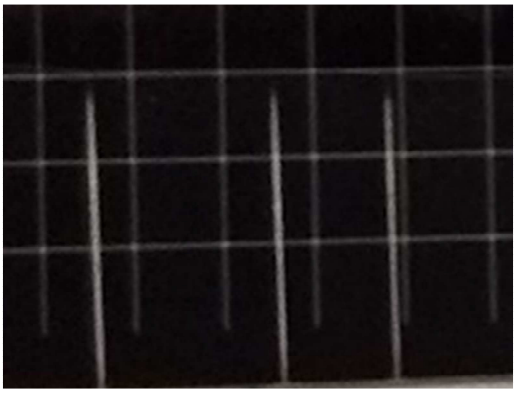

Figure 20. Diode Profiling Samples at Beam Waist

3.4.2 Xenon Flashlamp

The discharge circuit for the flashlamp uses an EG&G-350 flashlamp supply capable of converting 24 VDC up to 1000 VDC. This is used to charge the 66 μF capacitor to 400 V, and it also provides a TTL trigger input which produces a 200 V output to the high-voltage transformer initializing the lamp ionization. The lamp used is a model L4040Q linear quartz lamp with inner bore diameter of 2 mm arc length between anode and cathode of 27 mm. A polypropylene film capacitor is used to minimize series resistance. Ferrite and powder core inductors saturate near or below the current load needed for this application, as Figure 21 displays. An air gap core was instead made from a 3-D printed plastic base and hand-wound 10 AWG enamel cladded wire to the 39 μH specification needed. A safe discharge circuit was also designed to slowly dissipate the capacitors when testing was completed using two MOSFET switches to open the connection to the DC supply and close a connection from the capacitor to a 25 kΩ, 50 W resistor. Figure 22 shows the completed power supply. The modeled and scoped response for the lamp discharge is shown in Figure 23. The peak duration of 50 μs is shaded in blue to designate the bounds of the exposure that would be used for a PSV measurement. The model shows very good agreement despite neglecting any variation in

lamp resistance at different current densities through the discharge start-up and other inefficiencies present in each component. The peak electrical output power is 43 kW.

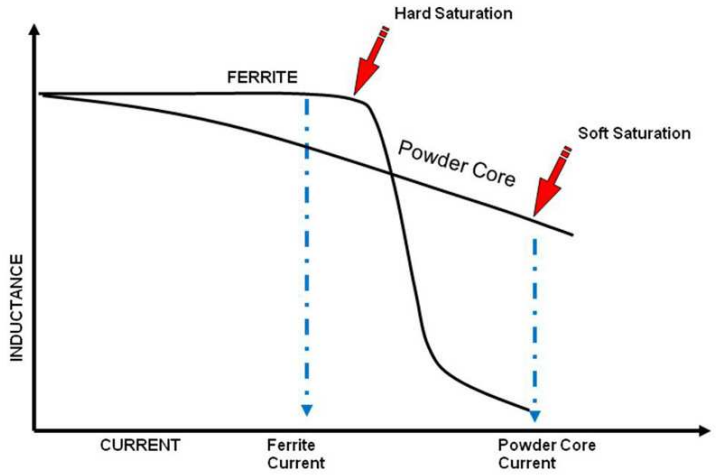

Figure 21. Solid Core Inductor Saturation Profiles [60]

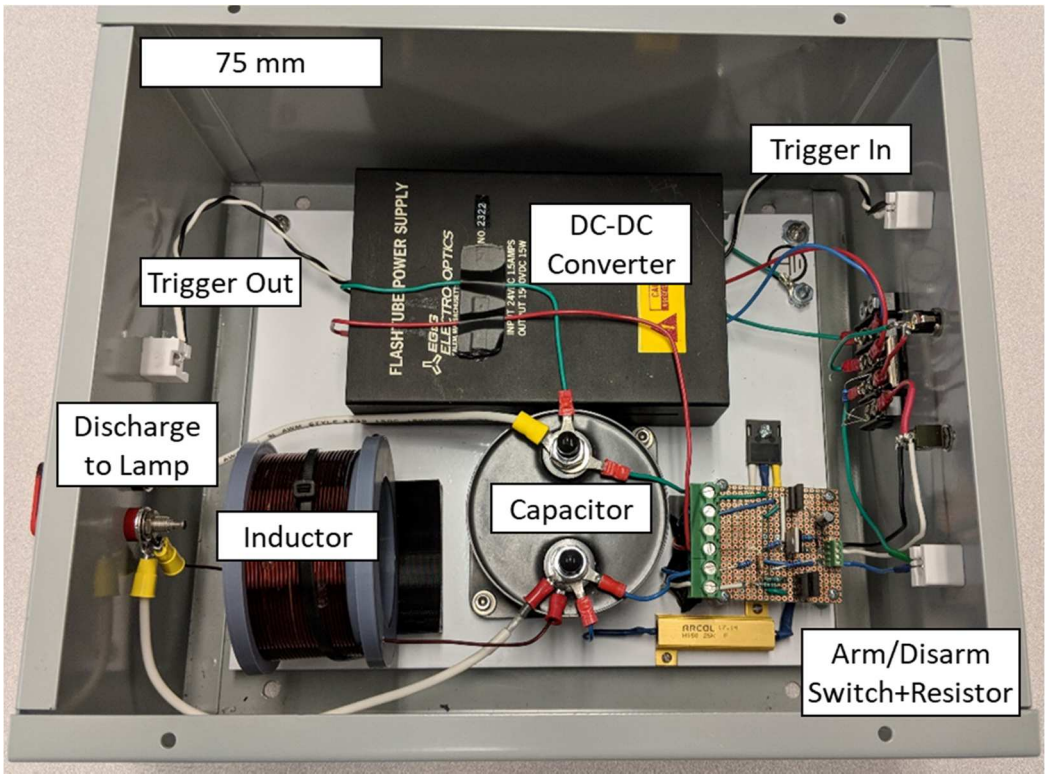

Figure 22. Flashlamp RLC Power Supply Circuit

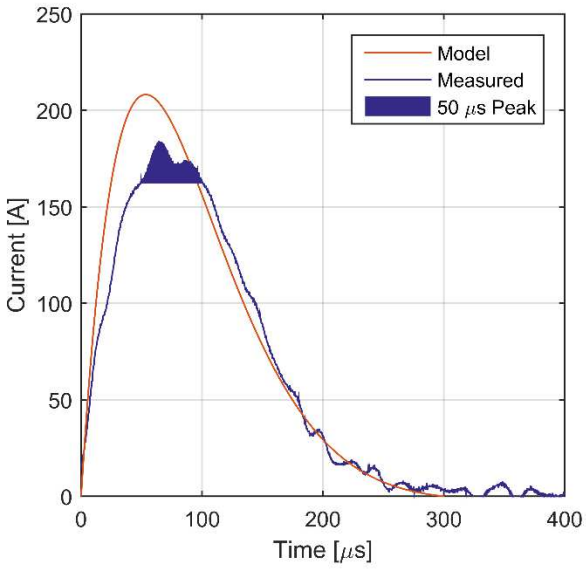

Figure 23. Modeled and Scoped Discharge Current of the Flashlamp
($V(0)$ = 400 V, C = 66μF, L = 39 μH)

To harness that power once it's converted to optical radiance, a rear reflector was designed to envelope the lamp. Because the desired measurement volume is a 1-D line and the lamp is linear, a cylindrical, elliptical reflector was chosen to provide maximum solid angle capture. The elliptical profile removes spherical aberrations allowing a much more concave shape than would otherwise be possible with a circular profile [61] [62]. The final design is shown in Figure 24. The lamp encloses 240° of the lamp and focuses it towards the downstream optics. This allows a field stop to be placed at the projected lamp image location to form a narrower illumination source. Although this will discard light, it will produce a sharper measurement region. This image can then be directed to the nozzle plume via a relay lens.

A rough, CNC-ground blank of the elliptical reflector was hand polished before receiving a silver mirror coating via plasma vapor deposition. The polishing process involves machining an aluminum lap shaped to the negative of the mirror contour, coating the lap with pitch, spreading silicon carbide onto the pitch, and grinding the mirror blank along the lap. The abrasives stepped from 120 grit to 800 grit in six increments until a final polish was performed with 10 μm cerium oxide powder. The final mirror and lamp assembly is shown in Figure 25 mounted on a two-axis stage to allow aiming of the outputted beam.

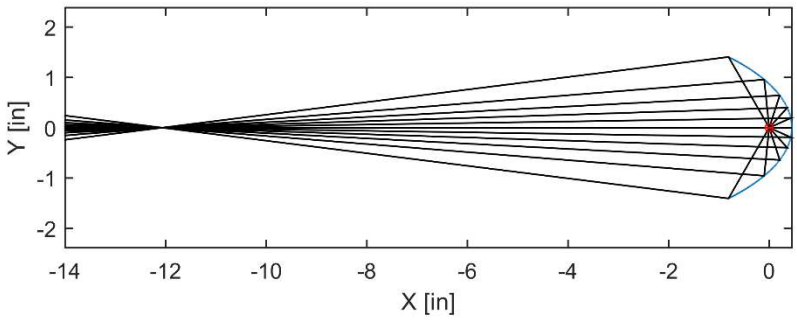

Figure 24. f/4 Elliptical Rear Reflector Ray Diagram

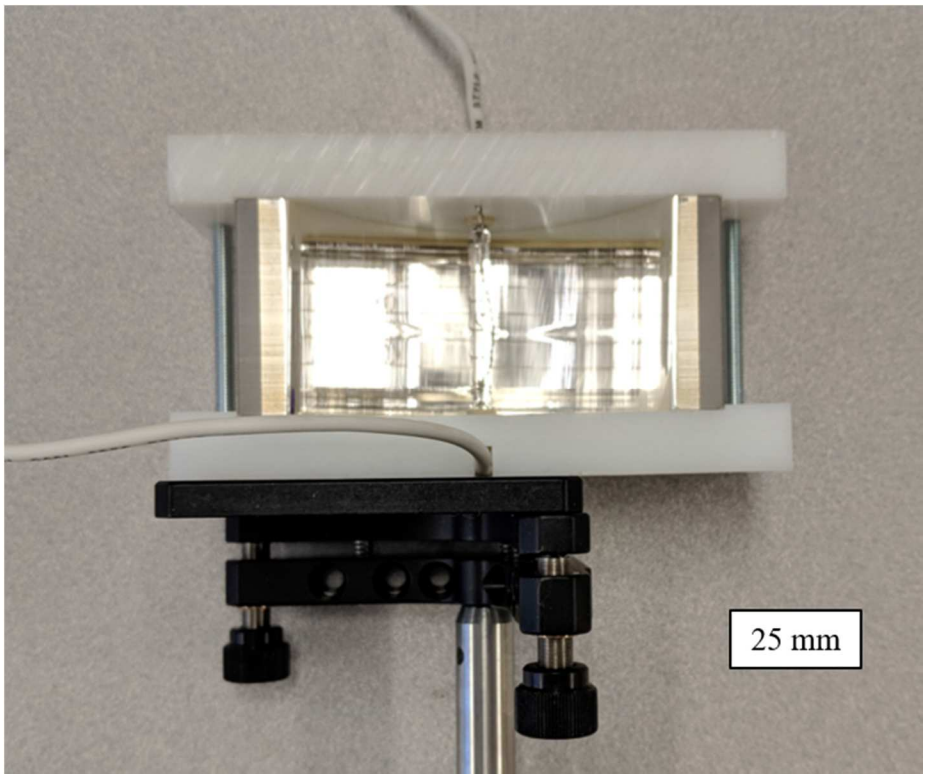

Figure 25. Flashlamp and Rear Reflector Assembly

3.5 Digital Streak Camera

A Sydor Instruments Ross 2000 streak camera is used to record the particle motion through the illuminating laser sheet [63]. It is comprised of a Photek STX streak tube, a Photek MCP125 intensifier, and a Prosilica GC-1380 CCD. The maximum spectral sensitivity of the streak tube and MCP coincide with the laser diode wavelength of 450 nm, as Figure 26 and Figure 27 show.

The CCD output is 12-bit resolution and provides 1360 pixels in the time domain and 1024 pixels in the spatial domain. The twelve available sweep speeds, listed in Table 4, are calibrated across the central 90% of the time axis, and only a portion of about 200 pixels in the spatial domain were used for this experiment given the height of the laser sheet. The quoted spatial resolution of the streak camera system is 10 lp/mm at 20 to 40% contrast depending on the region of the sensor, and the system magnification is 0.376x

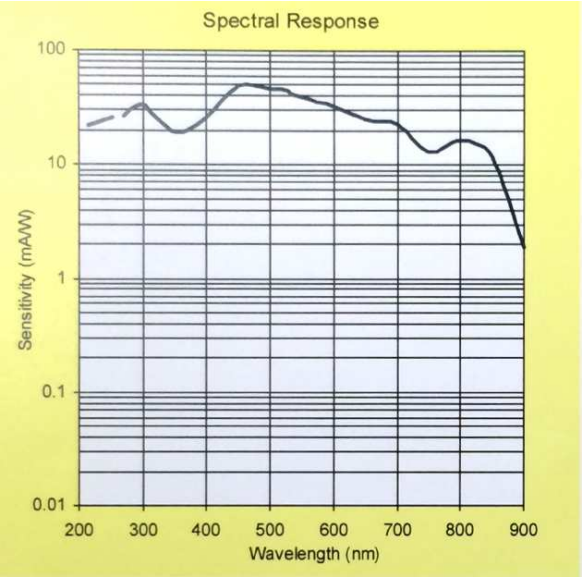

Sensitivity:	234 µA/lm	
	mA/W	%QE
214nm	22.02	12.76
254nm	25.77	12.58
270nm	26.52	12.18
280nm	30.55	13.53
290nm	32.48	13.89
300nm	33.05	13.66
350nm	19.49	6.90
400nm	25.57	7.93
450nm	48.92	13.48
500nm	46.40	11.51
532nm	41.53	9.68
550nm	38.82	8.75
650nm	25.28	4.82
750nm	12.99	2.15
800nm	16.45	2.55
850nm	11.97	1.75
900nm	1.90	0.26

Figure 26. Ross 2000 Streak Tube Spectral Response [64]

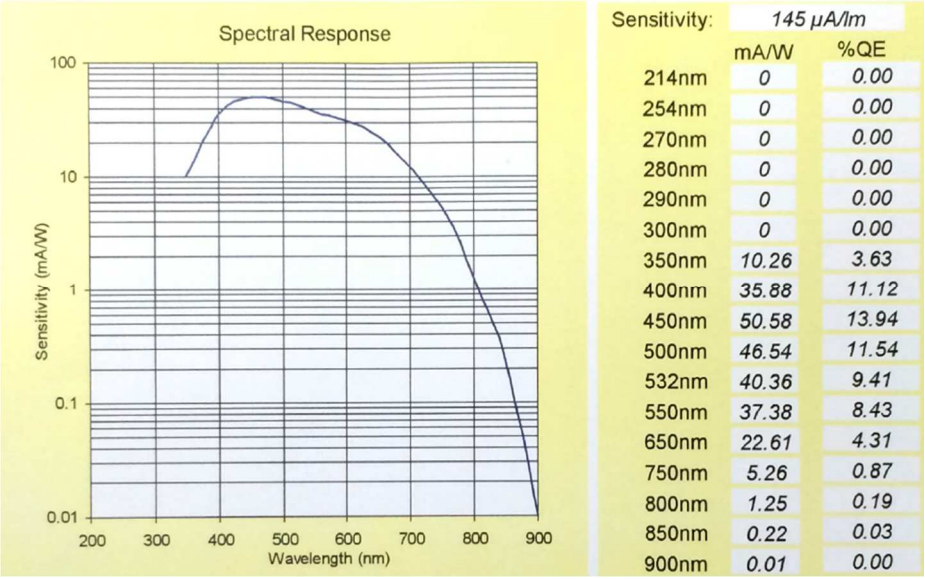

Figure 27. Ross 2000 MCP Spectral Response [64]

Table 4. Streak Camera Available Sweep Speeds and Resolution [65]

Sweep Duration	Average Pixel Dwell Time	Pixel Dwell Time Uncertainty
31.03 ms	24.90 µs	1.43 µs
21.08 ms	16.97 µs	0.48 µs
10.88 ms	8.76 µs	0.19 µs
5.51 ms	4.43 µs	0.18 µs
1.06 ms	852.6 ns	62.4 ns
519.87 µs	418.6 ns	23.7 ns
99.39 µs	80.0 ns	5.77 ns
49.17 µs	39.6 ns	2.5 ns
9.89 µs	7.97 ns	0.44 ns
4.98 µs	4.01 ns	0.23 ns
1.02 µs	814 ps	49 ps
294 ns	240 ps	10 ps

It is worth noting that, as delivered, the streak camera is mechanically coupled to an Acton 2356 UV-Vis spectrometer as the system's original purpose was to track transient combustion reactions. Rather than removing the spectrometer during testing, the highest efficiency grating is set to a

zero-order reflection, and the collected signal is passed through the device on to the streak camera at a 1:1 magnification. The net impact is that the 1200 g/mm, 300 nm blaze grating used only passes some fraction of the available light. This issue could be rectified in the future by adding an additional grating turret to the system with a plane mirror to maximize efficiency. In order to input the image to the spectrometer, the entrance slit and fiber coupling stage are removed, and an f-mount lens adapter is installed to complete the collection optics described in Section 3.6.

3.6 Streak Collection Optics

Figure 28 shows a diagram of the measurement setup. The diode is oriented with the long axis vertical, and its collimated output is focused into a thin sheet by a 150 mm focal length cylindrical lens. The beam waist is located to the nozzle center line by a plane silver steering mirror. A 50 mm diameter, 150 mm focal length doublet relay lens collects the scattered seed signal and projects at roughly 1:1. A translating stage attached to this lens allows fine focus adjustment after the primary lens discussed below has been set. A translating stage on the diode steering mirror allows the laser sheet to be projected just past the edge of this lens, while also crossing the nozzle centerline. A periscope formed from two 25 mm silver mirrors serves three purposes: to rotate the image 90°, translate the image down to match the height of the streak camera, and to steer the image into the camera. Because the streak camera cannot easily be repositioned, two-axis fine rotation control on the lower mirror provides small adjustments to ensure the signal is projected directly into the lens. A micrometer slit is placed at the relay lens image plane to serve as a field stop. Projected back towards the nozzle, this slit limits the field of view with respect to the nozzle radius. Whatever horizontal field is passed through the system is integrated into a single line, so this is necessary to avoid imaging particles near the nozzle perimeter. During testing, the slit was set to widths between 0.5 and 1 mm to provide sufficient seeding density within a given streak exposure. A Nikon 200mm f/4 ED-IF AF Micro-NIKKOR lens is used as the primary lens and is focused near 1:1 onto the relay lens image plane at the micrometer slit. The lens is mounted to the spectrometer, which passes the signal through to the streak camera.

1) 450 nm Laser Diode
2) Ø25 mm x 150 mm f.l. Cylindrical Lens
3) Ø25 mm Silver Mirror
4) Seeded Nozzle Exit
5) Ø50 mm x 150 mm f.l. Doublet Relay Lens
6) Ø25 mm Silver Mirror Periscope
7) Micrometer Slit
8) 200 mm f.l. Nikon Lens
9) Spectrometer
10) Streak Camera

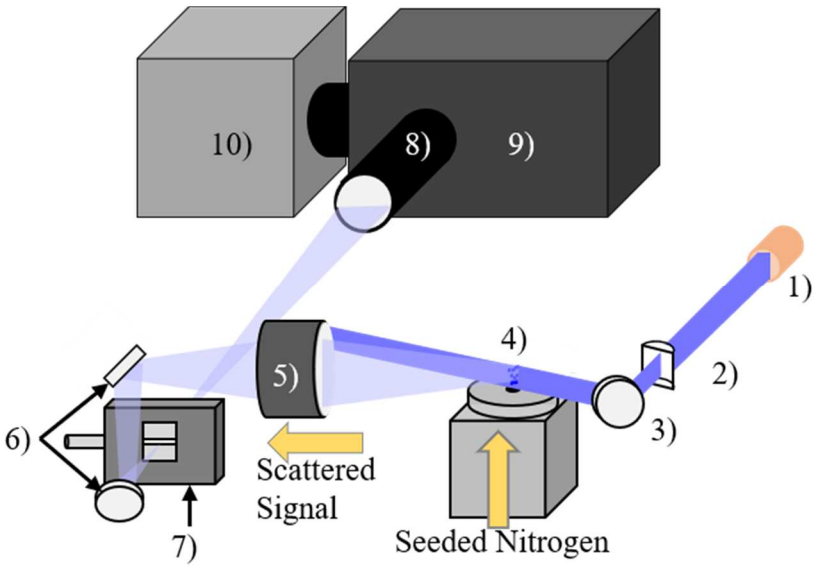

Figure 28. Particle Streak Velocimetry Collection Optics Layout

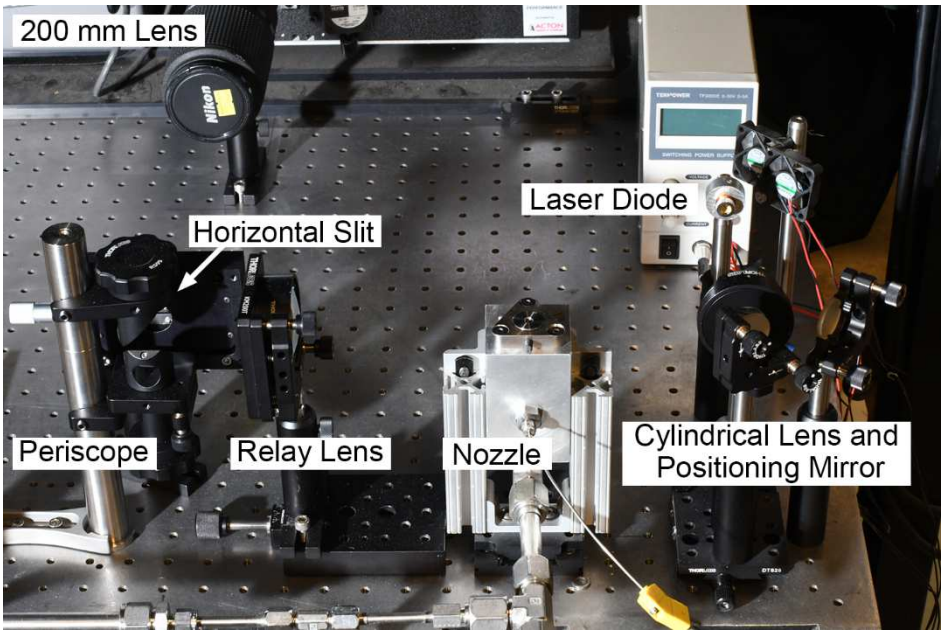

Figure 29. Streak Camera Collection Optics Setup Photo

The streak camera is aligned to a 0.6 mm diameter pin that can be mounted in the nozzle, shown in Figure 30. In addition to the steering knobs mentioned on the periscope, the nozzle is mounted to a linear translation stage. A low-powered, red diode is aimed onto the alignment pin to provide

a reference point of the measurement region. First the signal is maximized down the optical axis using the periscope and located vertically near the center of the CCD. Then, the nozzle is moved laterally until that signal is maximized on the streak camera output. The micrometer slit and nozzle are then adjusted iteratively until the relay perfectly focuses the image onto the slit allowing maximum signal detection of the target beam with only a slit opening of ~100 μm. Once the slit, nozzle, and CCD are sufficiently centered, the slit can be opened to the necessary field of view, and the primary laser diode can be aimed towards the relay lens edge and translated to intersect the nozzle alignment pin.

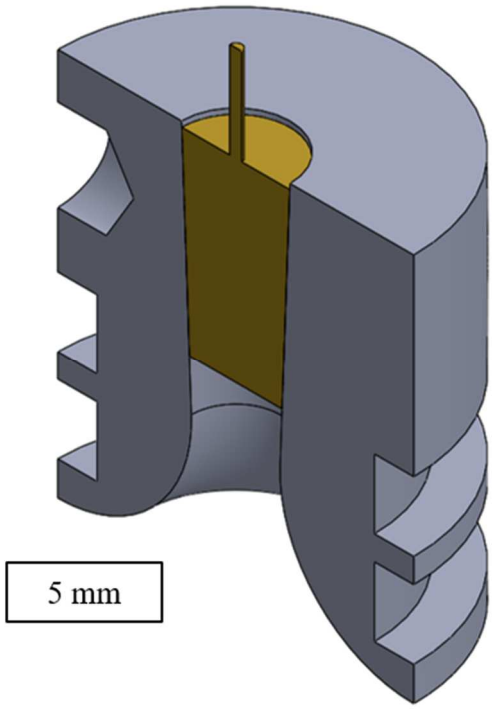

Figure 30. Nozzle Insert for Camera Alignment

Figure 31 provides a reference diagram of the measurement region with all components aligned. The black circle represents an axial view of the nozzle exit with the angular field of view focused onto the center axis. The intersecting blue laser sheet is just off axis to the lens edge in order to maximize the forward Mie scattering collection. This results in an oblique measurement region around the nozzle enter, shown in yellow. Particles passing through the exact center will be most in focus and thus produce maximum signal. Those near that focal plane can also be imaged as the streak camera integrates this entire field, however, particles furthest from the center will be well

out of focus. This benefits the technique as those velocities may not represent the desired measurement location, however they also add substantial background noise to the sample, as is shown later.

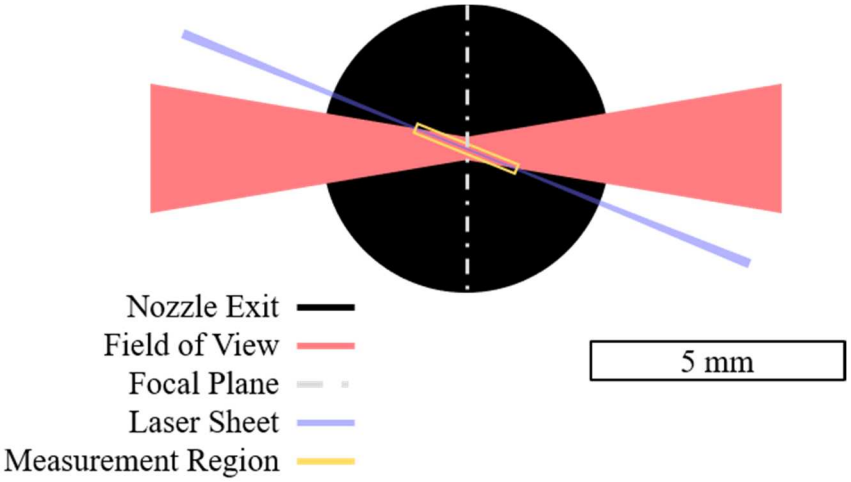

Figure 31. Particle Streak Velocimetry Measurement Region Viewed Axially Down the Nozzle

3.7 Calibration Scale

A 5 lp/mm Ronchi ruling is used as the calibration scale to correlate pixels in the spatial domain to a physical distance covered. The chrome-plated glass square is positioned across the nozzle exit, and a laser beam is used to illuminate the lines. Figure 32 shows the ruling in place with the red alignment diode, though subsequent calibration procedures used the blue diode, at just above its minimal lasing power, so that chromatic focusing effects of the collection optics would be consistent with actual streak test measurements. A sample signal averaged across time is shown in Figure 33 with corresponding peaks denoted and the linear fit displayed. The slope of the fit line provides the spatial scaling factor (y_s) for converting streak slope in pixels/pixels to velocity. Calibration images were taken at several locations across the sensor to ensure the streak camera's built-in geometric corrections properly linearize the scale. Separate files are also recorded for each day of testing as the Nikon lens was removed and reinstalled on the spectrometer and could not be returned to the exact same focus.

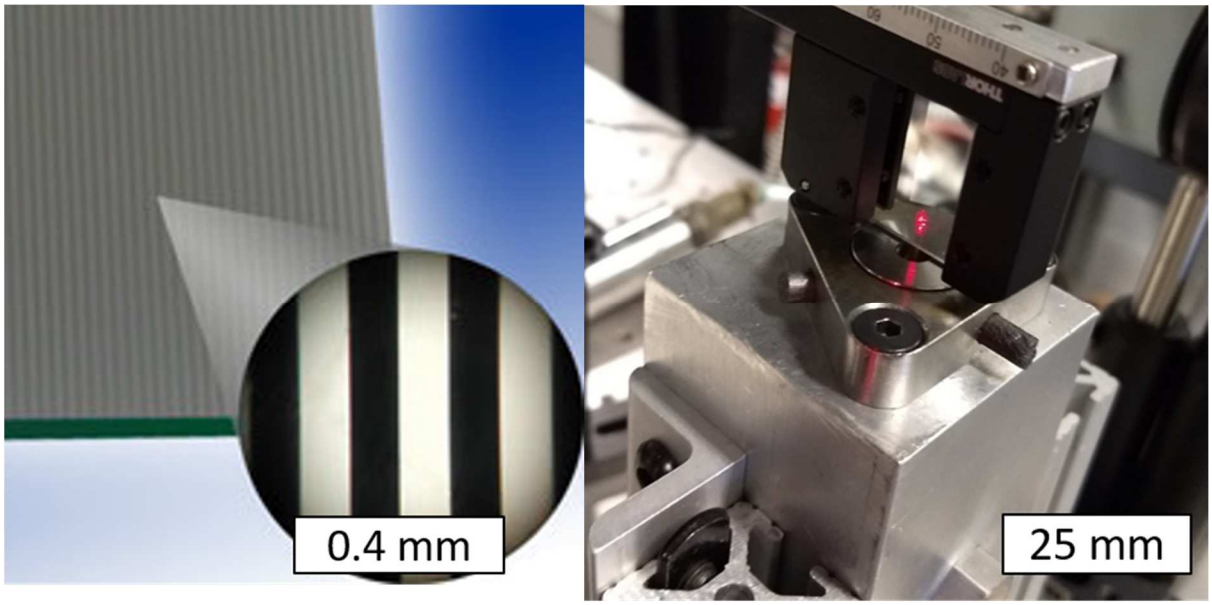

Figure 32. Example of Ronchi Ruling Surface [66] and Position over Measurement Region

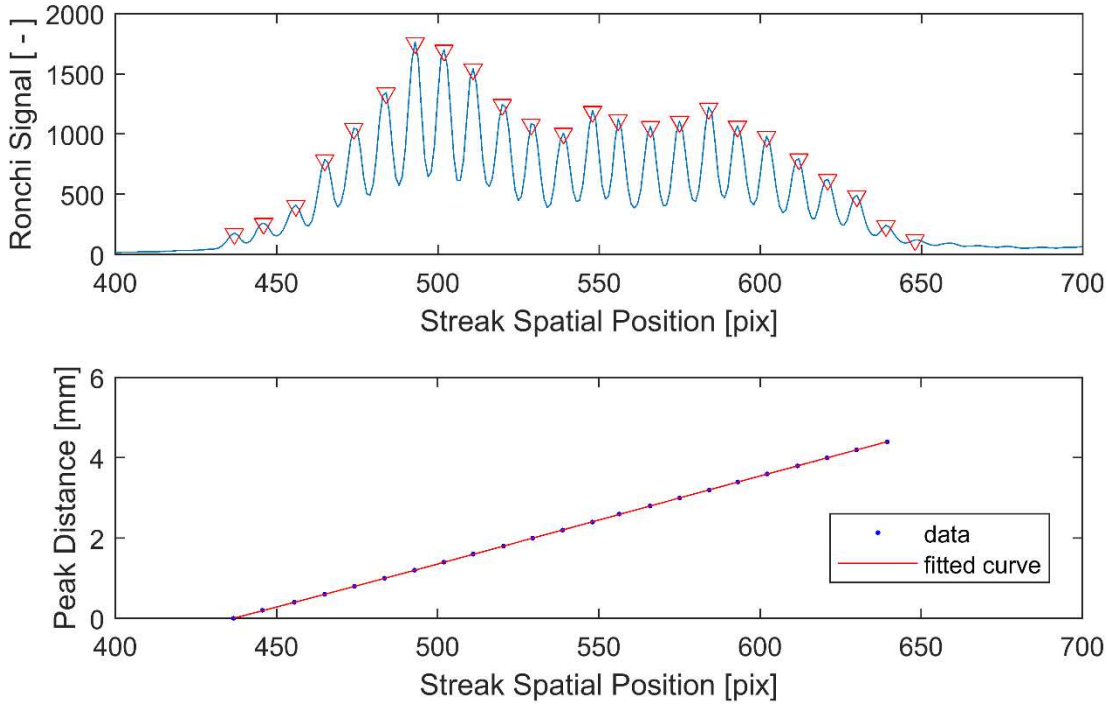

Figure 33. Sample Ronchi Spatial Calibration Signal and Fit Line

3.8 High-Speed Camera

While a traditional high-speed camera cannot track these moving particles in time, it can still be used to visualize seeder function. A Vision Research Phantom v1212 coupled with an Infinity DistaMax K2 lens operating at 10,000 fps with 98 μs exposure time provides qualitative data of the seeding density exiting the nozzle during each test. A single comparative snapshot is acquired against the entire streak camera 100 μs. The forward scattering principle is again used to maximize signal by placing a mirror downstream of the laser beam on the opposite side from the streak camera relay lens. This provides the same low incidence angle view to the v1212 such that with the blue gain maximized, particle “streaks” are easily detected.

4. RESULTS & DISCUSSION

This chapter describes the two phases of the experiment performed with PSV. The first configuration provided preliminary results and understanding for how the system behaves. Schlieren and PSV were performed on the nozzle flowing nitrogen with SiO_2 seed particles. Reiteration on the design based on those findings led to the second experiment performed with TiO_2 particles flowing in pure nitrogen and a mix of nitrogen and helium.

4.1 Initial Particle Streak Velocimetry Development

This section is modified from a paper presented at the *53rd AIAA/ASME/SAE/ASEE Joint Propulsion Conference*, July 2017, AIAA 2017-4680. It is intended to preface the most current developments and results discussed in Section 4.2. System configurations discussed here represent only those which deviate from the configuration described in Chapter 3; mainly the collection optics and data analysis. The nozzle test article and seeder correspond to those described above.

Jared D. Willits and Timothée L. Pourpoint
Purdue University, West Lafayette, IN, 47907
School of Aeronautics & Astronautics, Purdue University,
500 Allison Rd., West Lafayette, IN 47906, USA

In order to troubleshoot and validate this novel technique against existing velocimetry measurements, a system using cold nitrogen has been designed and tested both with Particle Streak Velocimetry and schlieren imaging. Schlieren measurements taken at several locations beyond the exit of a supersonic nozzle were correlated to velocities ranging from 479 to 490 m/s. Particle streak measurements illuminated by a laser diode at identical locations indicated velocities ranging from 380 to 430 m/s. The measurements demonstrated a particle to flow velocity ratio between 77 and 88 %, less than the predicted 93% from Stokes flow based on the particle diameter of 1 μm.

4.1.1 Particle Lag

For a given nozzle geometry, the gas velocity is solved numerically by the area ratio at each location assuming 1-D isentropic flow with knowledge of flow stagnation temperature and ratio of specific heats. The present analysis provides only an order of magnitude of the velocity uncertainty to select particle diameter and density. Nitrogen stagnation conditions were updated to match measurements during tests, and the model is initiated with ϕ=1 at the beginning of the nozzle contraction. Figure 34 shows the particle and fluid velocities as well as ϕ indicating the quality of the particle in accurately following the fluid velocity. While a value greater than 95% is desirable for velocimetry measurements, the 93% provided by the current seed material at the nozzle exit still provides valuable insight into PSV during development.

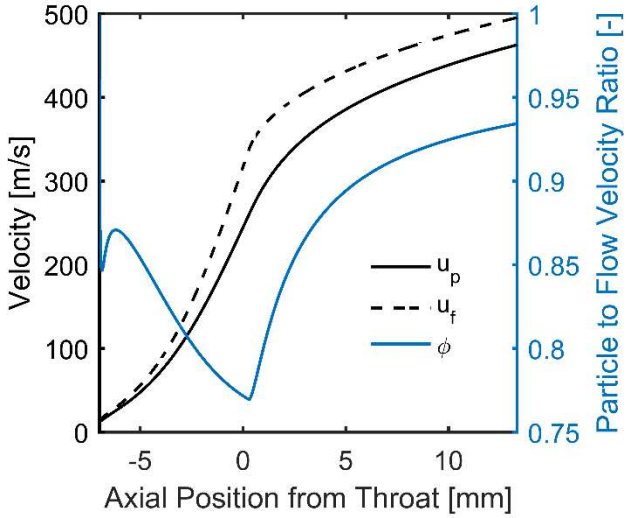

Figure 34. Predicted Particle and Fluid Velocity through the Nozzle
(d_p = 1.0 µm, P_0 = 115 psia, T_0 = 290 K)

4.1.2 Particle Seeding

Several iterations of both the seeder and seed material were required to achieve the desired seeding density and minimum particle size. Seed options investigated were TiO_2, SiC, and SiO_2 with the desired traits of uniform size and shape as well as a high refractive index to maximize signal are also desired. Seeder operation is characterized by sweeping a piece of carbon tape across the nozzle exhaust and analyzing it in a desktop SEM. Results show that the TiO_2 and SiC samples used cause extensive agglomeration that is not broken up by the sonic orifice. This was attributed to strong inter-particle forces due to their non-uniform, non-spherical shapes allowing tightly packed

clusters to form. Figure 35 shows an SEM image of a SiC agglomeration that broke apart only after impacting he tape sample at the nozzle exit. In contrast, 1.0 µm spherical SiO_2 samples from Alfa Aesar (Part # L16986) show no agglomerations and qualitatively even seeding density on the tape samples as demonstrated in Figure 36.

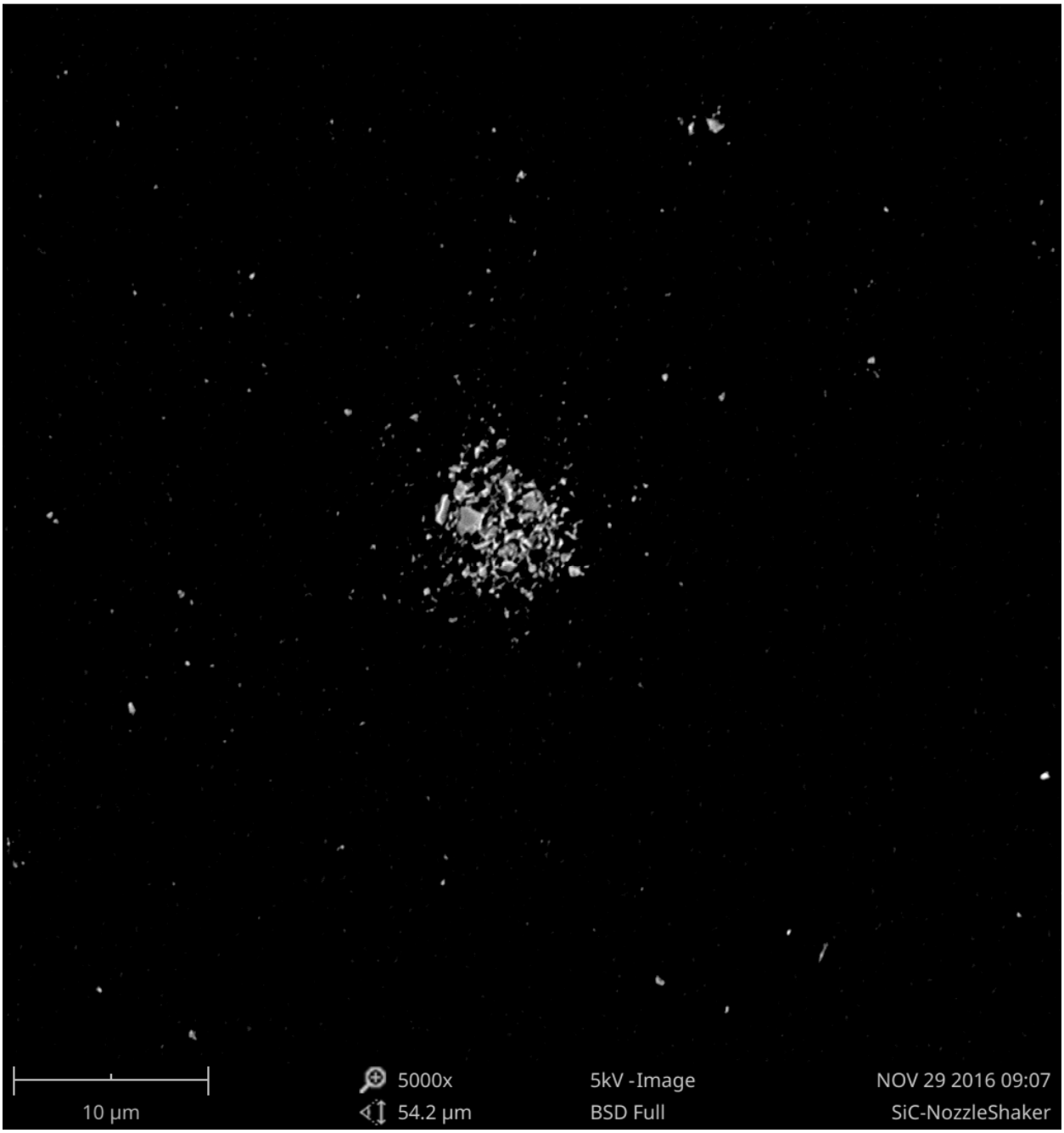

Figure 35. SEM of SiC Collected from Nozzle Exhaust

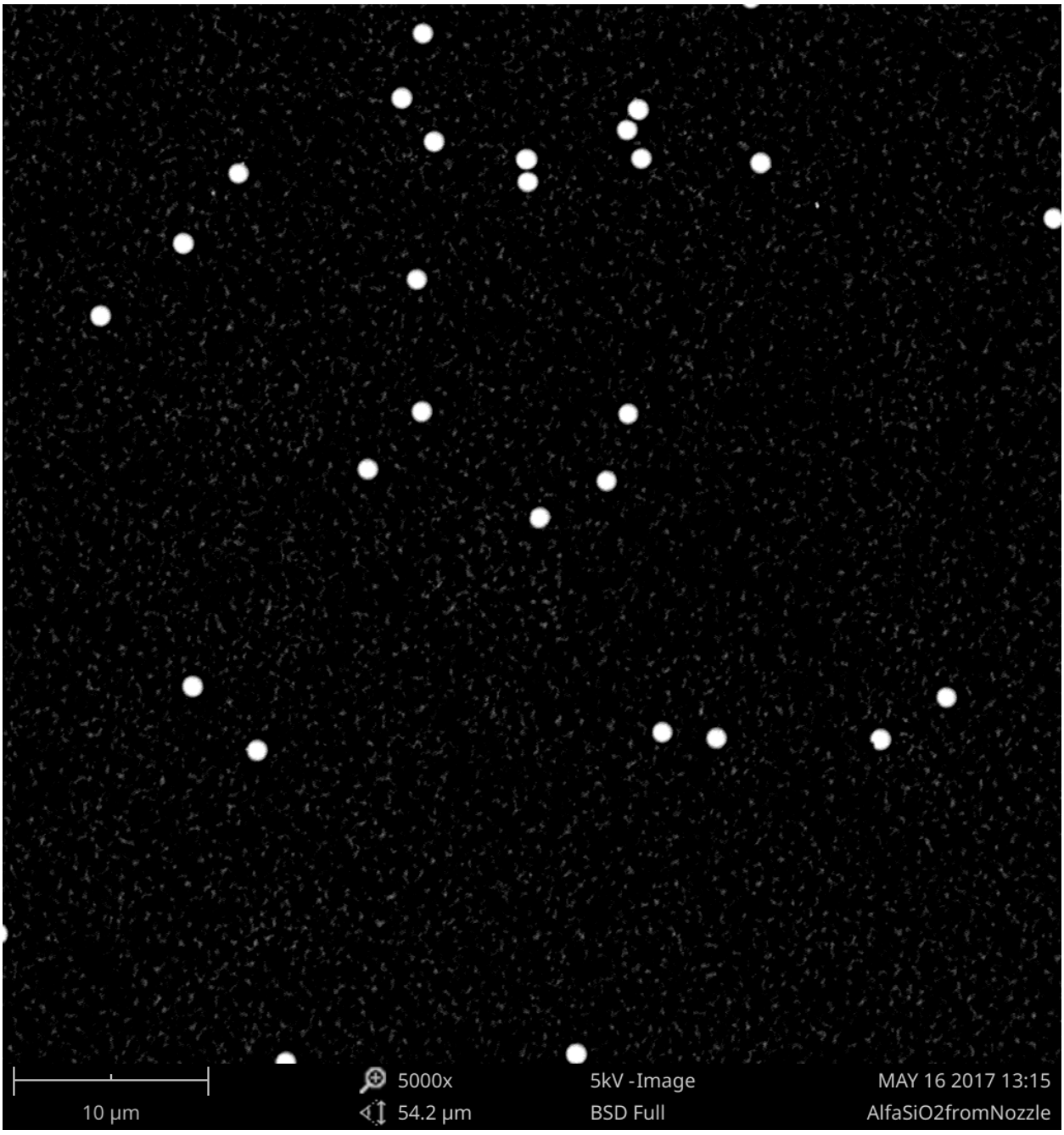

Figure 36. SEM of SiO_2 Collected from Nozzle Exhaust

4.1.3 Streak System Components and Layout

Figure 37 shows a diagram of the measurement setup. The diode is oriented with the long axis vertical. The collimated line output is focused into a thin sheet by a 150 mm focal length cylindrical lens. A plane mirror positioned behind the test article is used to direct the beam. The horizontal

waist is located at the nozzle center line with the sheet height being approximately 5 mm and positioned vertically at the nozzle exit plane. A 75 mm focal length spherical lens collects the scatter and focuses it 1:1 onto a micrometer slit. This acts as a field stop to limit the width of the measurement region allowing control of the number of particles being imaged, total light intensity, and spatial resolution about the nozzle center axis. A dove prism rotates the image 90° to align with the streak camera photocathode orientation. A 200 mm f/4 macro Nikon lens is used to collect the image. As delivered, the system includes a UV-Vis spectrometer, but for the purposes of this experiment, this is bypassed by setting the diffraction grating to a zero-order reflection which will act as a plane mirror directing the signal into the streak camera.

1. 450 nm Laser Diode
2. Cylindrical Lens (Sheet)
3. Mirror (Alignment)
4. Nozzle Exit
5. Spherical Lens (Collection)
6. Micrometer Slit (Stop)
7. Dove Prism (Rotation)
8. 200 mm Macro Lens
9. Spectrometer @ 0 nm
10. Streak Camera
11. Beam Dump

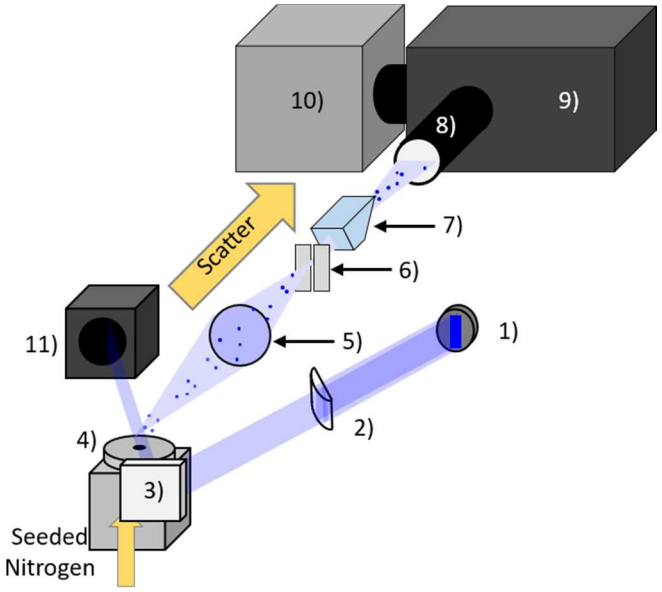

Figure 37. Cold Gas Test Bed Schematic for Initial Streak Experiments

4.1.4 Focus and Calibration

The spatial scale of the laser sheet within the streak camera signal is found by placing a needle at the measurement location and raising it incrementally with a 120 thread per inch, ultra-fine screw. Figure 38 shows a range of samples overlain with equivalent edge locations identified by black squares representing one thread graduation. The mean y-scale (y_s) has been found to be 13.7±0.8 µm/pixel. Focus at the image plane is achieved by qualitatively maximizing the signal intensity and peak sharpness via the position of the 75 mm lens and the focusing ring of the 200 mm lens assembly.

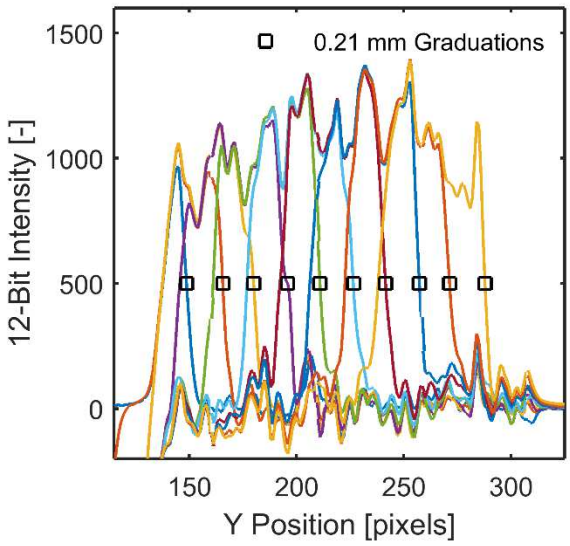

Figure 38. Spatial Signals and Edge Fit Markers
from Incrementally Raised Needle for Y-Axis Calibration

4.1.5 Image Processing

While the eventual goal of this work is to provide 1-D spatially and temporally resolved flow velocity data, the initial testing presented here is assumed to be measuring a field at steady state, which is small enough to ignore spatial variance. This allows for bulk analysis of several streaks within the image to find a mean value with higher signal to noise. Processing of the streak data is accomplished using a CSFT, which transforms the spatial domain image into constituent horizontal and vertical frequency components.

Shown in Figure 39, the region of interest containing particle streaks is cropped from the 1360 by 1024 pixel, 12-bit, raw CCD image. The region is padded to a square to preserve the angles and the CSFT is performed, shown in Figure 40. The location of the maxima in each column of the CSFT are found. The coordinates of the peaks are transposed to account for the perpendicular shift between the spatial lines and frequency domain lines, and a linear fit for these points is found, as in Figure 41. Figure 42 shows the original region of interest with lines of slope equal to the linear fit scaled by the spatial and temporal scaling factors, y_s and t_s, overlain to demonstrate the accurate fit to the major streak signals.

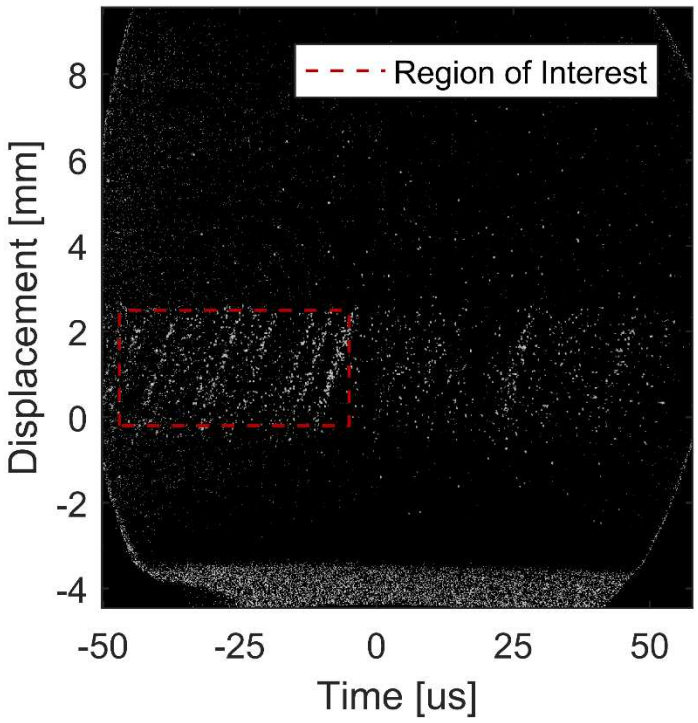

Figure 39. Raw Streak Image with Region of Interest Indicated

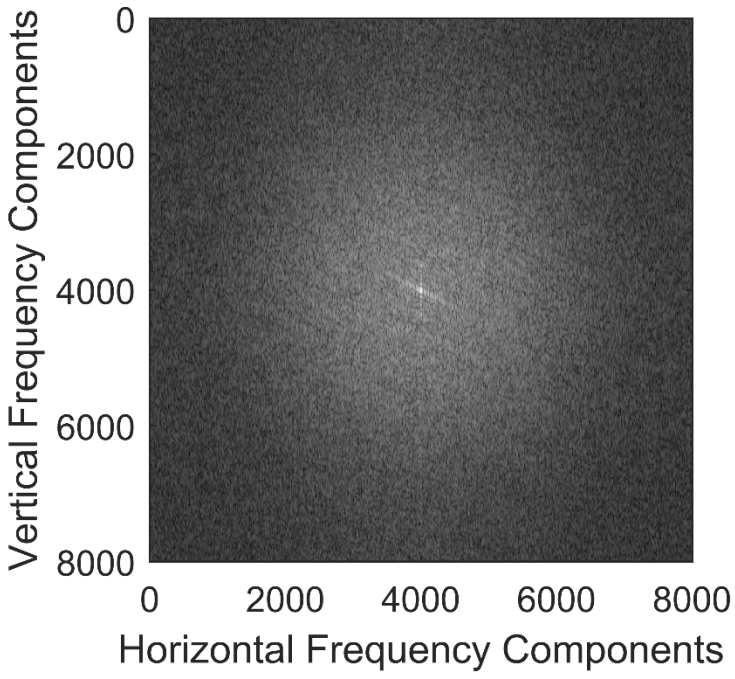

Figure 40. CSFT of Streak Region of Interest

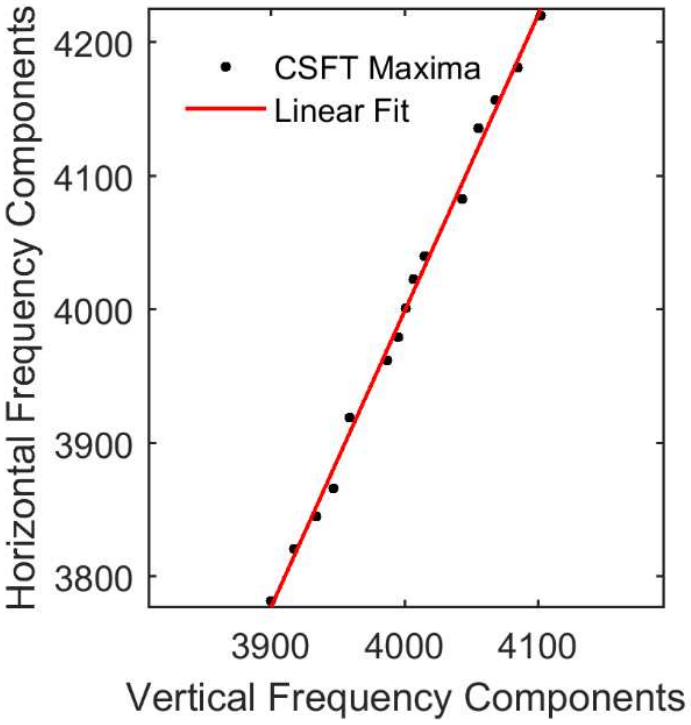

Figure 41. Linear Fit of Maxima in Streak CSFT

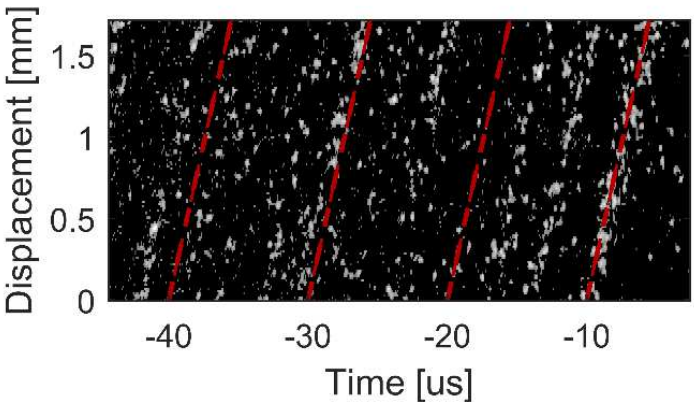

Figure 42. Streak Image Region of Interest with Demonstrative Fit Velocity Lines Overlain

4.1.6 Nitrogen Schlieren Imaging Tests

Schlieren imaging of the nozzle plume provides baseline velocity data of the cold gas thruster with a traditional velocimetry technique against which to compare the PSV results. The technique visualizes density gradients in the flow via variations in the refractive index. Mach waves propagating through the nozzle as the gas expands produce these variations and can be correlated to the local Mach number by Equation 30, where the Mach angle (θ_M) is measured between the flow direction and these disturbances. The flow is assumed to be axial very near the center line where the samples are obtained. Left and right running lines provide two locations to sample and average to account for imperfect alignment of the camera to the flow field.

$$M = 1/sin\theta_M \tag{30}$$

The schlieren measurement uses a lens-type system as shown in Figure 43 [67]. The nozzle is directed upward through the test section, and the screen is replaced with a high-speed, Vision Research Phantom v1212 camera to record images of the plume with an Infinity K2 DistaMax lens producing ~2x magnification. The 150 mm focal length schlieren objective lenses provide a 50 mm circular test section, and the illumination is provided by a 1.2 W radiant flux, SugarCUBE LED.

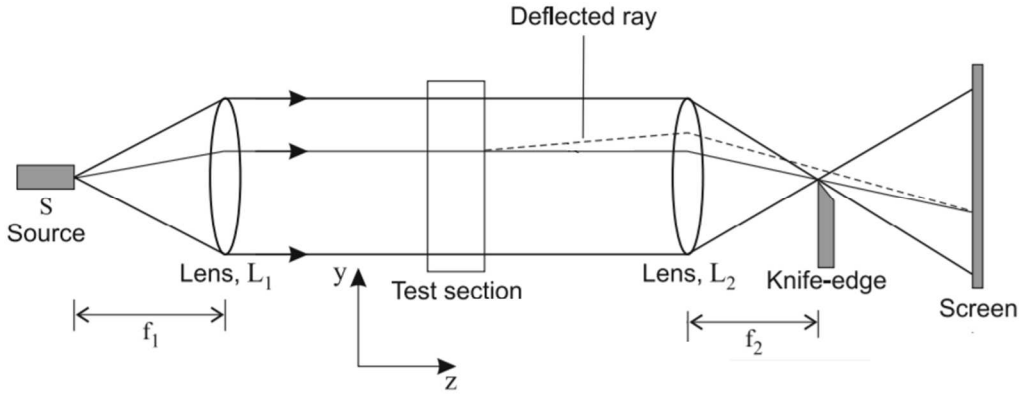

Figure 43. Example Lens-Type Schlieren Schematic [67]

The analysis method employed to find this angle resembles that described in Section 4.1.5 in analyzing the PSV data. A CSFT is productive in this instance both because the angle of the primary elements of the image are of interest, and despite maintaining their angle, the Mach wave locations oscillate from frame to frame. This renders exposure stacking in the spatial domain less

effective. By stacking the frequency domain results which are all referenced to the spectrum center, a sharper average appears, and the dominating peaks are far easier to detect. The initial slope estimation via the CSFT peaks is sufficient to obtain the mean Mach angle for these baseline tests.

Figure 44 displays a sample ROI for analysis of the schlieren images. Forty CSFT spectra acquired over 200 ms are stacked to produce an average sample. One sample spectrum is displayed in Figure 45. The local maxima of the mean sample are then fit with left and right running linear regression lines, as in Figure 46, and θ_M is obtained from the arctangent of the fit line slope. Figure 47 displays the original sample frame with the overlain fit lines, which satisfactorily identify the dominant angles in the ROI. With the Mach number calculated in the plume, predicted gas velocity for each streak test can be specified through Equation 31 by measuring stagnation temperature in the nozzle holder given γ and molecular weight of the gas. This method is limited in that it does not account for non-isentropic features occurring within the nozzle which produce non-uniform properties at the nozzle exit. Shocks or simply enough sequential small Mach waves could skew the exit temperature from that calculated from the stagnation temperature though these are assumed to be small effects. Further fidelity could be achieved in the future by incorporating additional scaling based on literature for conical nozzles or CFD analyses of these flows.

$$v_f = M\sqrt{\frac{\gamma R u T_0}{MW\left(1+\frac{\gamma-1}{2}M^2\right)}} \qquad 31$$

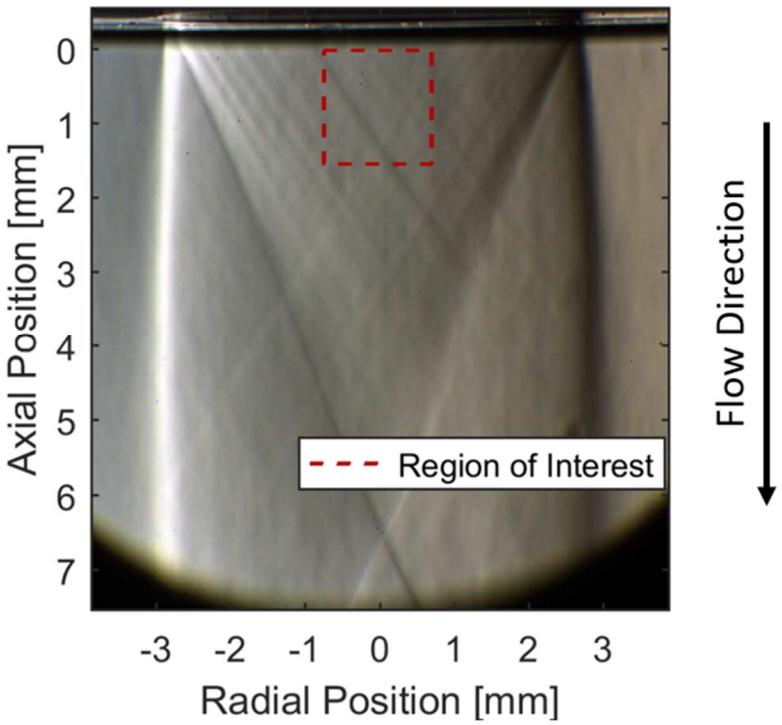

Figure 44. Raw Schlieren Image with Region of Interest Indicated

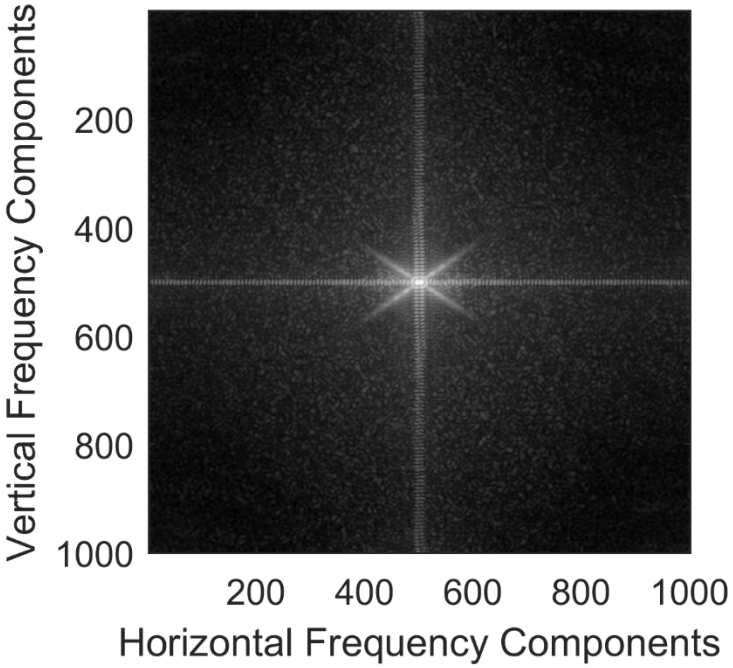

Figure 45. CSFT of Schlieren Region of Interest

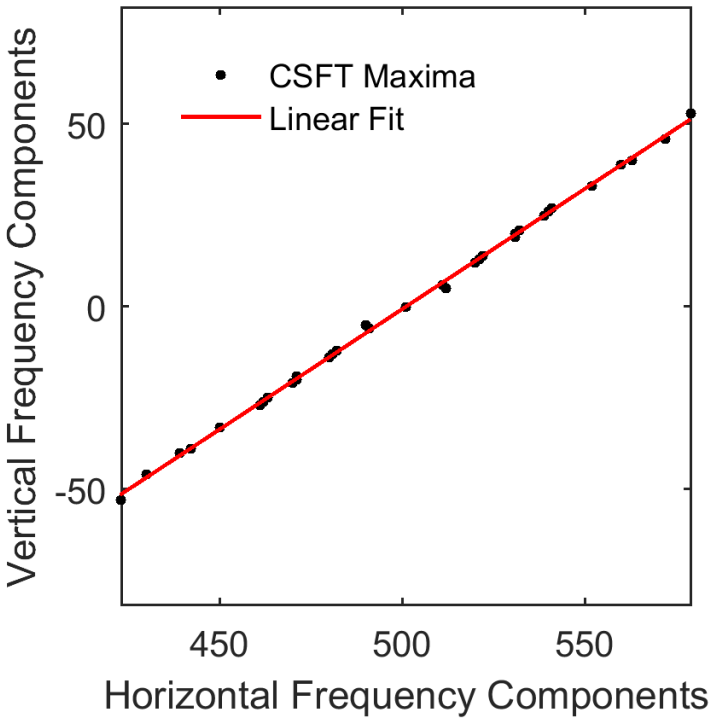

Figure 46. Linear Fit of Left Going Maxima in Schlieren CSFT

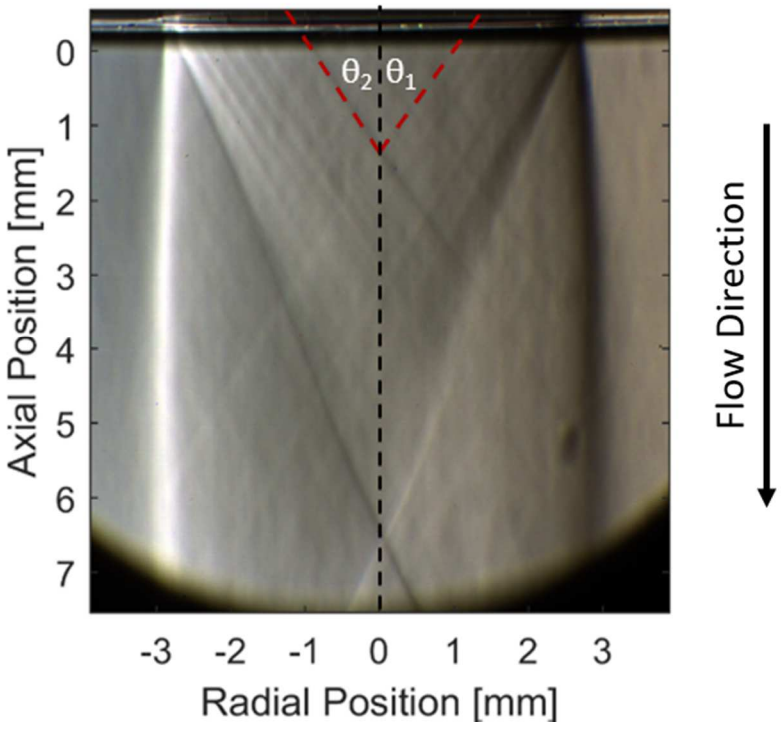

Figure 47. Region of Interest with Demonstrative Fit Mach Lines

Schlieren data of the nitrogen plume was acquired at three locations. Table 5 lists the distance from the nozzle exit of the sample and the corresponding fit Mach angles. The non-sequential test numbers reflect that schlieren measurements were performed between streak tests to best estimate the flow velocity given the current state of the system. Schlieren and streak recordings could not be performed simultaneously because stray reflections from the LED wash out the particle scatter collected by the streak camera. With the estimated Mach numbers at each *h* location, flow velocity for the streak measurement tests were adjusted for the measured temperature. At the nozzle exit, all tests indicate a flow velocity of approximately 480 m/s and an uncertainty (ε_f) of ±13 m/s based on the goodness of fit of the linear regression and the temperature measurement uncertainty. The exit Mach number is lower than the predicted 1.83 shown in Figure 2, which is to be expected with viscous losses, a conical nozzle, and other real-world effects not accounted for in the isentropic flow analysis based on throat and exit diameter. Test 10 was run without seed particles present to demonstrate that no detectable loss of flow momentum is caused by accelerating and carrying the seed particles in tests 11, 12, and 16 at the same location. Because the flow is slightly underexpanded given the stagnation pressures recorded and the expansion ratio of the nozzle, some slight acceleration is observed in tests 19 and 22 as expected when moving away from the nozzle exit.

Table 5. Summary of Schlieren Test Data for Nitrogen Flow

Test Number	Seeder On	h [mm]	θ_M [°]	M [-]	T_0 [K]	v_f [m/s]	(ε_f)
10	No	0.00	34.7	1.76	290	480	(13)
11	Yes	0.00	34.9	1.75	290	479	(13)
12	Yes	0.00	34.8	1.75	290	479	(13)
16	Yes	0.00	34.7	1.76	290	480	(13)
19	Yes	2.54	33.6	1.81	291	489	(13)
22	Yes	1.27	34.0	1.79	289	484	(13)

4.1.7 Nitrogen Streak Tests with SiO_2

Streak samples using 1 μm SiO_2 seed particles were collected across multiple days and at several vertical positions above the nozzle. All tests were run with a nozzle stagnation pressure (P_0) of 115 psia and a seeder pressure of 300 psia. The summary of test conditions and results for the streak samples are shown in Table 6. No test shows a velocity lag within the specified uncertainty matching the 93% value predicted by the model at the nozzle exit. The largest contributor to the reported uncertainty in v_p (ε_p) is the streak linear fit slope (m_{st}). The scaling factors for time (t_s) and space (y_s) make up a much smaller portion. Values of ε_p range from ±4 to 24 m/s or ±1 to 6%. Measured stagnation temperature (T_0) varied somewhat from test to test due to cooling of the feed lines by the gas expansion and day to day fluctuations in ambient temperature. However, by comparing velocity ratios (ϕ) of the particles to their corresponding flow prediction, rather than particle speed, this variation should be addressed.

Table 6. Summary of SiO_2 Streak Data for Nitrogen Flow

Test Number	Test Day	h [mm]	T_0 [K]	v_p [m/s]	(ε_p)	v_f [m/s]	ϕ [-]	(ε_ϕ)
1	1	0.00	288	365	(13)	478	0.76	(0.03)
2	1	0.00	289	348	(10)	478	0.73	(0.03)
3	1	0.00	287	356	(13)	477	0.75	(0.03)
4	2	0.00	294	380	(14)	483	0.79	(0.04)
5	2	0.00	293	380	(11)	482	0.79	(0.03)
6	2	0.00	293	373	(16)	482	0.77	(0.04)
7	2	0.00	293	375	(5)	482	0.78	(0.04)
8	2	0.00	294	405	(18)	482	0.84	(0.04)
9	2	0.00	293	395	(20)	482	0.82	(0.05)
13	3	0.00	290	389	(15)	479	0.81	(0.04)
14	3	0.00	291	383	(4)	479	0.80	(0.02)
15	3	0.00	290	387	(13)	479	0.81	(0.04)
17	3	0.00	289	384	(17)	478	0.80	(0.04)
18	3	2.54	292	433	(12)	490	0.88	(0.03)
20	3	2.54	290	415	(8)	488	0.85	(0.03)
21	3	1.27	290	412	(16)	485	0.85	(0.04)
23	3	1.27	286	420	(24)	481	0.87	(0.06)

Noticeable trends in ϕ with respect to test day and sample position above the nozzle are illustrated in Figure 48. The three samples from day 1 are the slowest among all samples. All other parameters recorded in those tests, besides the fitted slope, appear to fall in nominal ranges amongst the other similar tests. It is likely that after aligning the system, some piece was incidentally shifted, and this was not corrected until preparing the system for the second test day and preserved through to the third day. No other parts of the system, such as the seeder, were reviewed or altered between test days.

The other key trend is the evidence that between positions 0 and 1.27 mm, the particles are still significantly accelerating to the flow velocity. Although the schlieren data shows that v_f is accelerating along that interval, the velocity ratio, not just the particle velocity, still recovers almost 5% of the lag before leveling back out between 1.27 and 2.54 mm. Several possibilities exist to explain this trend:

- It is possible that the particle lag model described above is over-predicting the flow following capability. By the end of the nozzle, the model predicts less than 1% lag recovery per mm. Whether it is due to how spherical the particles are or the Reynolds flow regime the particle falls under or some other assumption, the model may underestimate the distance required to accelerate the particle up to the desired velocity ratio. If an extra 1 mm can produce that acceleration, then perhaps the whole nozzle could be made longer to account for perceived latency relative to the model.

- Alternatively, the distinct change in lag could show that the particles are responding very quickly to the flow, but some other contributing factor in the alignment or scaling causes this actual flow acceleration to be perceived differently than by the schlieren observations.

In either case, finer steps between locations and better resolved measurements at intermediate positions within one CCD image will help provide a clearer picture of what is causing the lower than expected velocity ratio in future works. Additionally, smaller diameter particles will be investigated to move beyond the threshold case defined by the lag model.

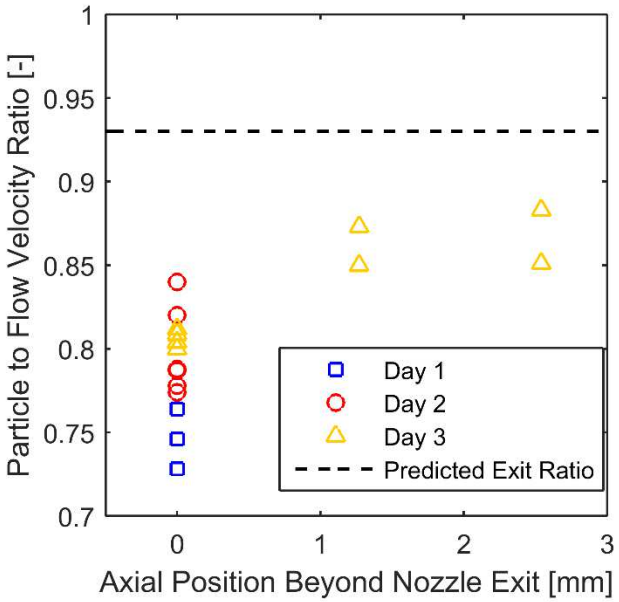

Figure 48 . Streak Particle Velocity Ratio vs. Sample Location and Test Day

4.2 Current Particle Streak Velocimetry Diagnostic Status and Applications

In response to the results obtained in the previous section, an alternative seeding powder was obtained, and the optical imaging system was reconfigured to the status described in Chapter 3. The added degrees of freedom in positioning and alignment of components, optimized use of forward Mie scattering, increased laser power, and elimination of inefficient optical elements drastically improved the magnitude and sharpness of the collected data.

4.2.1 Second Seeding Survey

Results in Section 4.1.7 show that 1 μm SiO_2 fail to accelerate to the expected nozzle exit velocity. A new survey of seed samples was then performed to find a suitably smaller particle which could still be delivered in consistent sizes and concentrations. Though the SiO_2 did show good disaggregation behavior, other materials were included under the circumstance that smaller diameter SiO_2 might not be manufactured in spherical form. Candidates identified and acquired from US Research Nanomaterials, Inc. were SiO_2, Al_2O_3, ZrO_2, and TiO_2 with the respective quoted sizes and other material properties listed in Table 7.

Table 7. Second Seed Survey Sample Properties

Material	ρ_p [kg/m^3]	Melting Point [K]	n_p @450 nm [-]	Quoted d_p [nm]	Predicted ϕ_e in N_2 [-]
Al_2O_3	3970	2318	1.779 [68]	300	0.99
Al_2O_3	3970	2318	1.779 [68]	500	0.98
SiO_2	2650	1983	1.466 [43]	400	0.99
TiO_2	4230	2116	2.813 [69]	300	0.99
TiO_2	4230	2116	2.813 [69]	500	0.98
ZrO_2	5890	2988	2.197 [70]	200	0.99

Simulations of particle lag for each sample entrained in the nitrogen cold gas nozzle are shown in Figure 49. The four samples equal to or below 500 nm diameter show ideal response at up to 99% flow following accuracy, however, as particle size is reduced, so is its ability to scatter light to the streak camera, so the 500 nm samples of Al_2O_3 and TiO_2 were tested, as well.

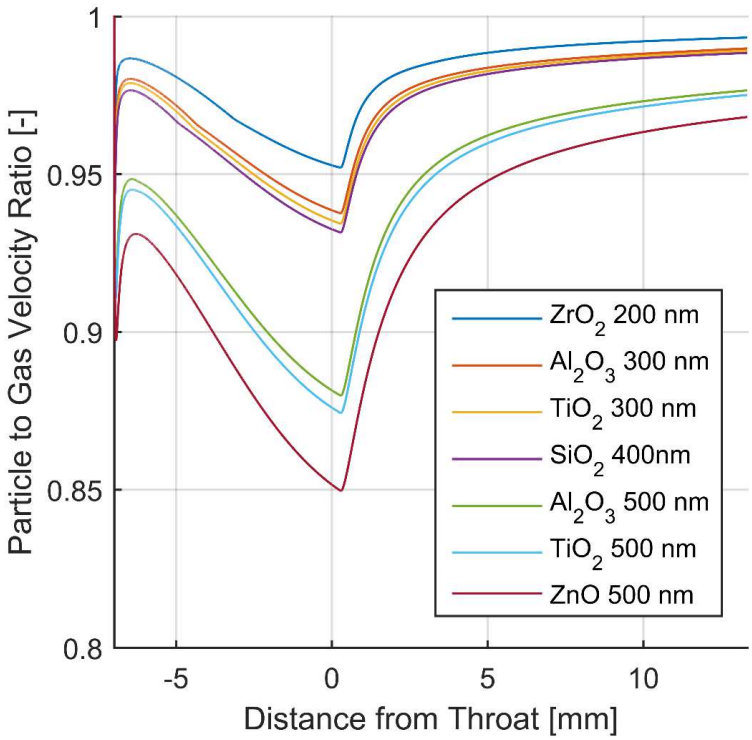

Figure 49. Predicted Lag Response of Seed Powders in Second Survey

After receipt of the samples, the SEM was used to assess the uniformity, size, and shape of each sample relative to its quoted characteristics from the manufacturer. The Al_2O_3 and SiO_2 bulk samples, shown in Figure 50, Figure 51, and Figure 52, each display substantial variation in particle size with many outliers on the order of 5 μm or more. While the seeder is designed to filter grossly oversized particles, a large concentration still raises the risk of passing enough particles through and contaminating the streak measurement with brighter, slower streaks. Additionally, the SiO_2 and 500 nm Al_2O_3 appear jagged and very non-spherical. The straight faces contribute to particle agglomeration as more surface area is available for the inter-particle forces to act over and tighter packing of clusters can also occur. The particle lag model relies on a spherical assumption to calculate the drag coefficient and predict response, so its utility in predicting performance is also hindered. Conversely, the ZrO_2 sample displayed in Figure 53 appears to show an abundance of undersized particles. The SEM was unable to resolve constituent particles within the displayed clusters. While small particles are desirable for flow following, minute particles that are too small to image, but are introduced to the flow in great quantities, add background noise.

The TiO_2 300 nm and 500 nm samples present by far the most ideal distribution of the available materials. While the wide views in Figure 54 and Figure 56 show the particles clustered together, and some into very large agglomerations, the less jagged shape observed at the higher magnification in Figure 55 and Figure 57 makes it far more likely that the seeder is able to break them apart into the constituent sizes. However, the less-spherical nature of these particles relative to the SiO_2 sample used initially raises some concern about the accuracy of the Stokes drag coefficient applied in the lag response model. Further fidelity could be achieved by investigating corrected factors for elongated shapes, though because this analysis is primarily a first-order estimate, analysis of this correction was deferred. The variation of particle diameters within the clusters appears relatively uniform around the 300 nm and 500 nm quoted sizes. In order to maximize particle response, the 300 nm sample was selected for initial evaluation, and was used for the remainder of this experiment.

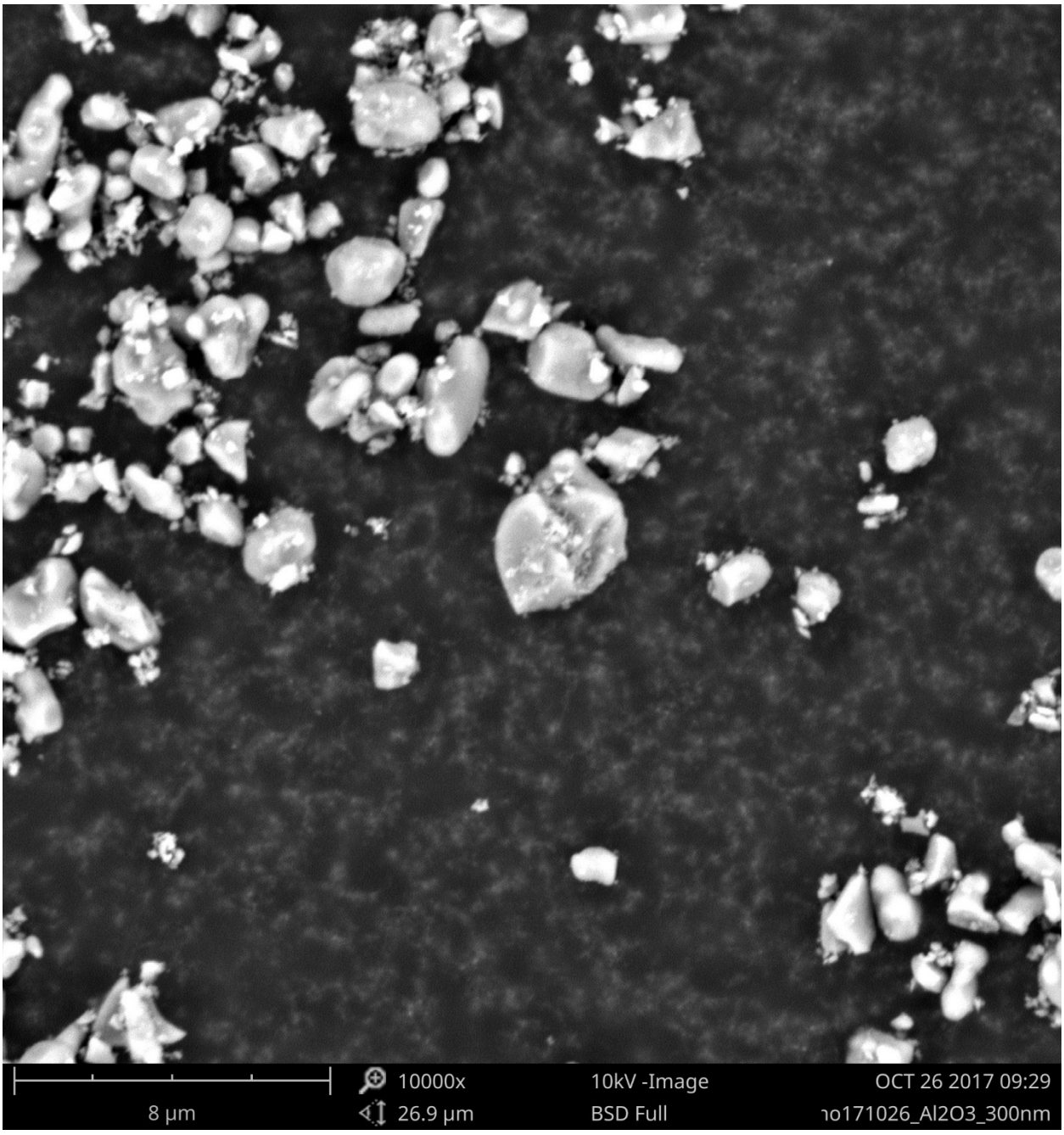

Figure 50. Al_2O_3 300 nm Bulk Sample SEM

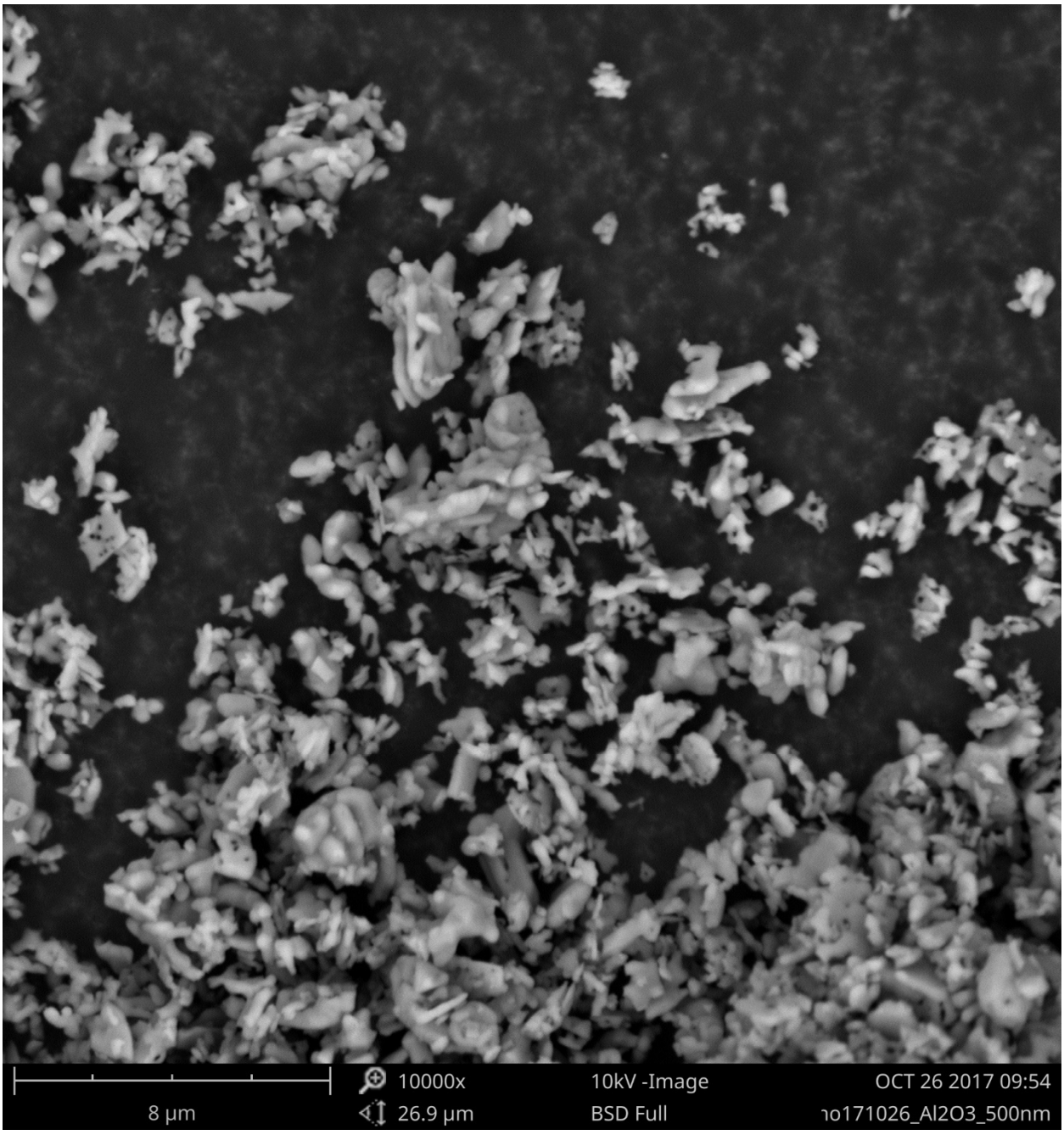

Figure 51. Al_2O_3 500 nm Bulk Sample SEM

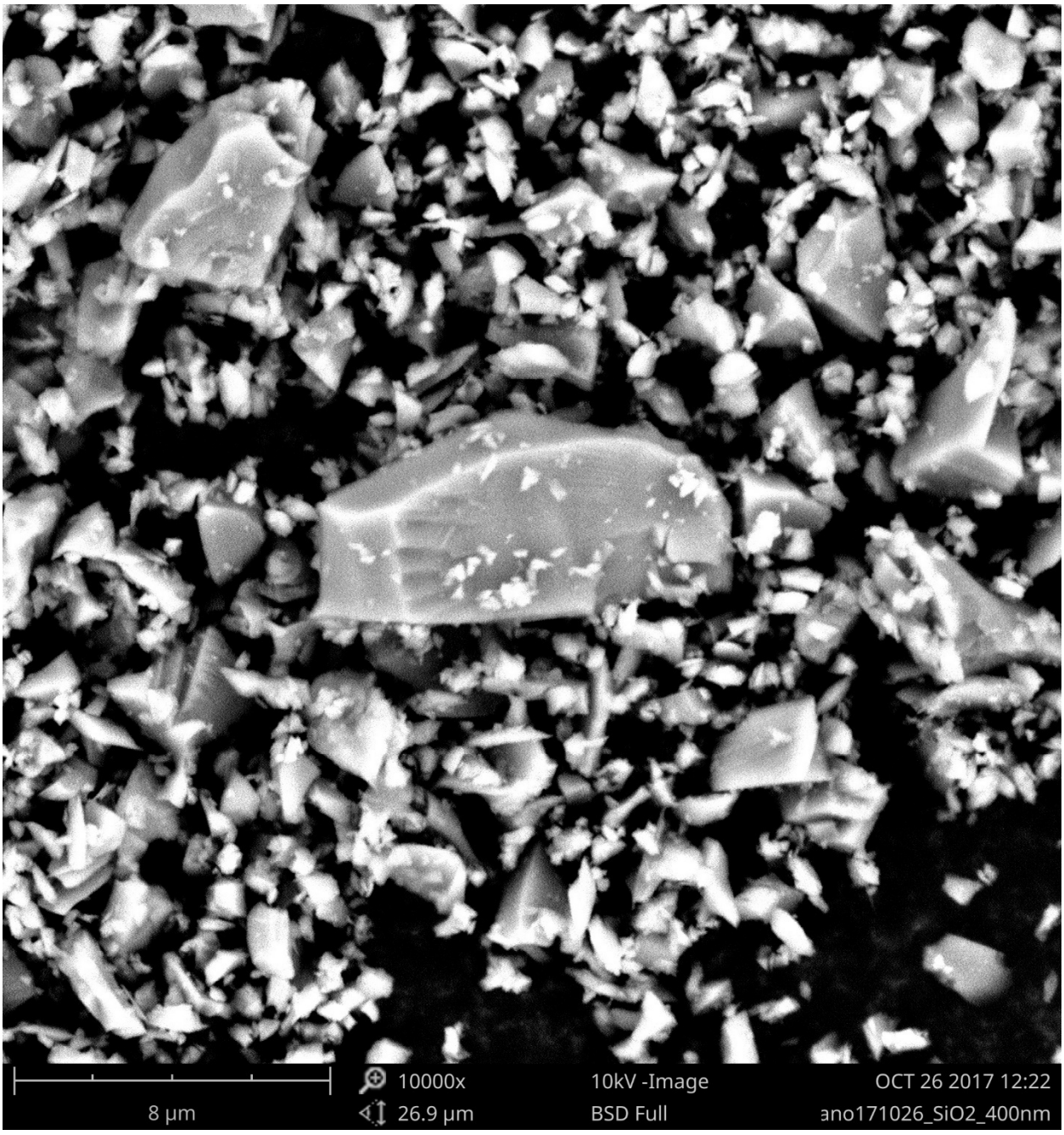

Figure 52. SiO_2 400 nm Bulk Sample SEM

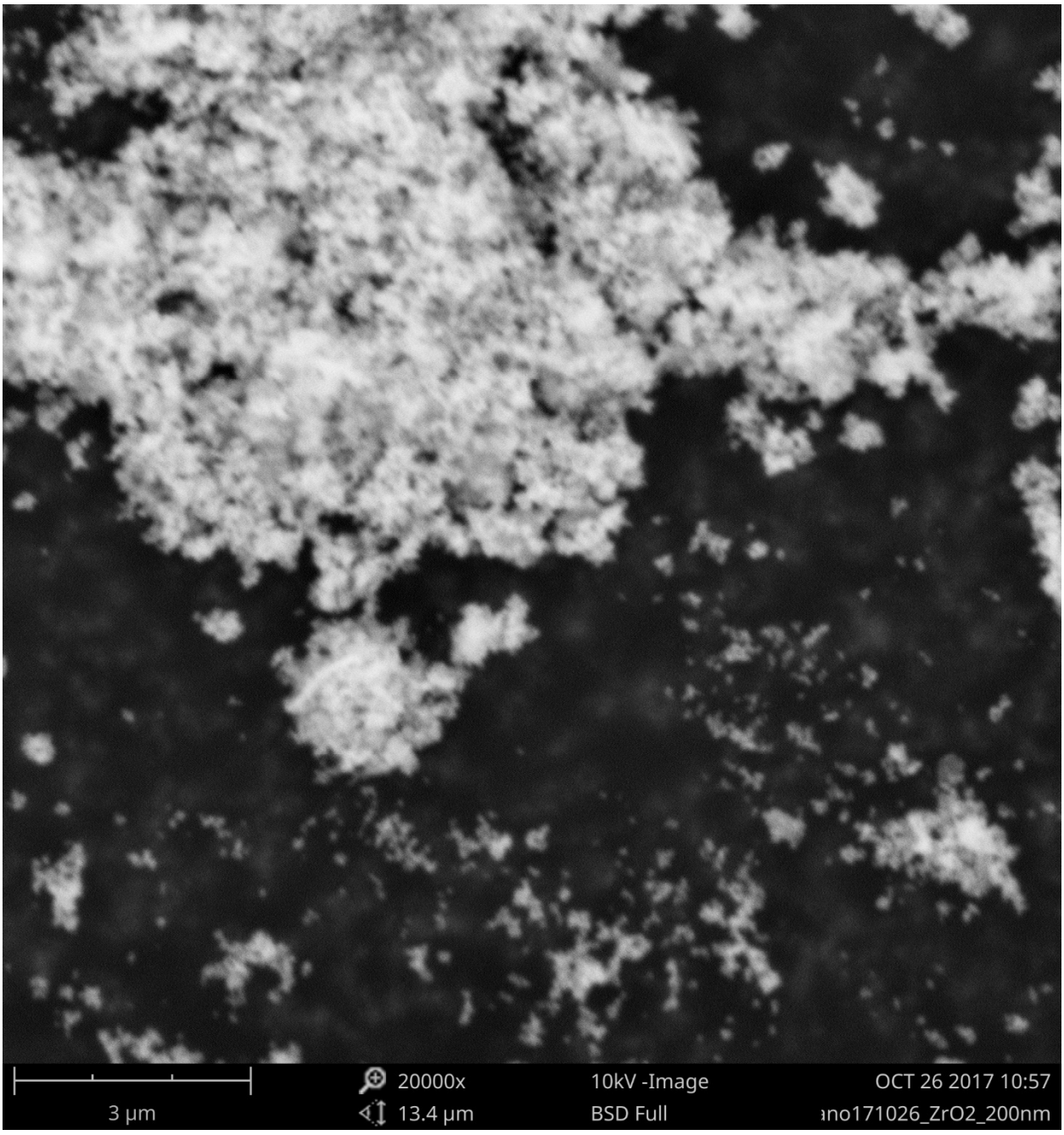

Figure 53. ZrO_2 200 nm Bulk Sample SEM

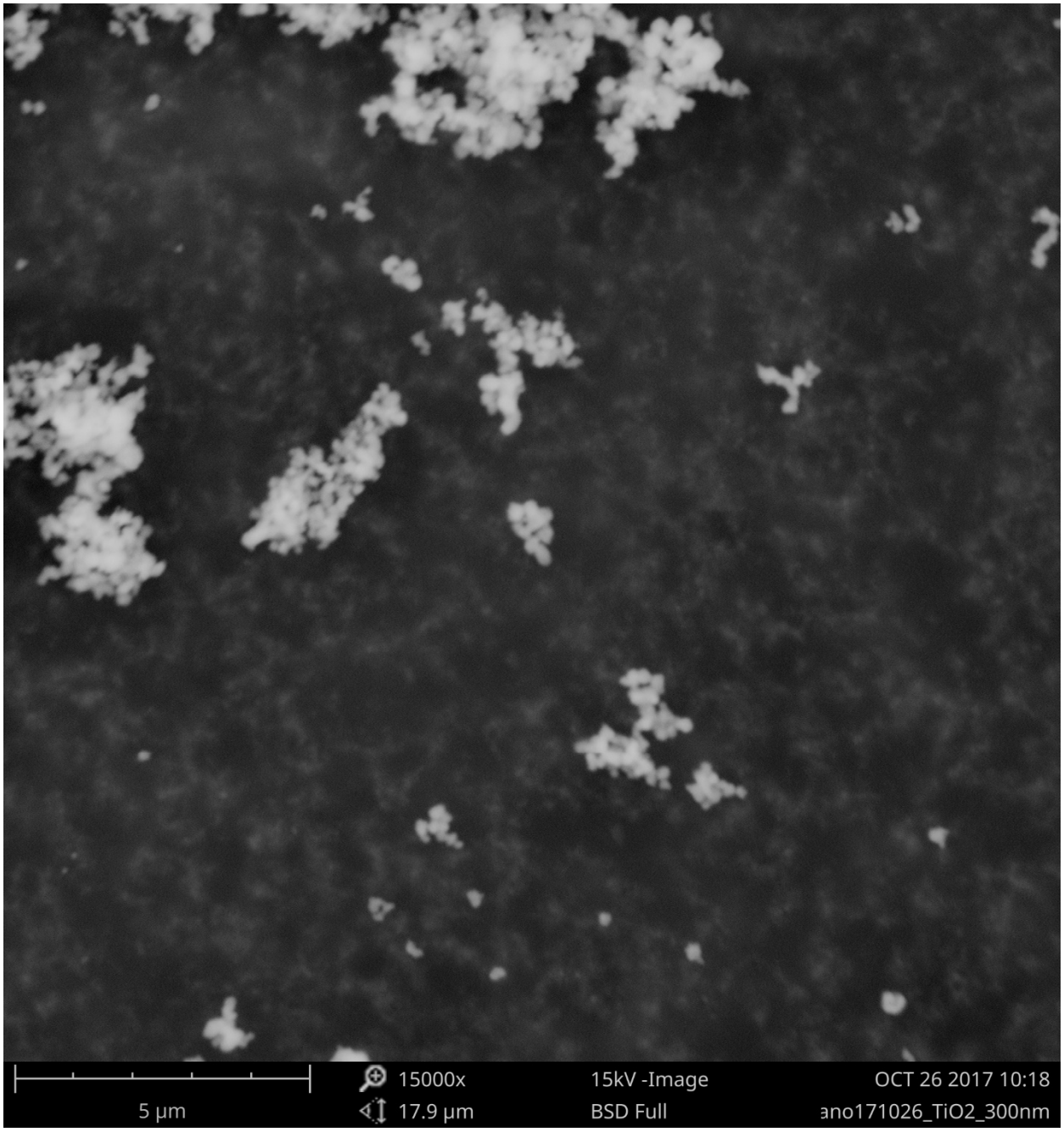

Figure 54. TiO_2 300 nm Bulk Sample SEM Wide View

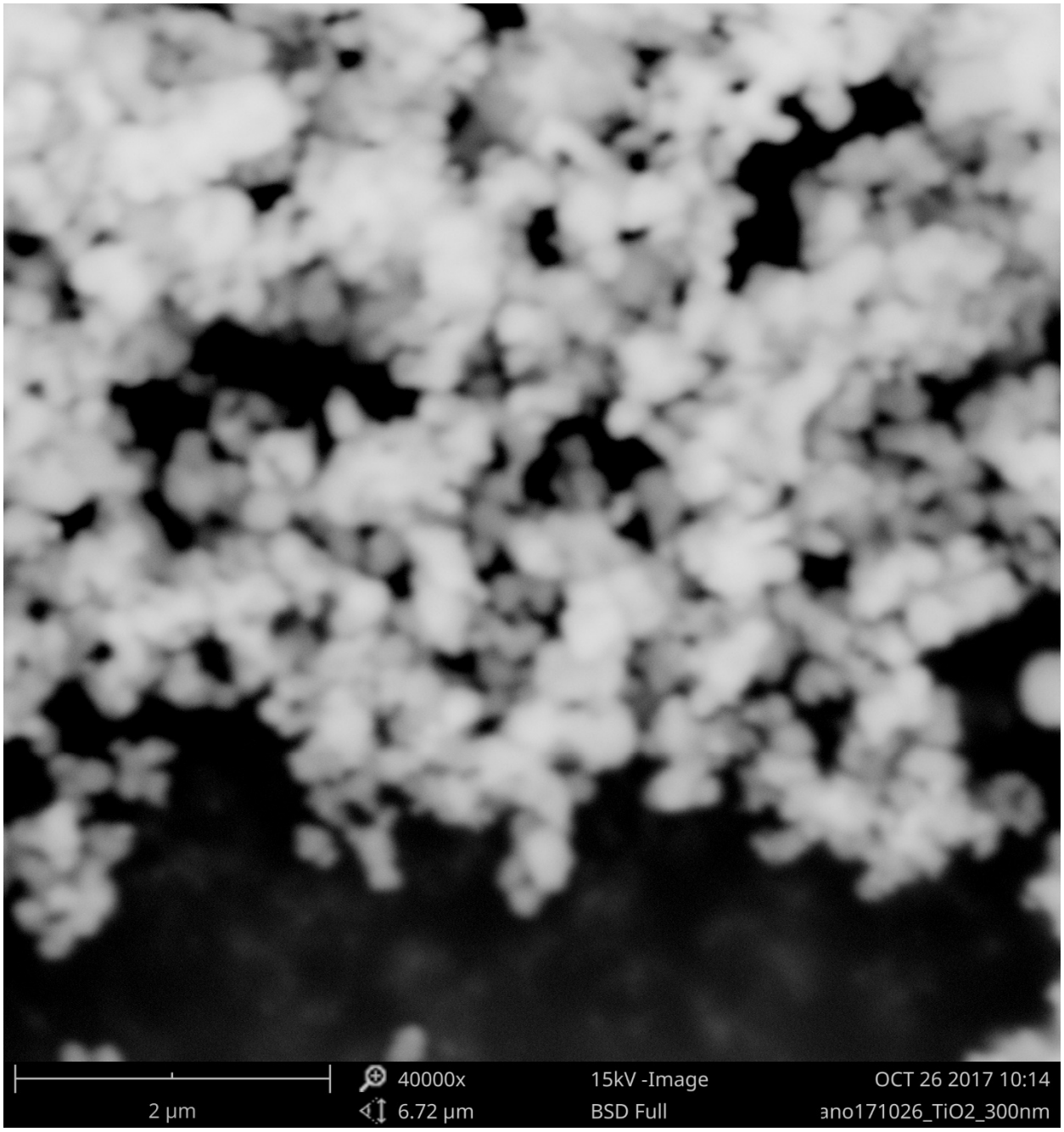

Figure 55. TiO_2 300 nm Bulk Sample SEM High Magnification

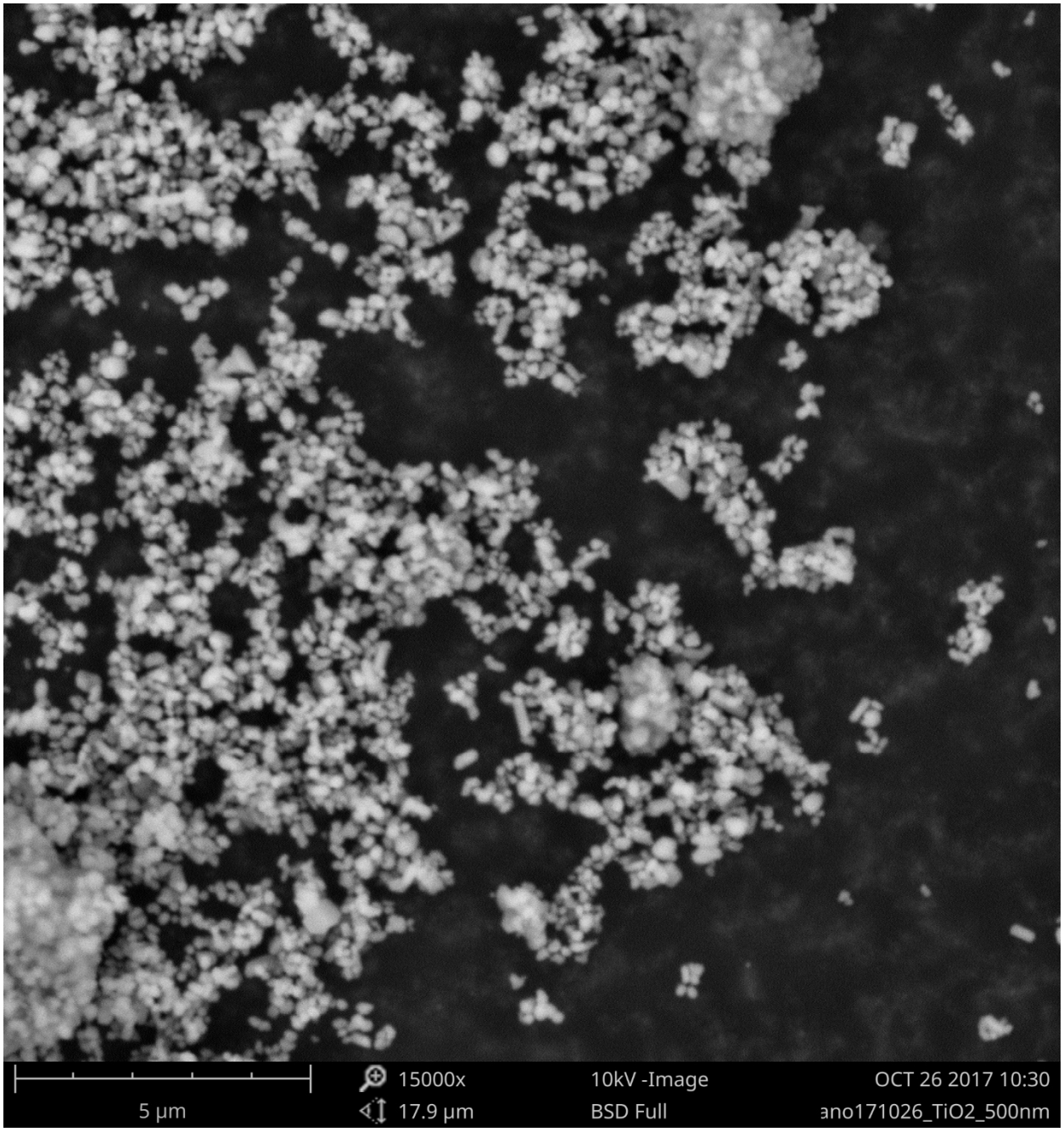

Figure 56. TiO_2 500 nm Bulk Sample SEM Wide View

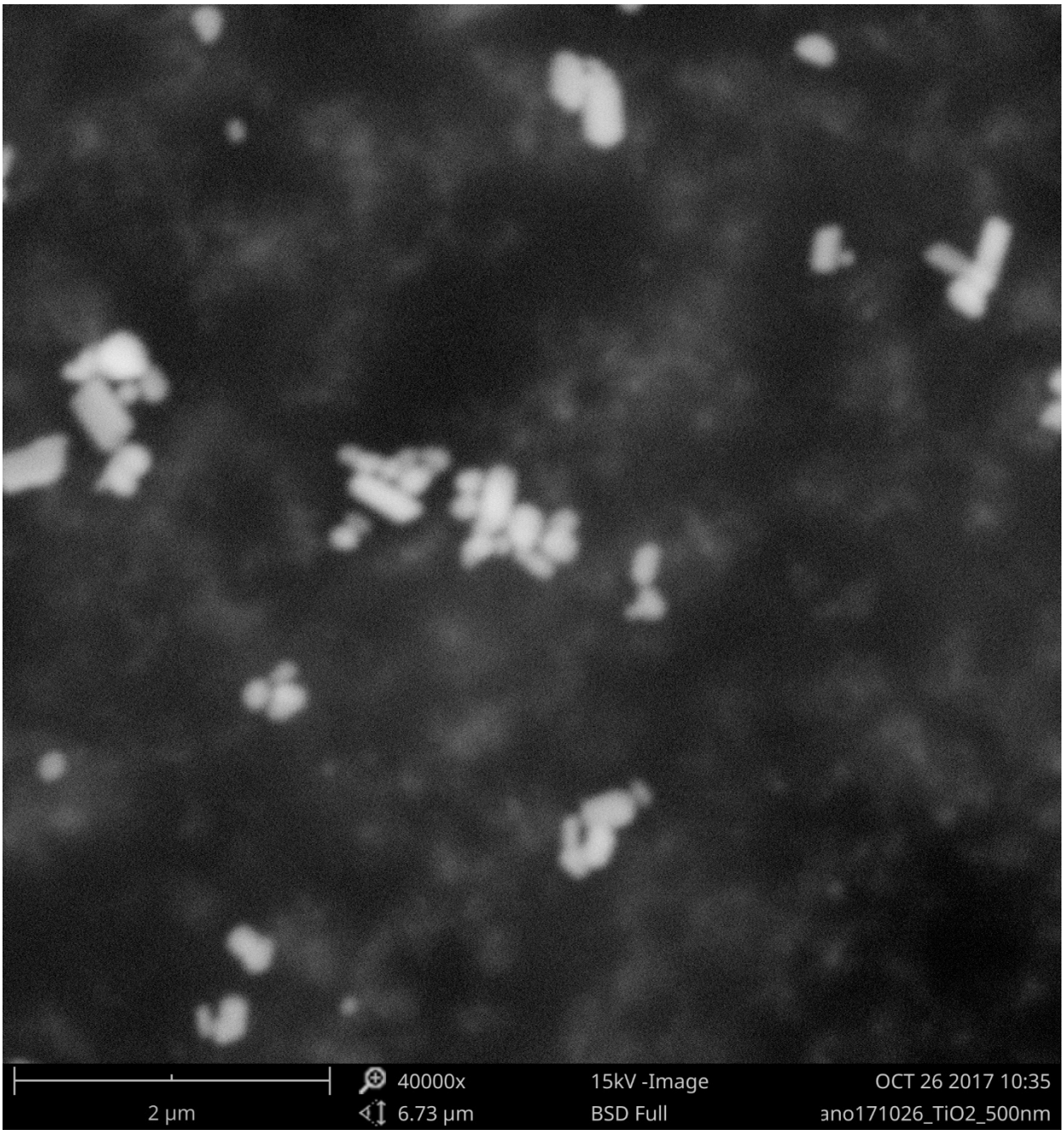

Figure 57. TiO_2 500 nm Bulk Sample SEM High Magnification

To confirm that no substantial agglomerations pass through the seeder, SEM samples are again taken from the nozzle exit with only the seeder running with a variety of sonic orifices. The cyclone cutline model provides an estimation of the desired orifice size in Figure 58, however, this was just a first order approximation and iteration was required to achieve acceptable performance. A 1.50 mm orifice was first used, but the seeding density was far too high, as a steady jet of particles

was observed rather than a faint cloud. This is attributed to the substantial increase in the velocity ratio in the seeder first stage when the particle diameter was decreased while the total volumetric flow rate was simultaneously increased to improve efficiency in the seeder second stage. A 0.84 mm was tested next to balance between a moderate first stage velocity ratio and a still potentially suitable cutline based on Figure 58. The wide view SEM sample in Figure 59 demonstrates qualitatively sufficient seeding density comparable to that observed in the SiO_2 streak testing. Figure 60 confirms that the bodies passed by the seeder are at most an agglomeration of one or two constituent particles and are maintained well under 1 μm.

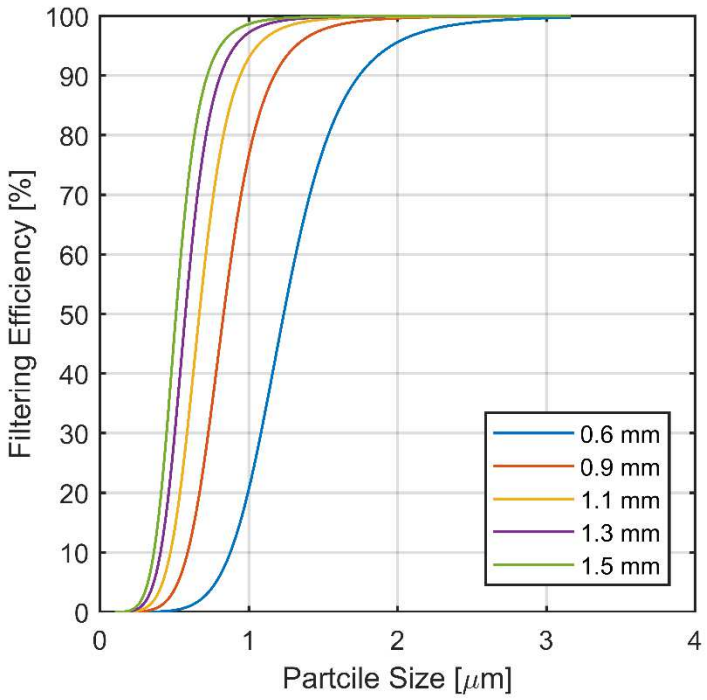

Figure 58. Cyclone Cutline for a Range of Sonic Orifice Diameters Flowing TiO_2 Seed in N_2

Figure 59. TiO_2 Seeder Sample for 0.85 mm Orifice SEM Wide View

Figure 60. TiO_2 Seeder Sample for 0.85 mm Orifice SEM High Magnification

4.2.2 Nitrogen Streak Tests with TiO_2

Eleven tests were conducted using the 100 µs sweep profile of the streak camera of which, nine provide resolvable streak data and two are overexposed after adjusting the streak camera triggering delay relative to the seeder opening. The nominal nozzle stagnation pressure was set at 120 psia and stagnation temperatures remained relatively constant between tests around 291 K. Lower

fluctuations in temperature compared to the first set of PSV tests are due to shorter run times of about five seconds which reduces cooling of the holder and feed lines from the gas expansion.

The seeder is operated at ~400 psia to ensure the flow restricting orifice remained choked regardless of pressure drop through the cyclone separator to the main nozzle flow junction. To improve seeding density over the previous tests, MV-N2-04 between the seeder first and second stages and PV-N2-02 between the regulator panel and the seeder inlet are shut between tests, and the seeder is vented upstream of the sintered disk (which does not allow seed to flow out) from 400 psia to 250 psia via SV-N2-01. PV-N2-02 is then opened with the regulator still set at 400 psia to allow an impulse of high flow into the seeder, which can break loose seed particles that may have clumped together and level out any channeling through the seed stack that may have occurred from uneven flow through the fluidized bed. PV-N2-01 is then opened to initiate the main flow through the nozzle. Once equilibrated, MV-N2-04 is opened to release the seed and then the streak camera is triggered. The appropriate timing to trigger is determined via examination of the v1212 high-speed video, which shows that maximum seed signal is present through the first three seconds of the test. Figure 61 and Figure 62 show representative instrumentation data for these tests. The main chamber pressure rises to approximately 110 psia in half a second, and then the seeder is opened which contributes the final step up to a steady 120 psia. The zero point in the figures represent the camera trigger point at which the streak data is acquired. Some slight oscillations in temperature are observed as the various flow sources are introduced and begin to cool from expansion of the gases, however the range during the measurement itself produces comparable conditions. The seeder response in Figure 62 demonstrates that some noticeable pressure drop through the filter plate is observed. This may contribute to the decline of seeding density after the three second mark as less flow than expected is being passed through the powder bed, however, the stirring technique implemented before testing does aerate enough particles prior to opening MV-N2-04 to seed the measurement volume for the test duration.

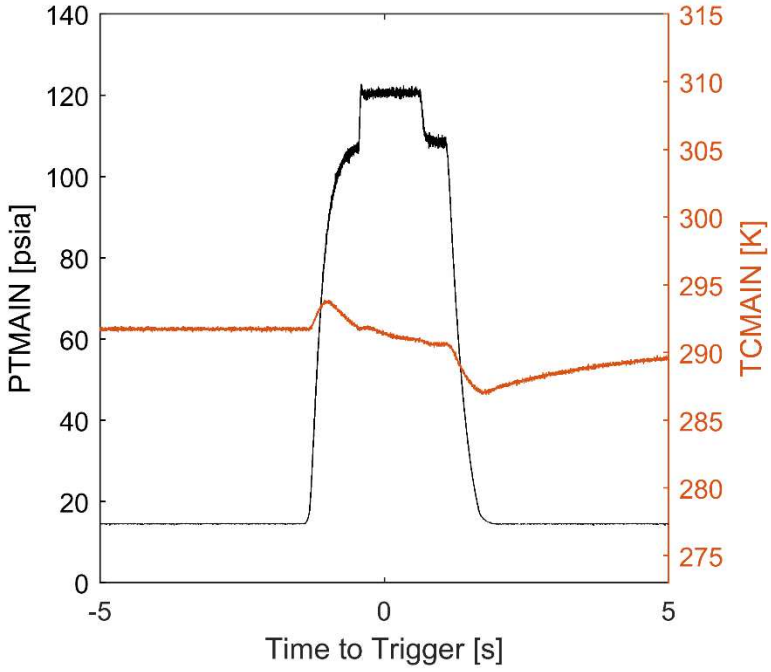

Figure 61. Sample Stagnation Data for TiO_2 in N_2

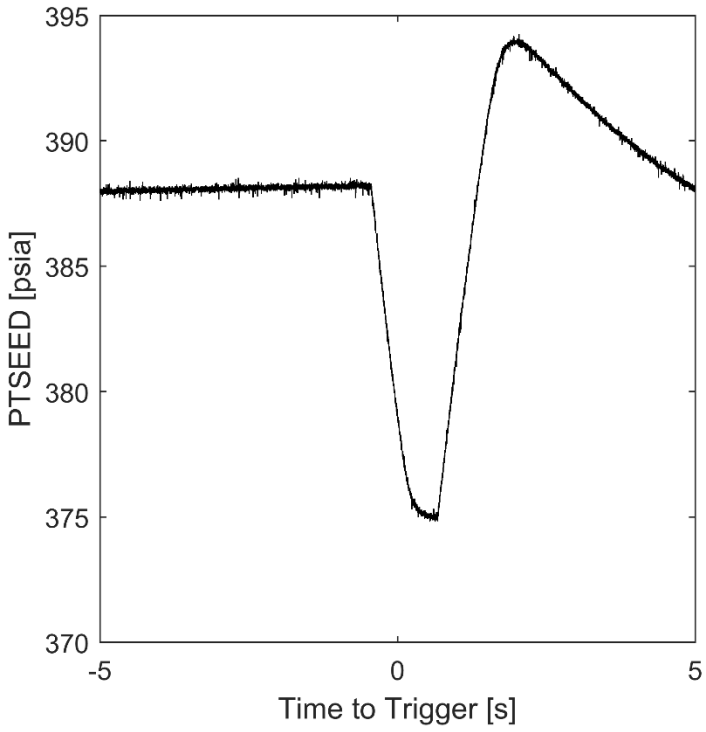

Figure 62. Sample Seeder Response for TiO_2 in N_2

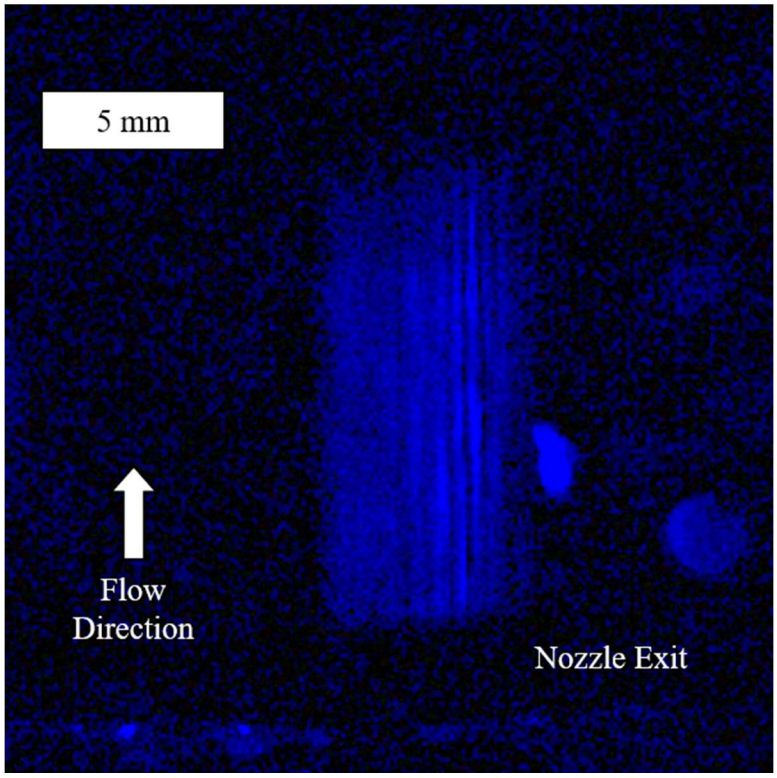

Figure 63. V1212 Video Frame of Nozzle Exhaust
(98 μs Exposure and Maximum Blue Gain)

The streak data analysis procedure is described here with results from test 7 provided as an example. The raw streak output, shown in Figure 64, provides distinguishable lines evenly distributed across the time domain. This ROI represents the entire 1360 pixel time domain and 300 pixels in the spatial domain. The scaling factor y_s calibrated from the Ronchi ruling is 22.1±0.1 μm/pixel, and t_s provided from the Sydor calibration data is 80.0±5.8 ns/pixel. The time axis zero is defined from Sydor as a calibrated delay from the input trigger signal. Because the flow is steady, and this entire exposure corresponds to only one cycle of the other data acquisition systems, this point is not essential, however, for time-varying analyses, this reference point can be used to correlate data. The particles are moving out of the nozzle from the top to the bottom of the image, and each appears to remain in view through the entire 4 mm laser sheet. Given the narrow width of the laser the sheet, this indicates that the particles are moving far faster axially than radially, as expected. The dimmed section at the right edge represents the edge of the photocathode within the streak camera, and the dark limits at the top and bottom in the y-axis are the edge of the laser sheet.

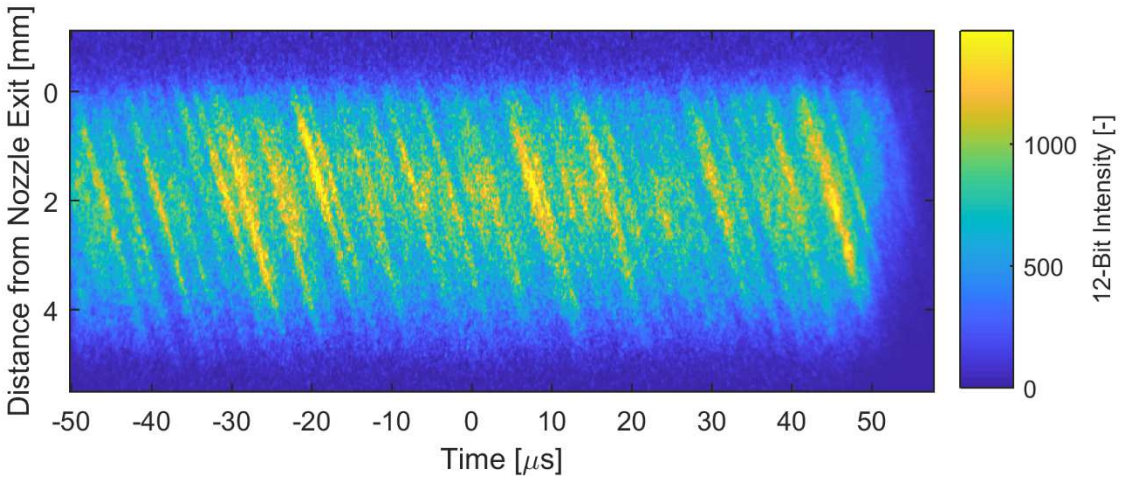

Figure 64. Raw Streak Image for TiO_2 in N_2 Test 7

The first step to calculating the mean velocity is to apply the CSFT and determine a first-order estimation of the average slope of all elements in the image. Figure 65 shows the peaks in each column of the CSFT with a fit line through the central, linear group displayed. The initial slope estimate is 1.87 pix/pix when scaled back to the spatial domain. While this estimate alone is how previous processing of the images was done, the peaks show a slight curving trend toward the higher frequencies. Rather than guessing which range of low-pass frequencies properly reflect the primary streak slopes or at which point the fit line deviates "too much" as they curve outward, this new process of preserving a wide band of slopes at all frequencies and continuing the processing in the spatial domain is implemented. The hyperbolic filter sets the asymptotic bounds such that it retains slopes ranging from 1.78 to 1.97, and the new CSFT is shown in Figure 66. The high magnitude points with which the filter was oriented are shown centered between the asymptotes, as expected.

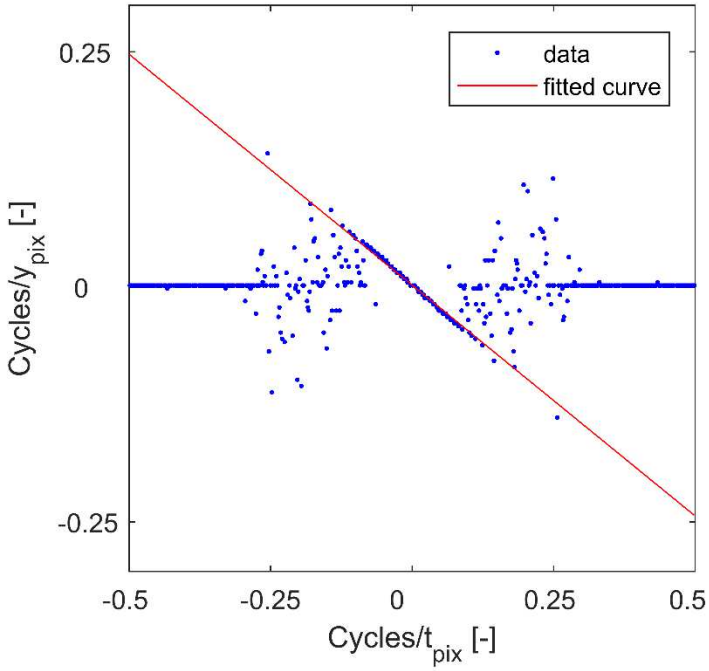

Figure 65. Initial CSFT Peak fit for TiO_2 in N_2 Test 7

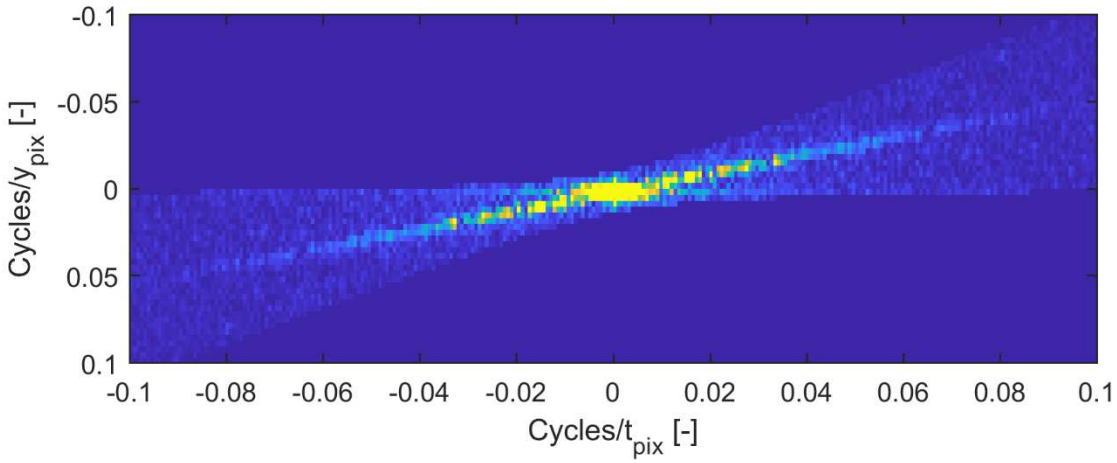

Figure 66. Filtered CSFT for TiO_2 in N_2 Test 7

Applying the inverse CSFT to the filtered data and implementing a baseline correction to each sample in time produces Figure 67. The baseline adjustment is performed to account for the slight roll-off that is visible along the y-axis so that a constant minimum peak height can be defined for the detection algorithm. The variation is very likely due to uneven intensity from the laser with the

center being brightest and the edges slightly dimmer. The image is then resampled in both dimensions to ten times the original resolution. This allows the peak detection function to extrapolate the true peak location between pixels rather than forcing to one pixel extent or the other of the peak. Because the slopes are greater than one, the peak detection algorithm is applied within each row rather than along the columns. A separation distance is defined to eliminate sampling of double peaks on the same streak image.

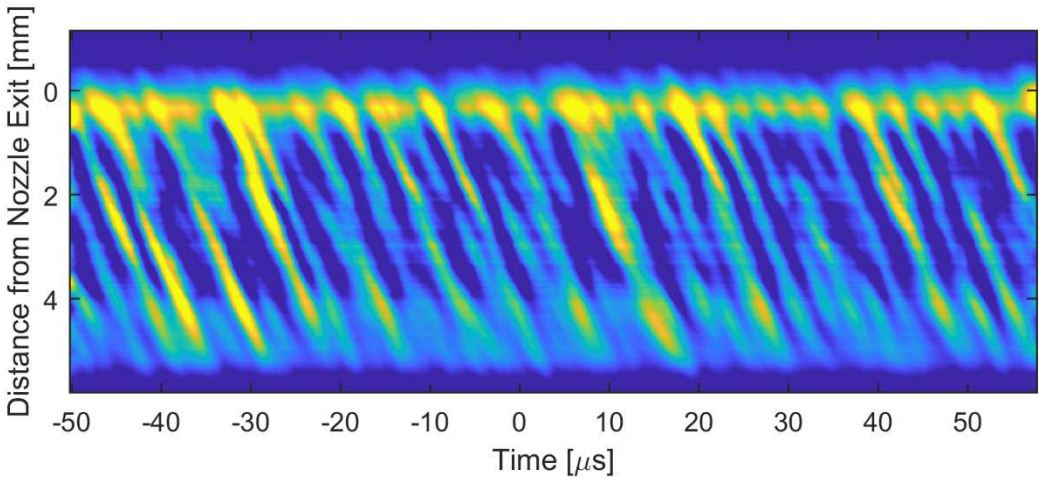

Figure 67. Inverse CSFT for TiO_2 in N_2 Test 7

The identified peaks within each row are overlain onto the original streak image in Figure 68. The red bands represent the central 70% of the time domain sampled. The time calibration for the streak camera is only provided for the center 90% pixels, and away from the center row on the CCD the photocathode geometric correction is limited at the edges, as well. Several outliers are visible in the top rows before the exit of the nozzle, which are a product of the window size used for background adjustments. The mean value is taken only from the row corresponding to the nozzle exit downward. The better spaced peaks around -20 μs, for example, show a smooth slope across the entire domain. Other regions, such as at 10 μs, indicate the identified peak location traversing across the overall streak. This may be an effect of the streak camera's ability to resolve multiple particles very near each other. Despite the peak separation limits defined, if two signals merge into one broad peak the detected maxima could shift across the two particles due to sensor noise or variations in illumination intensity. An outlier detection mechanism on an entire streak body level may be an adequate remedy in the future, though one was not yet developed for this dataset.

Alternatively, the effect may be due limits in observing the particles rather than analysis of the image. Variations in the local refractive index of the plume may be strong enough to cause transient oscillations in the scattered signal. A proposed method to quantify this in the future might be to repeat the spatial scaling tests using the Ronchi ruling placed behind the nozzle with nitrogen running through the nozzle. A frequency analysis of perturbations in the calibration lines could better define the magnitude to which inherent streak non-linearities should be expected.

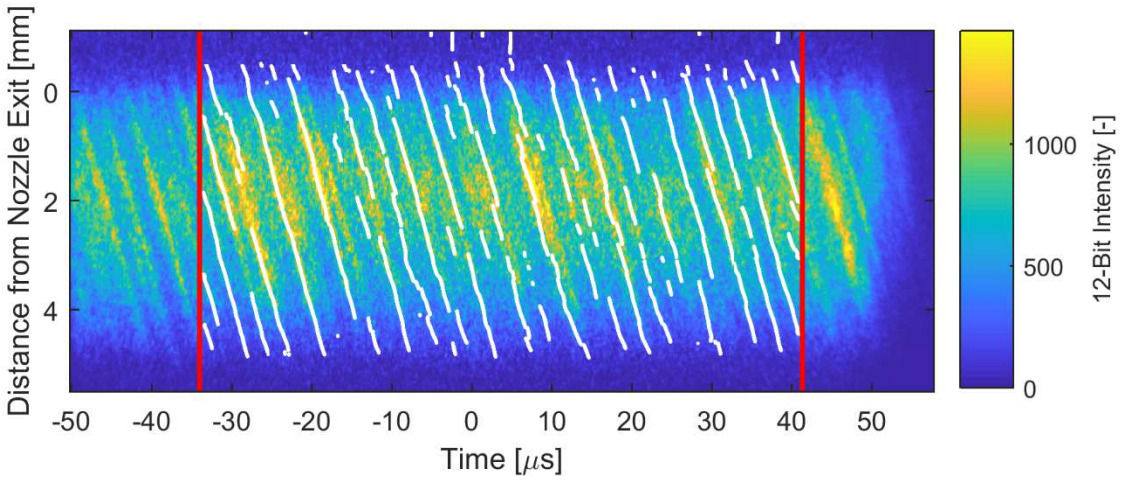

Figure 68. Peak Locations Identified for TiO_2 in N_2 Test 7

To convert peak locations to slopes, each pair of successive rows is compared to identify potentially neighboring peaks within a single streak and the displacement between them. If a translation in time is determined to be below the connectivity threshold that describes successive points in the same peak, then that shift is recorded. For these tests, with mean slope of near two, that connectivity threshold is 0.1 pixels (due to the 10x resampling) as virtually all rows would be expected to show either zero or one count displacement. Negative displacements are ignored. To achieve the mean plume velocity at the center line, all detected displacements are averaged from the nozzle exit through the y-domain and scaled by y_s, t_s, and the resampling factor in y of 10. Average particle velocities across the entire sample domain for each test are reported in Table 8. The average slope for test 7 is calculated to be 1.848 which is near the original estimation of 1.87 from the initial CSFT though processing within the spatial domain provides a more certain value along with location specific data.

The expected flow velocities against which the observed particle velocities are compared are calculated from stagnation temperature measurements from the given test and the Mach number obtained from schlieren test 19 in Section 4.1.6. This reference was selected rather than the nozzle exit because the schlieren measurement was obtained several millimeters downstream of the nozzle, which corresponds to the mean position around which the streak samples are taken rather than the front edge. The consistency of this basepoint in each row of the results table reflects more so that the temperatures remained relatively constant than that the flow fields were exactly alike since the Mach number is taken from a single prior test.

The uncertainty in flow velocity (ε_f) is primarily driven by the slope fit performed on the average schlieren CSFT peaks. The particle velocity uncertainty (ε_p) is influenced most strongly by the standard error of peak-to-peak displacements samples. As a continued example, test 7 used 26,000 peak shifts to calculate the mean displacement and the standard error was found to be 0.6% of the mean.

Table 8. Summary of TiO_2 Streak Data for Nitrogen Flow

Test Number	T_0 [K]	v_p [m/s]	(ε_p)	v_f [m/s]	(ε_f)	ϕ [-]	(ε_ϕ)
1	292	509	(3)	490	(13)	1.04	(0.03)
2	292	498	(3)	490	(13)	1.02	(0.03)
3	291	499	(4)	490	(13)	1.02	(0.03)
4	291	507	(5)	490	(13)	1.04	(0.03)
5	292	499	(5)	490	(13)	1.02	(0.03)
6	291	499	(4)	490	(13)	1.02	(0.03)
7	291	509	(4)	490	(13)	1.04	(0.03)
8	291	510	(3)	490	(13)	1.04	(0.03)
9	291	507	(4)	490	(13)	1.03	(0.03)

Across all nine tests, the mean particle velocity calculated exceeded the expected flow velocity ranging from 498 to 510 m/s with uncertainty of approximately ±4 m/s. However, the uncertainty in the schlieren measurements brings the uncertainty band for ϕ nearly in range of the expected value of 0.99. While it is impossible for the particles to exceed the true flow velocity. It is a marked

improvement over the SiO_2 results demonstrating lag greater than 15% in most cases. At minimum, the conclusion can be drawn that 300 nm TiO_2 particles very likely do suitably follow the flow in the given test article, whereas 1 µm SiO_2 particles did not. Deviations between the measured and expected velocities instead represent limitations in testing the system almost a year apart from the schlieren baseline to these streak tests or limitations of the two velocimetry techniques themselves in their current state, which could be further refined with iteration in both application of the diagnostic and processing of the acquired data.

Despite the stirring method implemented by venting the seeder and rapidly repressurizing, tests 4 and 5 each showed a noticeable drop in seeding density as demonstrated by Figure 69. Previous tests 1, 2, and 3 resemble the results shown for test 7. To further break up clusters within the seeder first stage, the system was disassembled and physically shaken end over end several times. This was effective in breaking loose more seed on the surface to entrain in the flow. Two attempts recorded between test 5 and test 6 saturated the streak camera with signal, as Figure 70 shows. Only after extending the trigger delay relative to the seeder opening was a more suitable seed distribution re-achieved and successful testing resumed with test 6.

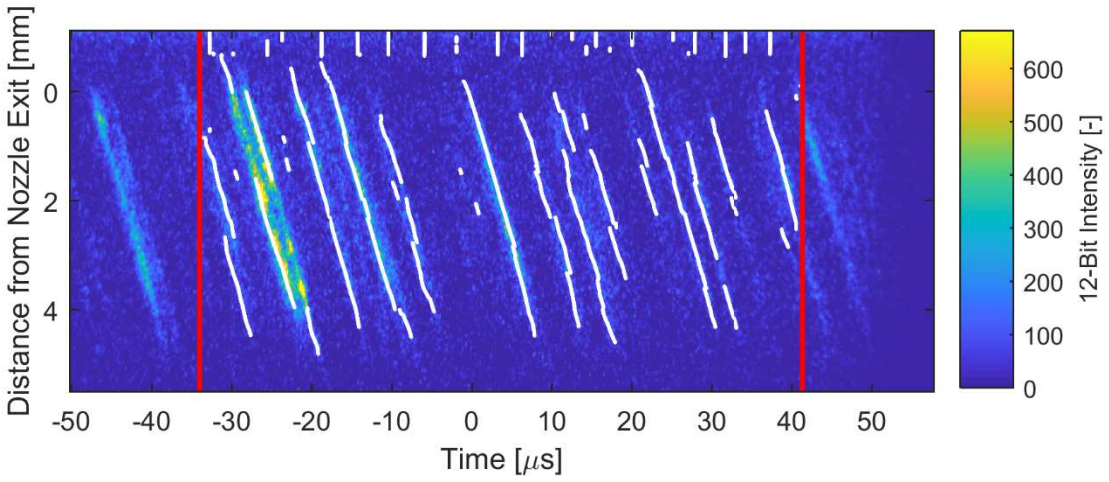

Figure 69. Peak Locations Identified for TiO_2 in N_2 Test 4

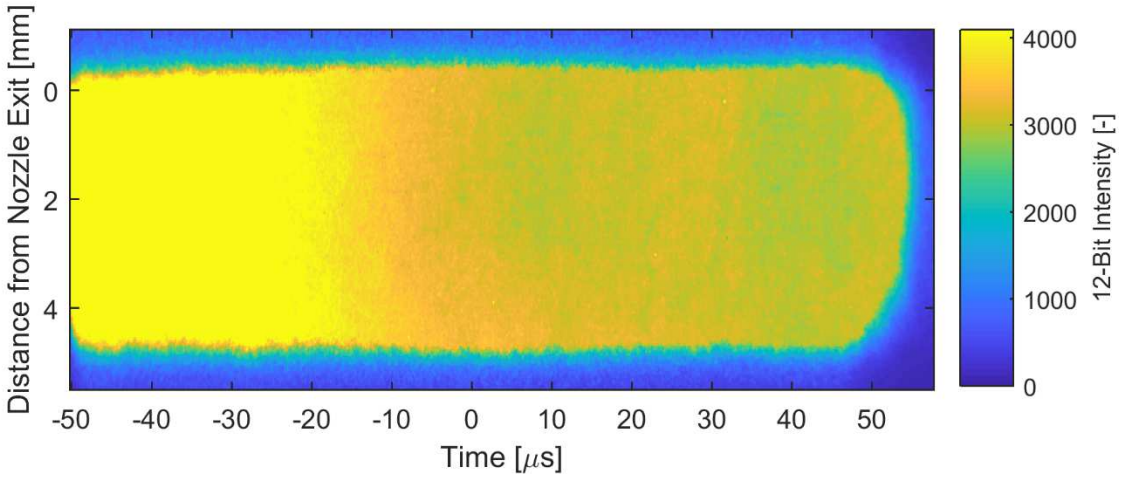

Figure 70. Saturated Streak Signal for TiO_2 in N_2

Comparing the results shown in this section using TiO_2 to the prior experiments performed with SiO_2 demonstrates the substantial improvement in image quality. Figure 71 shows a sample from SiO_2 test 15 representative of those taken with the previous measurement configuration. The peak signal is over an order of magnitude lower than the current data set, and the particle paths are not contiguous due to the sensor noise. The progress in producing strong, sharper signal is attributed to the added alignment mechanisms and procedures to center the nozzle exit, camera field of view, and illumination sheet. Replacing the dove prism with the two-mirror periscope also likely improved signal and focus as the prism is known to introduce some astigmatism and provides lower transmission than the mirror's reflectance. Even prior to the improvement, faint, diagonal streak trends are still visible, so the extended image analysis procedure was applied to this image to review the previous conclusions made about the SiO_2 particle response and agreement to schlieren. Despite the substantial noise, the procedure is still able to identify the faint streaks, as Figure 72 shows. Calculating the mean velocity from these few samples yields a value of 411 m/s±9 m/s. This is somewhat higher than the previous analysis result of 387±13 and suggests the SiO_2 lag may not have been as drastic as first thought, however it still reinforces that the replacement with 300 nm TiO_2 provides the necessary improvement required to proceed to faster flows.

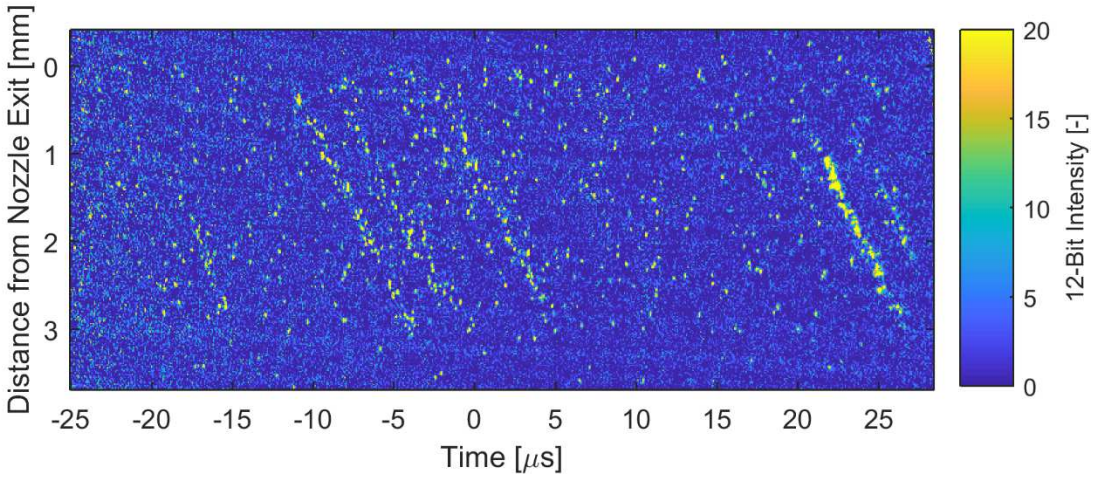

Figure 71. Raw Streak Image for SiO_2 in N_2 Test 15

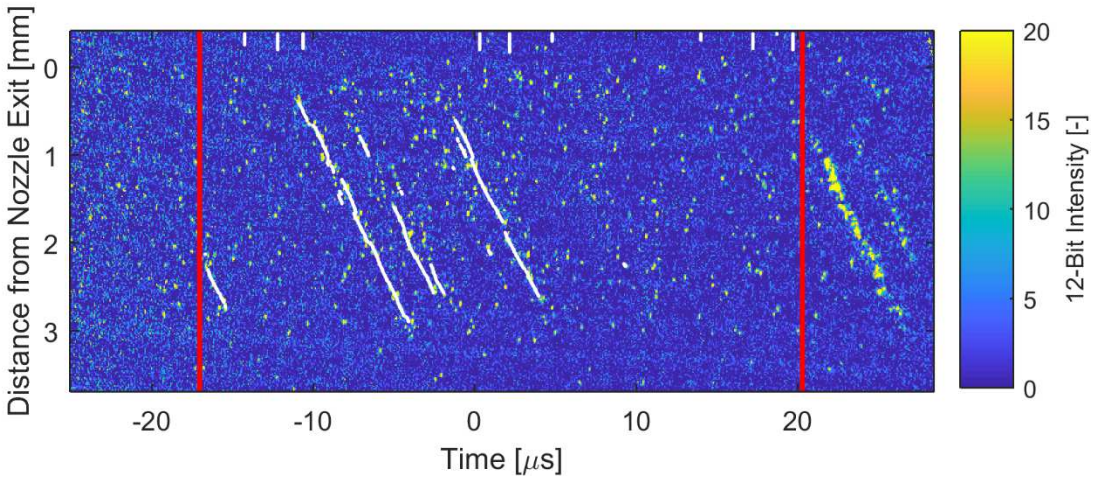

Figure 72. Peak Locations Identified for SiO_2 in N_2 Test 15

4.2.3 Helium Streak Tests with TiO_2

Despite the slight deviation between the two velocimetry techniques, the satisfactory seed response did allow progression on to higher velocity flows. In order to expand the bounds within which PSV can be applied, the bulk nozzle flow of nitrogen was replaced with helium which has a much higher speed of sound. The seeder was still driven with nitrogen to preserve the well-understood operation based on flow rates and viscosities. The expected velocities for the gas mixture flowing through the nozzle are calculated from isentropic flow assumptions, estimated mass flow data of the pure nitrogen through the choked seeder orifice for each test, and the stagnation state data recorded in the nozzle for each test. Nozzle pressure measured ~118 psi and the temperature was

near 293 K across all tests. The seeder operated at around 500 psi for most tests. Seven tests were performed using the 50 µs sweep speed, though as with the nitrogen tests described in the previous section, several tests displayed a sequential reduction in seeding density and two were excluded from reporting for lack of signal. Removing and manually shaking the seeder again provided the necessary agitation to release more seed. The scaling factor y_s is 23.1±0.2 µm/pixel, and t_s provided from the Sydor calibration data is 39.6±2.5 ns/pixel.

Despite the reduced pixel dwell time in both axes due to the faster sweep in time and the faster travel through the y-domain, the successful tests showed adequate scatter for clear detection with the streak camera. Figure 73 and Figure 74 demonstrate a low seeding density test prior to resettling the seeder and a high seeding density test following the procedure described above. The sample from test 2 still produced one substantially resolvable streak around 10 µs, which allowed inclusion in the data set, though the uncertainty is much higher due to having fewer samples. Conversely, test 3, 4, and 5 appear much the same to the better performing samples of the previous configuration. Multiple streaks are seen across the time domain reaching from the nozzle exit to the laser sheet edge. As the v_f approximately doubled and t_s halved, the filtering and peak detection process was very similar to that from the nitrogen tests with slopes in the range of 1.9.

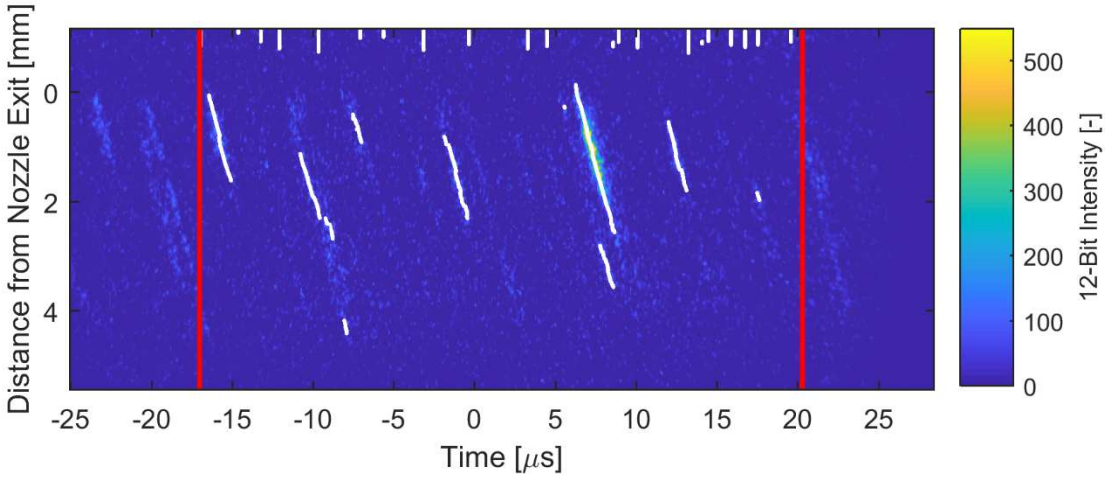

Figure 73. Peak Locations Identified for TiO_2 in He Test 2

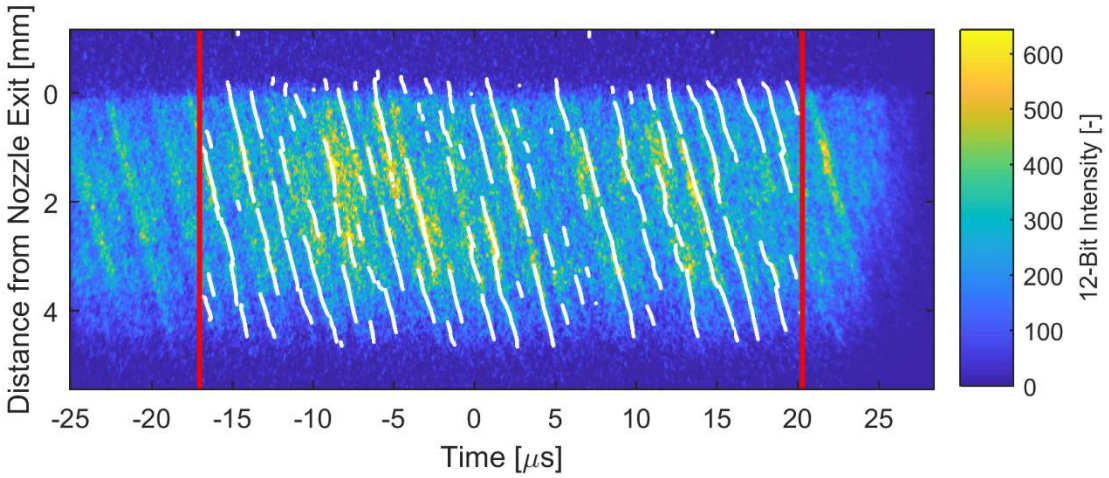

Figure 74. Peak Locations Identified for TiO_2 in He Test 4

The mean velocities across the entire measurement domain are recorded in Table 9. Particle velocities ranged from 1128 to 1171 m/s with uncertainties on the order of 15 m/s except for test 2 with its drastically reduced number of identified peaks. The predicted flow velocities remain consistent around 1122 m/s for tests 1-4 as the seeder and nozzle pressures and temperatures were fairly consistent. The model for test 5 rises to 1144 m/s because the seeder pressured was lowered slightly from 500 psi in the previous four tests to 440 psi. However, the particle velocity measurement does appear to reflect that velocity increase.

Table 9. Summary of TiO_2 Streak Data for Helium Flow

Test Number	T_0 [K]	v_p [m/s]	(ε_p)	v_f [m/s]	ϕ [-]	(ε_ϕ)
1	293	1115	(16)	1120	1.00	(0.01)
2	293	1132	(30)	1124	1.01	(0.03)
3	293	1171	(12)	1122	1.04	(0.01)
4	293	1128	(13)	1123	1.00	(0.01)
5	293	1147	(14)	1144	1.00	(0.01)

As before, with tests flowing nitrogen, the particle velocity very nearly equal to the flow with ϕ ranging from 1.00 to 1.04. While the results here show fewer instances of the particle velocity exceeding the flow velocity, the predicted values do not account for inefficiencies in the nozzle that were found to be present in the nitrogen tests as no schlieren data was taken for comparison.

This was in part because the upgraded PSV collection optics did not allow setup of the schlieren system simultaneously, and any measured Mach number would be heavily reliant on estimated gas properties from the pressure and temperature data due to it being a mixture. However, as stated before, the promising match of measured velocities supports the conclusion that the 300 nm TiO_2 is adequate and that the PSV can very clearly provide flow velocity measurements exceeding 1000 m/s. The remainder is a matter of limiting uncertainty and refining the means by which the exact values can be validated.

4.3 Spatially Resolved Analysis

As a further investigation into the slightly higher than expected particle velocities, an analysis of the velocity profile varying in *y* was performed. This analysis also provides substantial benefit for future applications of PSV to flow fields that are varying in time or space. After determining all peak shifts, the samples are binned in 500 row increments of the 10x resampled data, which corresponds to approximately 1.1 mm intervals across the entire analyzed time domain. This binned window was then stepped at 10 sample intervals and all peak displacements within the bin were averaged. Figure 75 shows the results for test 9 when the binned averages are scaled from pixel slopes to m/s. The *y* location (displayed on the x-axis) represents the center of the bin, and thus the first available point is 250 rows beyond the nozzle exit. The flow appears to show the more expected velocity around 485 m/s for the bin closest to the exit and then a rapid acceleration occurs up to 515 m/s which then steadily rises to ~530 m/s by the end of the measurement region. This acceleration exiting the nozzle could explain the slightly elevated bias of the tabulated mean measurements. Based on the design nozzle profile and the measured stagnation pressure, the flow is slightly underexpanded, and some acceleration is to be expected. This is also supported by the acquired schlieren measurements discussed above, though the acceleration did appear not to be quite of this magnitude in those tests.

Even binning 1.1 mm worth of samples, the signal is still quite noisy, and smaller bins show oscillations of 100 m/s or more. The relatively binary nature of the peak displacement from other a shift of zero pixels, one pixel, or no acceptable shift requires a significant number of samples to set an appropriate mean. Other tests analyzed showed similar profiles though this one was found to be the smoothest. Performing peak shift measurements across more than just neighboring rows

would reduce the binary nature and warrants further investigation. This serves as a baseline on which the analysis can continue to be built.

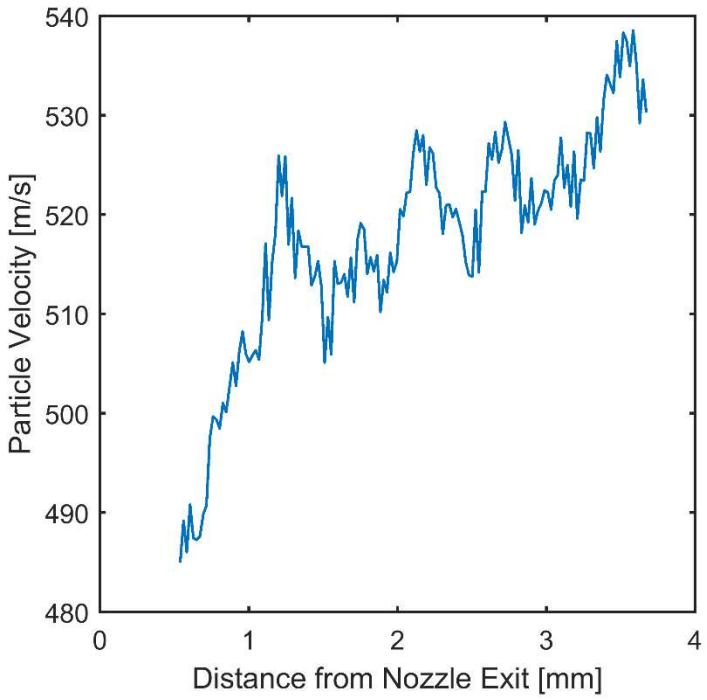

Figure 75. Spatially Resolved Mean Particle Velocity Data for TiO_2 in N_2 Test 9

5. CONCLUSIONS

In this work, development and testing of a new velocimetry technique was described. Particle Streak Velocimetry has the potential to provide higher sampling frequency than traditional PIV. This can aid in visualizing highly transient events and provide a much lower limit to resolvable lengths scales in very high-speed flows. Observations and lessons both from the measurement data and operational requirements can feed the start of another iteration to further expand the envelope of flows to which PSV can be applied. The work resulted in a US Provisional Patent filed 05/19/16.

5.1 Seed Particle Delivery

A variety of seed materials and sizes were surveyed and characterized by shape, distribution, scattering ability, and modeled flow acceleration response. A two-stage filter using nitrogen as a carrier gas was designed, built, and tested to produce consistent particle sizes required for accurate fluid velocity measurement. SEM samples collected from the seeder outlet show acceptable blocking or break up of aggregate particles. Further development could be performed to operate the seeder at steady state rather than the stirring and blow down procedure described above. Titanium Dioxide powder with mean diameter of 300 nm was found to be meet the necessary criteria to perform the PSV experiment in the cold gas thruster described.

5.2 Particle Illumination

The angular dependence of scatter for candidate particles was modeled and implemented to take advantage of the extra degree of freedom afforded by a 1-D measurement. It was shown that particle and wavelength scales used here produce a strong forward scattering bias. Two illumination sources were sized and built to provide sufficient scatter for detection by the measurement system. The 450 nm laser diode provides collimated, coherent light that is easy to steer to the measurement region and can run near continuously. However, the maximum power of ~4.5 W instigated the second concept which uses a xenon flashlamp to produce high peak energies of 45 kW for a 50 μs peak exposure. An elliptical reflector was manufactured to maximize delivery of the output optical energy to measurement volume. The first source proved sufficient to provide

detectable particle scatter for the given experiment. Further handling of the projected image of the second system will be required to maintain a narrow measurement region.

5.3 Characterization of the Measurement System

The optical system was tuned over time to provide control over each necessary component until a consistent, high signal could be produced from particles in the flow. The system resolution, magnification, and alignment were analyzed using a Ronchi ruling and narrow pin positioned within the measurement volume. Sweep speeds were correlated to the observed spatial scale to determine the speed required to resolve diagonal streaks given the anticipated flow velocity.

5.4 Developmental Tests of Particle Streak Velocimetry

The first attempts at seeding this supersonic flow failed to produce proper particle response, though the measurement system was in fact able to track this slower velocity well. Redoubled efforts to improve seed and seeder performance then allowed PSV to be benchmarked against a predictable flow under known conditions. Results were comparable to the predictions and known measurements for nitrogen flowing through the nozzle on the order of 500 m/s. The progression to a mixture of helium and nitrogen raised the velocity to over 1100 m/s which was again resolved by the PSV technique.

Each testing phase helped to clarify what quality data samples look like for this system. The first images were barely distinguishable from the sensor noise and were not contiguous. Though the streak images acquired show sufficient focus and sharpness to distinguish particles, this can still be improved. The oblique measurement region formed by the intersection of the laser sheet and field of view produces noise from particles beyond the depth of field. A finer balance could be struck between collecting the forward-biased Mie scatter and forming a narrower intersection between the planes. A higher-powered illumination source could compensate for the portion of forward scatter lost. Alternatively, increasing seeding density of the flow and narrowing the slit window would produce an equivalent number of samples detected overall but with more falling inside the depth of field rather than contributing noise. Finally, the streak camera itself produces more noise than traditional devices. Investigation of sensor binning within the hardware, tuning of

the streak tube gains to sacrifice precision in one of the axes over the other, or adjustment of the MCP operation are all potential options that could be adjusted for a specific application.

The ability to process data in the spatial/temporal domain well enough to produce a satisfactory mean is a first step towards unlocking the real potential of this diagnostic. While more refined velocity distributions along either axis cannot yet be readily produced without substantial noise, the ingredients are available. With equal iteration applied to developing the processing architecture, high resolution time and spatial distributions of the velocity field can be produced. Current tests performed at 12.5 MHz and 25 MHz already exceed limits identified for PIV if that data can be successfully extracted. Spatially, at both the 500 m/s and 1100 m/s flow conditions, individual particle paths were recorded continuously across a domain of 4 mm which spanned 200 pixels. The measurement domain can be expanded beyond those 200 pixels to utilize the entire resolvable area of the sensor with the appropriate light source and sheet forming optics.

These sequential results serve to set a baseline against which even faster flow measurements could be built. Within the tunable sweep duration range of the streak camera, resolvable velocities through the given measurement region scale linearly. For example, with twenty times the illumination power, the 4 ns/pixel sweep setting could resolve a flow velocity of 10 km/s to identical resolution of the 500 m/s flow shown above. The limiting factors for this system's efficacy become the particle seeding frequency and their response to the accelerations and flow features of interest. Beyond a certain limit, the laser/camera system in PIV or PSV cannot expand upon the fundamental response of the seed particles themselves. The 300 nm TiO_2 in Nitrogen yields a Stokes characteristic time on the order of 1 μs which would govern the turbulent features that could be resolved. For this reason it would be greatly beneficial to explore molecular tagging options to produce the visibly tracked objects. If the extinction time for the emission of a deliberately excited molecule within the flow can sustain through its residence within the sample region, far greater particle response can be achieved before the limits of PSV are reached.

APPENDIX A. MATLAB SCRIPTS

MieScattering.m

```
in = input('[D y nl]: ');

%%%%%%%%%%%%%%%%%%%%%%%%%%%%%%%%%%%%%%%%%%%%%%%%%%%%%%%%%%%%%%%%%%%%%%%%%%%%%%%
% Equations derived from C. F. Bohren and D. R. Huffman, "Chapter 4:
% Absorption and Scattering by a Sphere," in Absorption and Scattering of
% Light by Small Particles, Wiley, 2007, pp. 83-129.
%%%%%%%%%%%%%%%%%%%%%%%%%%%%%%%%%%%%%%%%%%%%%%%%%%%%%%%%%%%%%%%%%%%%%%%%%%%%%%%

D  = in(1); % Diameter                       [nm]
y  = in(2); % Wavelength                     [nm]
nl = in(3); % Refractive index of particle  [-]
l  = 36000; % Define length of scattering angle vector
s  = 16;    % Set number of terms in series to keep
th = linspace(-180,180,l+1);    % Generate scattering angle vector

n  = 1;         % Refractive index of medium
m  = nl/n;      % Relative refractive index
x  = pi*D*n/y;  % Size parameter

% Define Ricatti-Bessel functions and their derivatives
ps  = @(nu,z) sqrt(pi*z/2).*besselj(nu+1/2,z);
xi  = @(nu,z) sqrt(pi*z/2).*besselh(nu+1/2,z);
psp = @(nu,z) ps(nu-1,z)-nu.*ps(nu,z)./z;
xip = @(nu,z) (1/2)*(xi(nu-1,z)-xi(nu+1,z)+xi(nu,z)./z);

% Initialize series variables
a  = zeros(1,s);
b  = zeros(1,s);
p  = zeros(s,l+1);
t  = zeros(s,l+1);
Es = zeros(1,l+1);
Ep = zeros(1,l+1);

% Solve for scattering coefficients
for i = 1:s
    a(i)  = (m*ps(i,m*x)*psp(i,x)-  ps(i,x)*psp(i,m*x))/...
        (m*ps(i,m*x)*xip(i,x)-  xi(i,x)*psp(i,m*x));
    b(i)  = (  ps(i,m*x)*psp(i,x)-m*ps(i,x)*psp(i,m*x))/...
        (  ps(i,m*x)*xip(i,x)-m*xi(i,x)*psp(i,m*x));
end

% Calculate series at each scattering angle
for j = 1:length(th)
    i = 1;    % First term for pi_k and tau_k
    p(i,j)  = 1;
    t(i,j)  = cosd(th(j));
    Es(j) = (2+1/i)/(1+i)*(a(i)*p(i,j)+b(i)*t(i,j));
    Ep(j) = (2+1/i)/(1+i)*(a(i)*t(i,j)+b(i)*p(i,j));
```

```
    i = 2;    % Second term for pi_k and tau_k
    p(i,j)  = 3*cosd(th(j));
    t(i,j)  = i*cosd(th(j))*p(i,j)  -  (i+1)*p(i-1,j);
    Es(j) = Es(j)+(2+1/i)/(1+i)*(a(i)*p(i,j)+b(i)*t(i,j));
    Ep(j) = Ep(j)+(2+1/i)/(1+i)*(a(i)*t(i,j)+b(i)*p(i,j));

    for i = 3:s   % k>2 terms for pi_k and tau_k
        p(i,j)  = (2*i-1)/(i-1)*cosd(th(j))*p(i-1,j)-i/(i-1)*p(i-2,j);
        t(i,j)  =             i*cosd(th(j))*p(i,j)  -  (i+1)*p(i-1,j);
        Es(j) = Es(j)+(2+1/i)/(1+i)*(a(i)*p(i,j)+b(i)*t(i,j));
        Ep(j) = Ep(j)+(2+1/i)/(1+i)*(a(i)*t(i,j)+b(i)*p(i,j));
    end
end

Is = abs(Es).^2;    % Perpendicular polarized scatter intensity
Ip = abs(Ep).^2;    % Parallel polarized scatter intensity

figure();plot(th,Es/max(Es),th,Ip/max(Ip));

Isl = log10(Is./max(Is)*1000);  % Log-scale of normalized scatter to show 3
Ipl = log10(Ip./max(Ip)*1000);  % orders of magnitude
ths = pi/180*th(Isl>=0);        % Convert degrees to rad
thp = pi/180*th(Ipl>=0);
Isl = Isl(Isl>=0);              % Normalized values less than 1/1000 are
Ipl = Ipl(Ipl>=0);              % ignored to clean up polar plot
figure();polarplot(thp,Ipl,'k',ths,Isl,'r','LineWidth',1.1);
hl=legend('Parallel','Perpendicular');
set(hl,'FontSize',9);
set(gca,'FontSize',10,'RTickLabel',{'','.01','.1','1'},...
'RAxisLocation',352);
set(gcf,'Units','Inches','PaperPosition',[0 0 3.5 3.5]);
```

N2HeMix.m

```
T0  = 290;            % Nozzle Stagnation Temp  [K]
Ts  = 291.0;          % Seeder Stagnation Temp  [K]
P0  = 120*6895;       % Nozzle Stagnation Pres [Pa]
Ps  = 438.7*6895;     % Seeder Stagnation Pres [Pa]
Dt  = 0.183*0.0254;   % Nozzle  Throat Diameter [m]
De  = 0.222*0.0254;   % Nozzle   Exit  Diameter [m]
Ds  = 0.033*0.0254;   % Seeder Orifice Diameter [m]

Ru =  8314;        % Universal Gas Constant      [J/kmol-K]
W1 =     4;        % Gas 1 (He) Molecular Weight    [g/mol]
R1 = Ru/W1;        % Gas 1 Specific Constant       [J/kg-K]
c1 =  5190;        % Gas 1 Specific Heat, cp       [J/kg-K]
S1 = 0.138;        % Gas 1 Specific Gravity            [-]
W2 =    28;        % Gas 2 (N2) Molecular Weight    [g/mol]
R2 = Ru/W2;        % Gas 2 Specific Constant       [J/kg-K]
c2 =  1040;        % Gas 2 Specific heat, cp       [J/kg-K]
S2 =  0.97;        % Gas 2 Specific Gravity            [-]

Gi = linspace(0,1,1001);          % Gas 1 Mass Fraction             [-]
Gi([1,end]) = [];
Ri = R1*Gi+R2*(1-Gi);             % Mixture Specific Constant  [J/kg-K]
```

```
Wi = Ru./Ri;                        % Mixture Molecular Weight    [g/mol]
Xi = Gi.*Wi./W1;                    % Gas 1 Mole Fraction             [-]

yi = 1./(1-Ri./(c1*Gi+c2*(1-Gi))); % Mixture Ratio of Specific heats [-]

% Isentropic Area Ratio Minus Actual Area Ratio [-]
AA = @(M,y) ((2./(y+1)).*(1+(y-1)/2*M^2)).^((y+1)./(2*(y-1)))/M-(De/Dt)^2;

% Mixture Exit Mach Number [-]
for i = 1:length(Gi)
    Me(i) = fzero(@(M) AA(M,yi(i)),[1+1E-6 3]);
end;

Ve = Me.*sqrt(yi.*Ri*T0./(1+(yi-1)/2.*Me.^2));% Mixutre Exit Velocity [m/s]
m  = P0./(Ri*T0).*(1+(yi-1)/2).^(-1./(yi-1)).*sqrt(yi.*Ri*T0./...
    (1+(yi-1)/2))*Dt^2*pi/4;                % Mixture Mass Flow    [kg/s]
ms = Ps/(Ri(1)*Ts)*(1+(yi(1)-1)/2)^(-1/(yi(1)-1))*sqrt(yi(1)*Ri(1)*Ts/...
    (1+(yi(1)-1)/2))*Ds^2*pi/4;             % Seeder  Mass Flow    [kg/s]

% Index Where Gas 2 Equals Seeder Mass Flow [-]
[~,j] = min(abs(m.*(1-Gi)-ms));
Ve(j)

% Gas 1 Flow Rate [SCFM_Gas1]
SCFM1 = m(j)*Gi(j)*R1/Xi(j)*60*293/(14.696*6895*(.0254*12)^3);

% Equivalent Air Flow Rate for Gas 1 at Index j [SCFM_Air]
Qe1   = SCFM1*sqrt(S1);

figure();
subplot(2,1,1);plot(Gi,Ve,Gi(j),Ve(j),'o');
xlabel('Mass Fraction [m_H_e/m_t_o_t]');ylabel('Exit Velocity [m/s]')
subplot(2,1,2);plot(Gi,m.*Gi,Gi,m.*(1-Gi),Gi,m,Gi(j)*[1 1],...
    [ms m(j)*Gi(j)],'o');
xlabel('Mass Fraction [m_H_e/m_t_o_t]');ylabel('Mass Flow Rate [kg/s]');
legend('m_H_e','m_N_2','m_t_o_t');
```

LampPulse.m

```
V0  =    400;   % [V]   Discharge voltage
C   =  66E-6;   % [F]   Capacitance
L   =  39E-6;   % [H]   Inductance
ESR =   6E-4;   % [Ohm] Capacitor equivalent series resistance
DCR =  12E-3;   % [Ohm] Inductor direct current resistance
LER =   1.33;   % [Ohm] Lamp estimated resistance
R   = ESR+DCR+LER;  % [Ohm] Total resistance
dt  = 1E-8;         % [s]   Time step
t   = 0:dt:5E-4;    % [s]   Time vector

y = sqrt(R^2-4*L/C); % [-] Root discriminant
I = V0/y*exp(-R*t/(2*L)).*(exp(y*t/(2*L))-exp(-y*t/(2*L))); % [A] Current
W = I.^2*LER;        % [W] Electrical power

% Calculate the maximum cumulative 50 us segment within entire pulse based
```

```
% on the summed output power
p = ceil(50E-6/dt)-1;
sE = [];
for i = 1:length(t)-p
    sE(i) = sum(W(i:i+p));
end
[~,m]=max(sE);

figure();subplot(2,1,1);plot(t*1E6,W/1E3);xlabel('Time [\mus]');
ylabel('Power [kW]');hold all;h=area(t(m:m+p)*1E6,W(m:m+p)/1E3);
legend(h,'50 \mus Max Pulse');
subplot(2,1,2);plot(t*1E6,I);xlabel('Time [\mus]');
ylabel('Current [A]');ylim([-10 400]);
```

EllipticalReflector.m

```
w  = 120;                          % Mirror half angle around focus
th = linspace(w,-w,10007)*pi/180; % Angle vector

syms p D N
a = D*(N/2-1/(4*tan(th(1))))+p; % Symbolic function of semi-major axis as a
% function of periapsis, projected f-number, mirror half angle, and mirror
% exit width [in]

e = @(a) 1-p/a; % Symbolic function of eccentricity as a function of semi-
% major axis, and periapsis [-]

Df = 2*a*sin(th(1))*(1-e(a)^2)/(1+e(a)*cos(th(1))); % Symbolic function of
% mirror exit width as a function of semi-major axis, eccentricity, and
% mirror half angle [in]

pf = solve(Df==D,p); % Solves system of equations for periapsis
pf = matlabFunction(pf(2)); % Converts positive/real function (2) from
% symbolic to function

D  = 3;                                % Define exit width [in]
N  = 4;                                % Define projected f-number [-]
p  = pf(D,N);                          % Resultant periapsis [in]
a = eval(a);                           % Resultant semi-major axis [in]
r  = (2*a*p-p^2)./(a+(a-p)*cos(th));   % Resultant curve profile radius
% as a function of angle [in]

x0 = 0;                    % Offset focus from source at origin
y0 = 0;

x  = r.*cos(th)+x0;        % Convert to cartesian coordinates
y  = r.*sin(th)+y0;

figure();plot(x,y);axis equal;hold all;

r2  = sqrt(x.^2+y.^2);     % Recalculate curve profile with offset
th2 = sign(y).*acos(x./r2); % Angle for mirror curve offset from source

% 4th order 1st derivative central difference of mirror curve
```

```
for i = 3:length(x)-2
    dydx(i) = 4/3*(y(i-2)/8-y(i-1)+y(i+1)-y(i+2)/8)/(x(i+1)-x(i-1));
end

ref = -1./dydx; % Perpendicular slope to mirror curve

% Generate ray angles and originating cartesian coordinates from source
rayth = linspace(atan2(y(4),x(4)),atan2(y(end-3),x(end-3)),9);
rayx = zeros(length(rayth),3);
rayy = rayx;

% Trace ray intersections and reflections from source to mirror
for i = 1:length(rayth)
    [~,j] = min(abs(th2-rayth(i)));       % Index where source ray
    % intersects mirror

    n(i)  = tan(2*atan(ref(j))-rayth(i)); % Slope of reflected ray
    rayx(i,2) = x(j); % Coordinates of ray/curve intersection
    rayy(i,2) = y(j);
    rayx(1,3) = -min(abs(2*(rayx(1,2)-rayy(1,2)/n(1))),15);  % Distance to
    % project reflected rays (either to y=0 or some defined x distance(15))
    rayx(i,3) = rayx(1,3); % Reflected ray coordinates
    rayy(i,3) = n(i)*(rayx(i,3)-rayx(i,2))+rayy(i,2);
    plot(rayx(i,:),rayy(i,:),'k');
end
```

VerticalElutriator.m

```
%% NITROGEN ONLY %%

% Orifice Diameter   [m]
Dt = ([0.059,0.021,0.016,0.015,0.010,0.008,0.004])*0.0254;
D0 = 3.250*0.0254;          % Pipe Diameter      [m]
Dp = logspace(-7,-5,1000);  % Particle Diameter  [m]
pp = 2650;                  % Particle Density   [kg/m^3]
P0 = 100*6895;              % Stagnation Pres    [Pa]
T0 = 293;                   % Stagnation Temp    [K]
mu = 1.747E-5;              % Viscosity          [Pa-s]
R  = 297;                   % Spec Gas Constant  [J/kg-K]
p0 = P0/(R*T0);             % Stagnation Dens    [kg/m^3]
TT0 = 1/1.2;                % Sonic Temp Ratio   [-]
pp0 = 0.6339;               % Sonic Dens Ratio   [-]
Vt = sqrt(1.4*R*TT0*T0);    % Throat Velocity    [m/s]

for i = 1:length(Dt)
    V0      = Vt*pp0*(Dt(i)/D0)^2;              % Pipe Velocity       [m/s]
    % Ratio of pipe velocity to particle terminal velocity [-]
    Vr(i,:) = V0*18*mu./((pp-p0)*9.81*Dp.^2);
    LEG{i}  = num2str(Dt(i)/.0254);
end

figure();plot(Dp,Vr,'o-');set(gca,'XScale','log','YScale','log');
ylim([1 inf]);
legend(LEG);
```

CycloneCut.m

```
%%%%%%%%%%%%%%%%%%%%%%%%%%%%%%%%%%%%%%%%%%%%%%%%%%%%%%%%%%%%%%%%%%%%%%%%%%%%
% Efficiency equation derived from J. Dirgo and D. Leith, "Cyclone
% Collection Efficiency: Comparison of Experimenal Results with Theoretical
% Predictions," Aerosol Science and Technology, vol. 4, pp. 401-415, 1985.
%%%%%%%%%%%%%%%%%%%%%%%%%%%%%%%%%%%%%%%%%%%%%%%%%%%%%%%%%%%%%%%%%%%%%%%%%%%%

mu  = 1.75E-5; % [Pa-s]    Gas viscosity
MW  = 28;      % [g/gmol]  Gas molecular weight
y   = 1.40;    % [-]       Gas ratio of specific heats
D   = 0.0208;  % [m]       Cyclone nominal diameter
A   = D/2*[1,1,2/5,1,8,3,3/4]; % [m] Stairmand dimensions [De,a,b,S,H,h,B]
dp  = logspace(-7,-5.5,1000);  % [m]       Particle diameter
Q   = linspace(1E-5,2E-4,5);   % [m^3/s]   Volumetric flow rate
rhp = 4230;                    % [kg/m^3]  Particle density
T0  = 295;                     % [K]       Stagnation temperature
vt  = sqrt(y*8314*T0*2/(MW*(1+y)));           % [m/s] Orifice velocity
dt  = sqrt(4*Q*((1+y)/2)^(1/(y-1))./(pi*vt)); % [m]   Orifice diameter

figure;hold all;

hstar = (A(5)-A(6))*(D-A(1))/(D-A(7))+(A(6)-A(4)); % [-] Non-dimensional
% parameter for efficiency equation

% Iterate to find efficiency for each flowrate
for i = 1:length(Q)
    vt   = Q(i)/(pi*A(1)^2/4)*(A(1)/2)*(D-A(3))*pi/(2*A(2)*A(3)*...
        (1-1.2*A(3)/D)+hstar*(D-A(3))*.02*pi);
    % [m/s] Tangential gas velocity

    vtsvstar = pi*hstar*vt^2*rhp*dp.^2/(9*mu*Q(i));
    % [-] Ratio of tangential gas velocity to settling velocity

    semilogx(dp*1E6,1./(1+vtsvstar.^-3.2)); % Plot efficiency vs particle
    % diameter

    leg{i} = num2str(dt(i)/.0254,'%5.3f in');
end

xlabel('Partcile Size [\mum]');ylabel('Filtering Efficiency [%]');
legend(leg,'Location','SouthEast');
```

VariableVelocityExplicitStep.m

```
geo = input('Generate New Geometry? (y/n): ','s');

y   = 1.4; % Ratio of Specific Heats [] (1.15 for MMH/RFNA)
R   = 8314.5/28; % Specific Gas Constant [J/kg-K] (MW~21.735 for MMH/RFNA)
To  = 288; % Stagntation temperature [K] (~2962 for MMH/RFNA)
Po  = 100*6894.76; % Stagnation pressure[Pa]
muo = 1.781E-5; % Viscosity [Pa*s] (N2 - 1.781E-5, MMH/RFNA - 1E-4)
C   = 111; % Sutherland's Constant [K] (N2 - 111, MMH/RFNA - NaN)
Tr  = 300; % Sutherland's Reference Temperature [K]
```

```
dp  = 1000E-9; % Particle Diameter [m]
rhp = 2650; % Particle Density [kg/m^3] (TiO2 4230, SiC 3216, SiO2 2650)

%% Geometry Definition
if geo == 'y'
    AA  = @(M)((y+1)/2)^((y+1)/(2*(1-y)))*(1+M^2*(y-1)/2)^...
        ((y+1)/(2*(y-1)))/M; % Area Ratio as a Function of Mach Number []
    L   = 0.800*.0254;       % [m] Total Nozzle Length
    Lc  = 0.286*.0254;       % [m] Contraction Length (Entrance to Throat)
    rc  = 0.275*.0254;       % [m] Contraction Curve Radius
    rt  = 0.0915*.0254;      % [m] Throat Radius
    re  = 0.112*.0254;       % [m] Exit   Radius

    dx = 1E-6; % [m] Axial length step
    x1 = 0:dx:Lc; % [m] Contraction axial position vector
    r1 = rt+rc*(1+sin(-acos((x1-rc)/rc))); % [m] Contraction radius vector
    x2 = x1(end):dx:L;  % [m] Expansion axial position vector
    r2 = linspace(r1(end),re,length(x2)); % [m] Expansion radius vector

    x = [x1,x2(2:end)]-rc; % [m] Combined axial position vector
    r = [r1,r2(2:end)]; % [m] Combined radius vector

    %% Isentropic Flow
    AAi = (r/rt).^2;        % Area Ratio []
    i=2;
    opt = optimoptions('fsolve','TolFun',1E-12,'Display','off');
    Mi  = zeros(1,length(x));
    Mi(1) = fsolve(@(M)AAi(1)-AA(M),0.1,opt);            % [] Mach Number

    while x(i)<0
        Mi(i) = fsolve(@(M)AAi(i)-AA(M),Mi(i-1),opt);
        % [] Subsonic Contraction
        i = i+1;
    end

    for j = i:length(x)
        Mi(j) = fsolve(@(M)(AAi(j)-AA(M)),Mi(i-1)+.1,opt);
        % [] Supersonic Expansion
    end
else
    load('VariableVelocityExplicitStep.mat'); % Previous nozzle data to
    % to save computation time
end

v    = sqrt(y*R*To./(1+(y-1)/2*Mi.^2)).*Mi;
% [m/s] Flow Velocity as a function of x

FDc  = [1/280,-4/105,1/5,-4/5,0,4/5,-1/5,4/105,-1/280];
% First Derivative 8th Order Central Finite Difference

lFDc = (length(FDc)-1)/2;
FDf  = [-49/20,6,-15/2,20/3,-15/4,6/5,-1/6];
% First Derivative 6th Order Forward/Backward

lFDf = length(FDf)-1;
```

```
dvdx = zeros(1,length(v));

% Perform forward/backward differencing on initial and final positions
for i =1:4
    dvdx(i)  = sum(FDf.*v(i:(i+lFDf)))/(x(i+1)-x(i));
    % [1/s] Derivative of Flow Velocity with Respect to x
    dvdx(length(v)-i+1) = sum(-FDf.*v((length(v):-1:...
        (length(v)-lFDf))-i+1))/(x(length(v)-i+1)-x(length(v)-i));
end

% Perform central differencing on intermediate positions
for i = 5:length(v)-4
    dvdx(i)  = sum(2*FDc.*v((i-lFDc):(i+lFDc)))/(x(i+1)-x(i-1));
    % [1/s] Derivative of Flow Velocity with Respect to x
end

%% Explicit Solver for Particle
rho = Po/(R*To); % Fluid Stagnation Density         [ kg/m^3]
ph  = 1;         % Particle to Fluid Velocity Ratio [ Vp/Vf ]
vp  = v(1)*ph;   % Particle Velocity                [  m/s  ]
xp  = x(1);      % Particle Position                [   m   ]
i   = 2;
dt  = 1e-7;      % Time step [s]

while xp(i-1)<x(end)
    Mf  = interp1(x,Mi,xp(i-1)); % Fluid Mach Number         [   -   ]
    Tf  = To/(1+(y-1)/2*Mf^2);   % Fluid Temperature         [   K   ]
    rhf = rho*(Tf/To)^(1/(y-1)); % Fluid Density             [ kg/m^3]
    vf  = Mf*sqrt(y*R*Tf);       % Fluid Velocity            [  m/s  ]
    if isnan(C)
        muf = muo;
    else
        muf = muo*(Tr+C)*(Tf/Tr)^1.5/(Tf+C); % Fluid Viscosity [Pa-s]
    end
    Re(i) = rhf*(vf-vp(i-1))*dp/muf; % Reynolds Number [-]
    n(i)  = min([150/(175*Re(i)^0.15+3*Re(i)),1]); % Correction Factor [-]
    dv    = interp1(x,dvdx,xp(i-1)); % Fluid Velocity Gradient [1/s]
    a     = n(i)*rhp*dp^2/(9*muf);   % Time Constant [s]
    z     = sqrt(1+2*a*dv); % Root of Discriminant [-]
    ph(i) = vp(i-1)/vf; % Particle to fluid velocity ratio [-]
    vp(i)  = vf*exp(-dt/a)*(ph(i)*cosh(dt*z/a)+(2-ph(i))*sinh(dt*z/a)/z);
    % Governing particle acceleration equation [m/s]
    xp(i)  = xp(i-1)+vp(i)*dt; % Step to next position [m]
    i      = i+1;
end

figure();
subplot(2,1,1);hold all; plot(xp, vp,x,v);xlim([xp(1) x(end)]);
subplot(2,1,2);hold all;plot(xp,ph);axis([xp(1) x(end) 1.1*min(ph)-.1 1]);
```

PeakDetection.m

```
SCFile = 'StreakN2224'; % Set streak filename
DATA = double(hdfread([SCFile,'.hdf'],'/fore')); % Load streak data
info = hdfinfo([SCFile,'.hdf']); % Extract streak metadata
```

```
[tinfo] = textscan(info.SDS.Attributes(1,103).Value,'%f %f %s',...
    'delimiter',','); % Slope, intercept, and unit of time vector
tinfo{1}=tinfo{1};

switch tinfo{3}{1} % Scale time slope to seconds/pixel
    case 'ns'
        ts = tinfo{1}*1E-9;
    case 'us'
        ts = tinfo{1}*1E-6;
    case 'ms'
        ts = tinfo{1}*1E-3;
    otherwise
        fprintf('Time Scale Error');
end

yscale = 22.0569;   % [um/pixel] Define spatial scale for the given test
db = DATA(441:740,1:1360);  % Define the portion of streak data to filter
tax = tinfo{1}*(1:1360)+tinfo{2};
% [s] Generate time vector from hdf slope-intercept string data

yax = yscale*((441:740)-491); % [um] Generate space vector for cropped
% domain (set 0 intercept as nozzle exit)

FD = fftshift(fft2(db)); % 2D Fourier transform of cropped domain
sD = size(FD); % Store size of domain

n  = FourierSlope(FD,.9); % [pix/pix] Find mean slope of peaks in Fourier
% transform to an Rsquare of 0.9

%% Define Hyperbolic Filter
th = atan(n); % [rad] Calculate angle from mean slope
m  = tan(atan(1/n.*([.95 1/.95]))-th); % [pix/pix] Calculate +/- 5% bands
% of slope and rotate to horizontal by theta

x0 = floor(sD(2)/2)+1; % [pix] Locate center of Fourier transform
y0 = floor(sD(1)/2)+1; % [pix]

a  = 3; % [pix] Hyperbola vertex to origin distance
b  = a*2/abs(m(2)-m(1)); % [pix/pix] Hyperbola asymptote slope
t  = linspace(-x0*2,x0*2,1E5); % [pix] Vertical array of hyperbola set much
% larger than the Fourier domain in order to reach edges

s  = a/b*sqrt(t.^2+b^2);
% [pix] Calculate horizontal hyperbola locations from t

s  = [s,-s]; % Define left and right hyperbolas
t  = [t, t];

C  = [cos(th) sin(th);-sin(th) cos(th)]; % Define direction cosine matrix
A  = C*[s;t]; % Rotate hyperbola
x  = A(1,:)+x0; % Translate hyperbola to Fourier center
y  = A(2,:)+y0;

% Iterate through Fourier columns and determine pixel locations where
```

```
% hyperbola overlaps
for i = 1:sD(2)
    [~,J(i)] = min(abs(x(1:length(x)/2)-i));
    [~,K(i)] = min(abs(x(1+length(x)/2:end)-i));
    K(i) = K(i)+length(x)/2;
end

% Determine the corresponding pixel rows for the upper and lower hyperbola
% curves; round the edges to fit within the Fourier domain
ly1 = round(y(J));
ly2 = round(y(K));
ly1(ly1>sD(1)) = sD(1);
ly2(ly2>sD(1)) = sD(1);
ly1(ly1<1)     = 1;
ly2(ly2<1)     = 1;

% Define a zero matrix and populate the pass filter with ones between the
% upper and lower curves
Flt = zeros(sD);
for i = 1:sD(2)
    if ly2(i) ~= ly1(i)
        Flt(ly2(i):ly1(i),i)=1;
    end
end

%% Filter Image and Locate Peaks
FD2  = FD.*Flt; % Apply the filter to the Fourier transform
df   = abs(ifft2(fftshift(FD2))); % Take the inverse transform
plt  = [];
ply  = [];
wnd  = [205 1154 1 300]; % Set the window within the new domain to apply
% the peak finding algorithm (choosing less than 90% of time axis ensures
% streak sweep calibration is preserved; choosing y axis that extend past
% laser sheet may help with background adjustments)

rss = 1; % Resampling rate (interpolates between pixels to better locate
% peak position

[dls]     = mslowess((wnd(1):wnd(2))',df(wnd(3):wnd(4),wnd(1):wnd(2))',...
'Span',16); % Smooth y
[dba]     = msbackadj((wnd(3):wnd(4))',dls','WindowSize',50,...
    'StepSize',2); % Linearize baseline signal
[trs,dtr] = msresample((wnd(1):wnd(2))',dba',(wnd(2)-wnd(1))*rss);
% Resample time

[yrs,dyr] = msresample((wnd(3):wnd(4))',dtr',(wnd(4)-wnd(3))*rss);
% Resample y

[p,pl]   = mspeaks(trs,dyr','HeightFilter',50,'OverSegmentationFilter',30);
% Locate peaks

% Reshape peak locations to a single column for plotting
for i = 1:length(p)
    plt = [plt;p{i}(:,1)];
    ply = [ply;yrs(i)*ones(size(p{i},1),1)];
```

```
end
%% Proceed to PeakDisplacement.m to analyze slopes

% Sample Plot options
%
% figure('units','normalized','outerposition',[0 0 1 1]);
% subplot(4,1,1);imagesc(db);axis equal tight
% subplot(4,1,2);imagesc(abs(FD2),[0 20]);axis equal tight;axis([sD(2)*...
% [.3 .7] -Inf Inf]);
% subplot(4,1,3);imagesc(db);axis equal tight;hold all;plot([wnd(1)...
% wnd(1) wnd(2) wnd(2) wnd(1)],[wnd(3) wnd(4) wnd(4) wnd(3) wnd(3)],'r',...
% plt,ply,'w.','MarkerSize',4);
% subplot(4,1,4);imagesc(trs,yrs,dyr,[0 20]);axis equal tight
%
% figure('units','inches','paperposition',[0 0 6.5 2.5],'position',...
% [0 0 6.5 2.5]);
% imagesc(tax,yax/1000,db,[0 .7*max(max(db))]);xlabel(['Time [\mus]']);...
% ylabel('Distance from Nozzle Exit [mm]');
% print([SCFile,'_RawStreak'],'-dtiff','-r300');
% %savefig([SCFile,'_RawStreak']);
%
% figure('units','inches','paperposition',[0 0 6.5 2.5],'position',...
% [0 0 6.5 2.5]);
% imagesc([-.5 .5],[-.5 .5],abs(FD2),[0 max(abs(FD2(:,floor(sD(2)/2)+10)...
% ))]);xlabel('Cycles/t_p_i_x [-]');ylabel('Cycles/y_p_i_x [-]');...
% axis([-.1 .1 -.1 .1]);
% print([SCFile,'_FFT'],'-dtiff','-r300');
% %savefig([SCFile,'_FFT']);
%
% figure('units','inches','paperposition',[0 0 6.5 2.5],'position',...
% [0 0 6.5 2.5]);
% imagesc(tax,yax/1000,db,[0 .7*max(max(db))]);hold all;plot(plt*...
% tinfo{1}+tinfo{2},(ply-50)*yscale/1000,'.w','MarkerSize',4);plot(...
% [205 205]*tinfo{1}+tinfo{2},([1 300]-51)*yscale,'r',[1154 1154]*...
% tinfo{1}+tinfo{2},([1 300]-51)*yscale,'r','LineWidth',2);xlabel(...
% ['Time [\mus]']);ylabel('Distance from Nozzle Exit [mm]');
% print([SCFile,'_Peaks'],'-dtiff','-r300');
% %savefig([SCFile,'_Peaks']);
%
% figure('units','inches','paperposition',[0 0 6.5 2.5],'position',...
% [0 0 6.5 2.5]);
% imagesc(tax,yax/1000,dyr,[0 250]);xlabel(['Time [\mus]']);
% ylabel('Distance from Nozzle Exit [mm]');
% print([SCFile,'_FilteredStreak'],'-dtiff','-r300');
% %savefig([SCFile,'_FilteredStreak']);
```

PeakDisplacement.m

```
%% Take calculated data from PeakDetection.m

deltax = NaN(length(p),max(cellfun('length',p)));
px     = NaN(length(p),1);
py     = NaN(length(p),1);
dx = [];

maxDisp = 4; % Set a maximum displacement to filter jumps from one streak
% to the next (could be replaced with better object detection; causes
% issues with identifying outliers vs spurious data

yDisp = 1; % Set the number of rows to look ahead (smaller numbers cause
% statistical issues where the x displacement for a given y displacement
% can only take values of 0 or 1 (for example)) could be replaced with
% polynomial fits over a few points but maintaining local data

% Iterate along each row and calculate the displacement of neighboring
% peaks
for i = 1:length(p)-yDisp
    if ~isempty(p{i+yDisp})
        for j = 1:size(p{i},1)
            [G H] = min(abs(p{i+yDisp}(:,1)-p{i}(j,1)));
            if G < maxDisp/rss
                deltax(i,j) = G*sign(p{i+yDisp}(H,1)-p{i}(j,1));
                if sign(p{i+yDisp}(H,1)-p{i}(j,1))<0
                    deltax(i,j) = NaN;
                end
            end
        end
    end
end


KK = [51 248]; % Set the y-domain bounds to average the displacements over
DX = reshape(deltax(KK(1):KK(end),:),[],1);
v  = yscale/(rss*tinfo{1}*nanmean(DX)) % [m/s] Mean velocity
```

APPENDIX B. MACHINE DRAWINGS

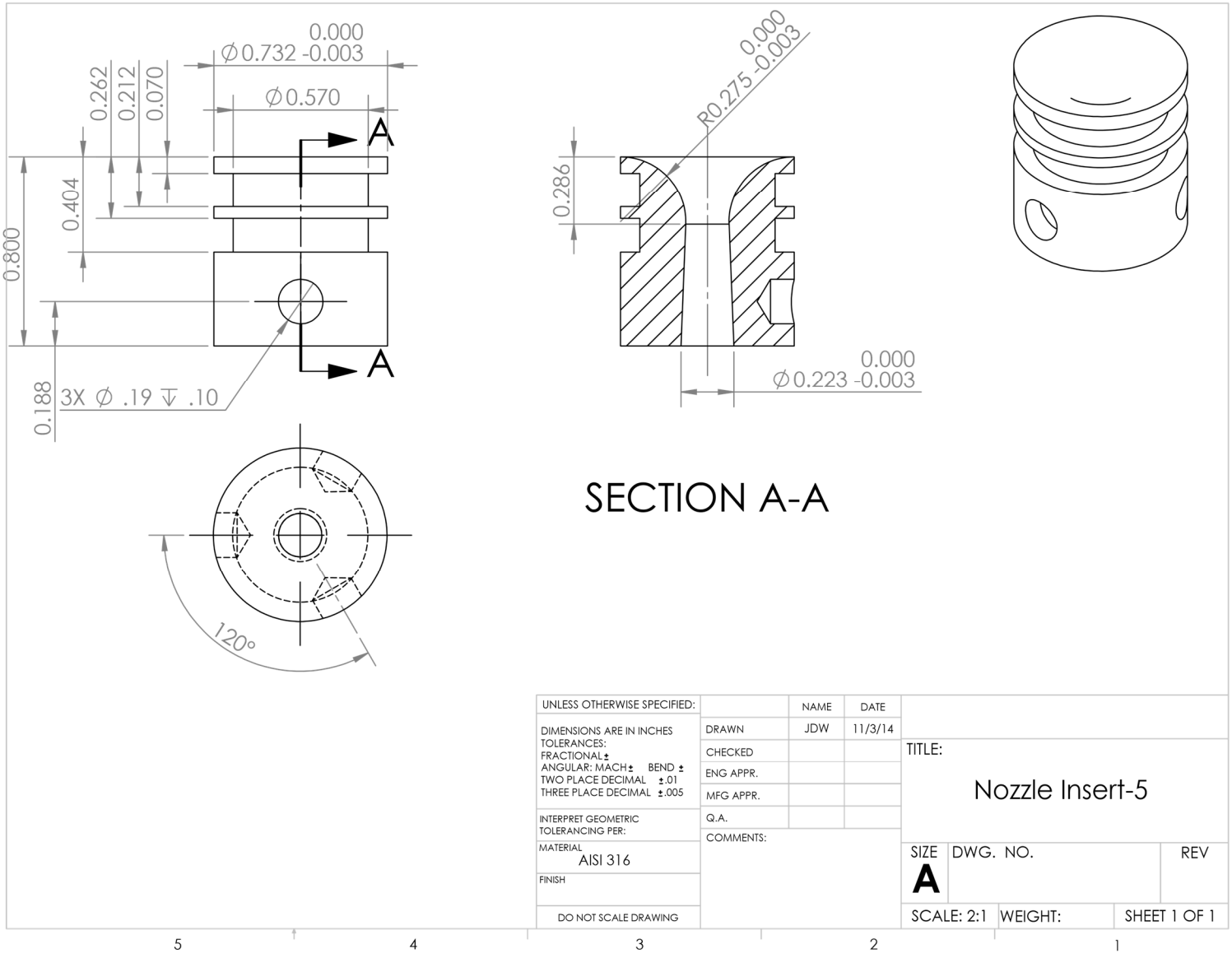

Figure 76. Converging-Diverging Conical Nozzle Machine Drawing

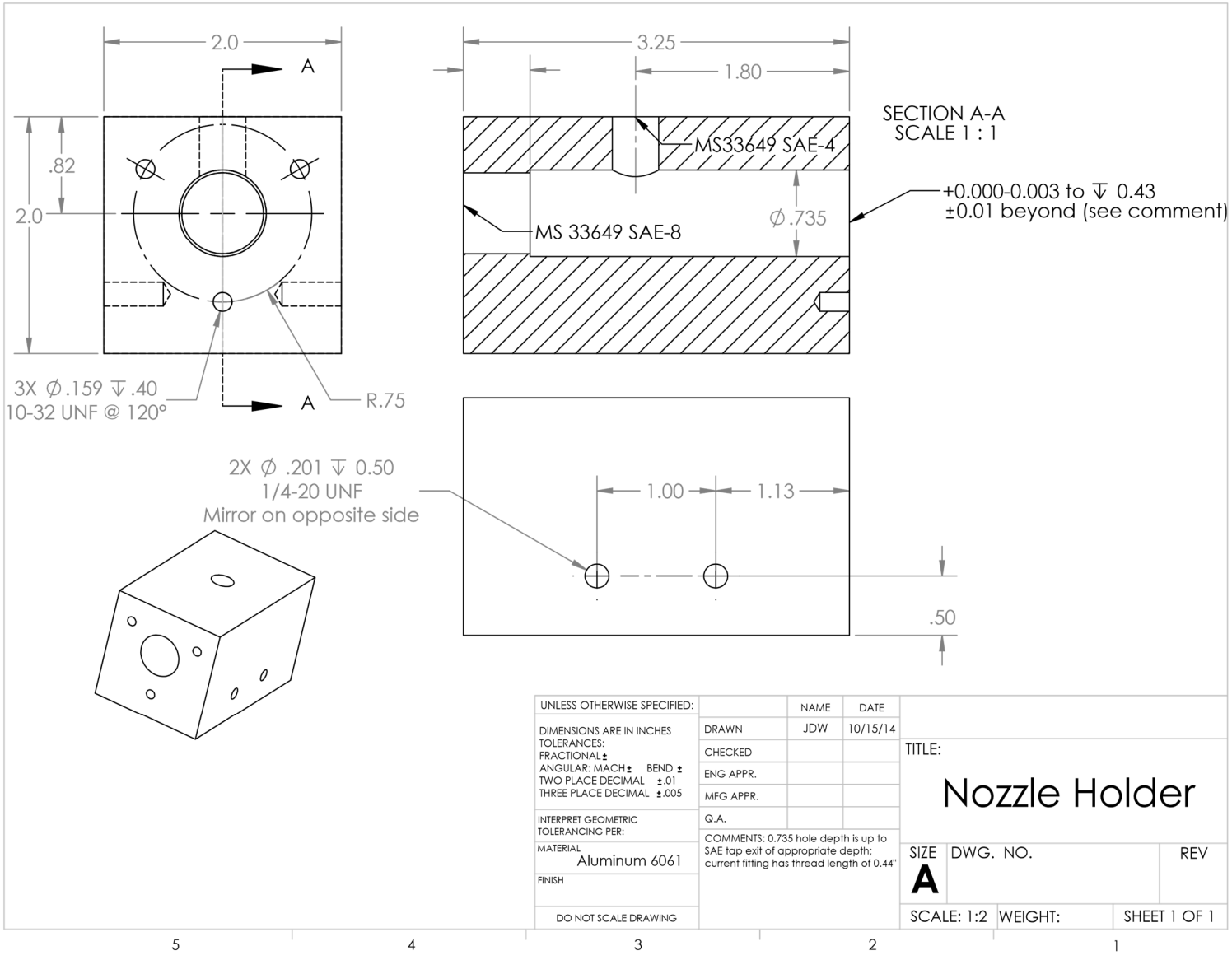

Figure 77. Nozzle Holder Machine Drawings

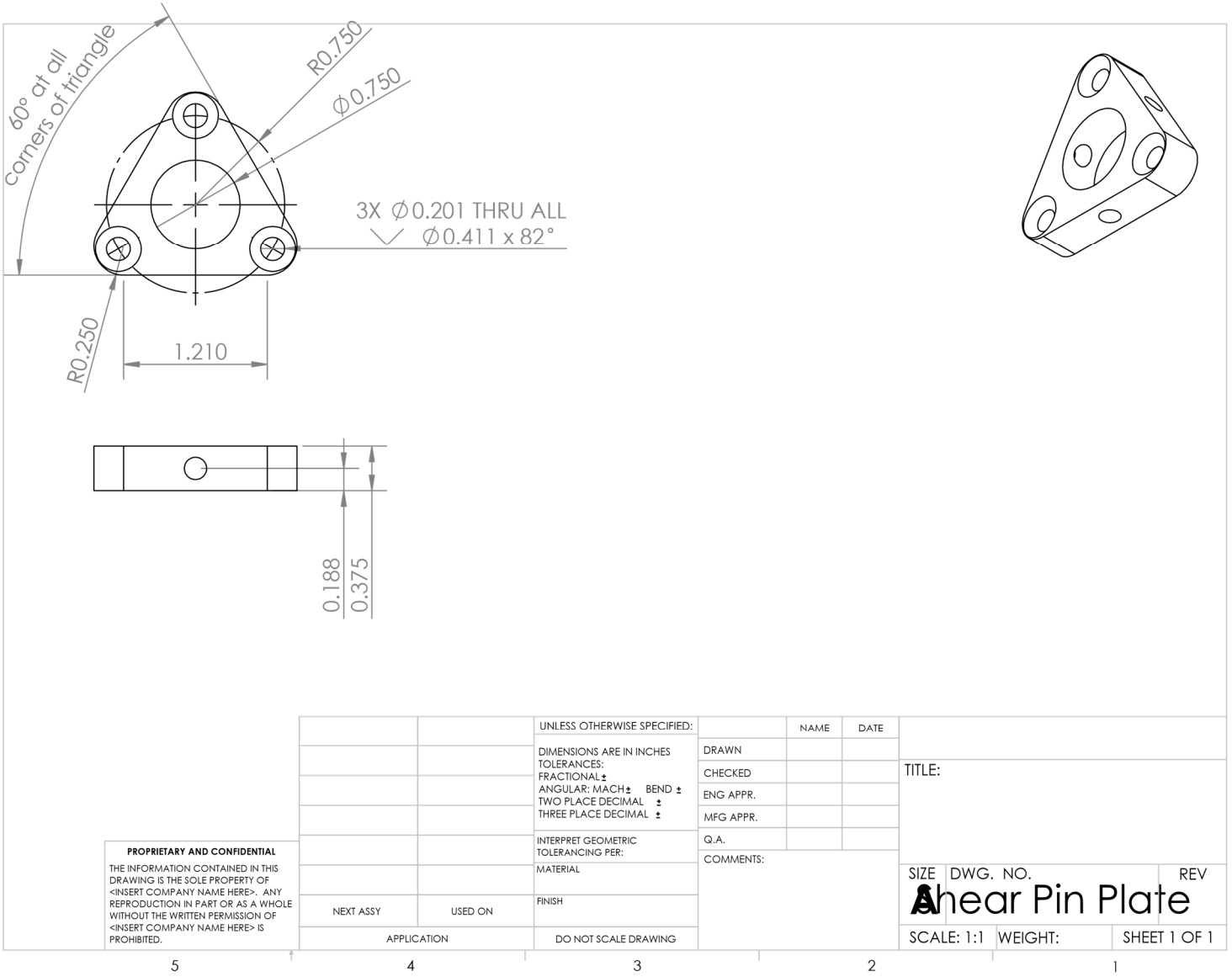

Figure 78. Nozzle Retaining Shear Pin Plate Machine Drawings

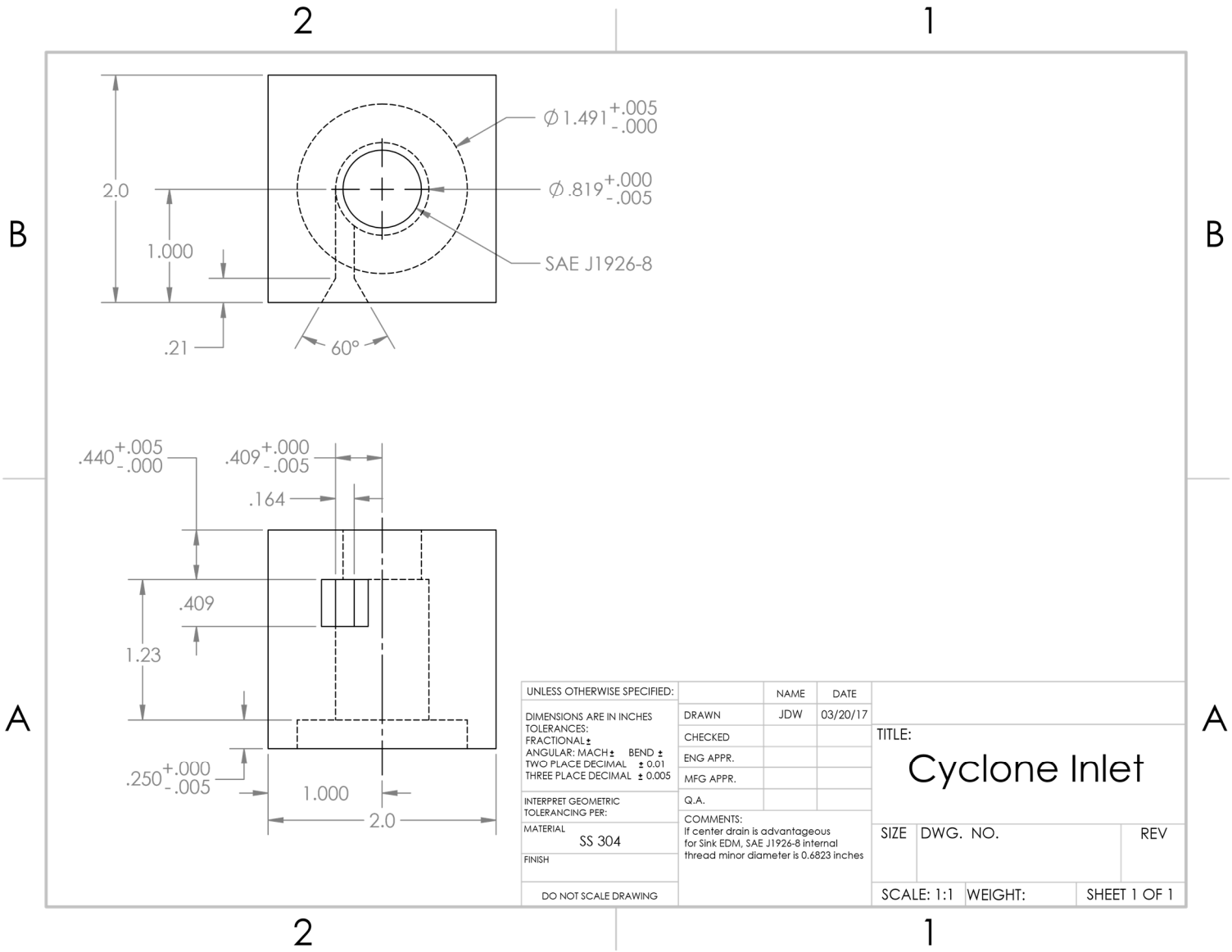

Figure 79. Cyclone Filter Cylinder Machine Drawings

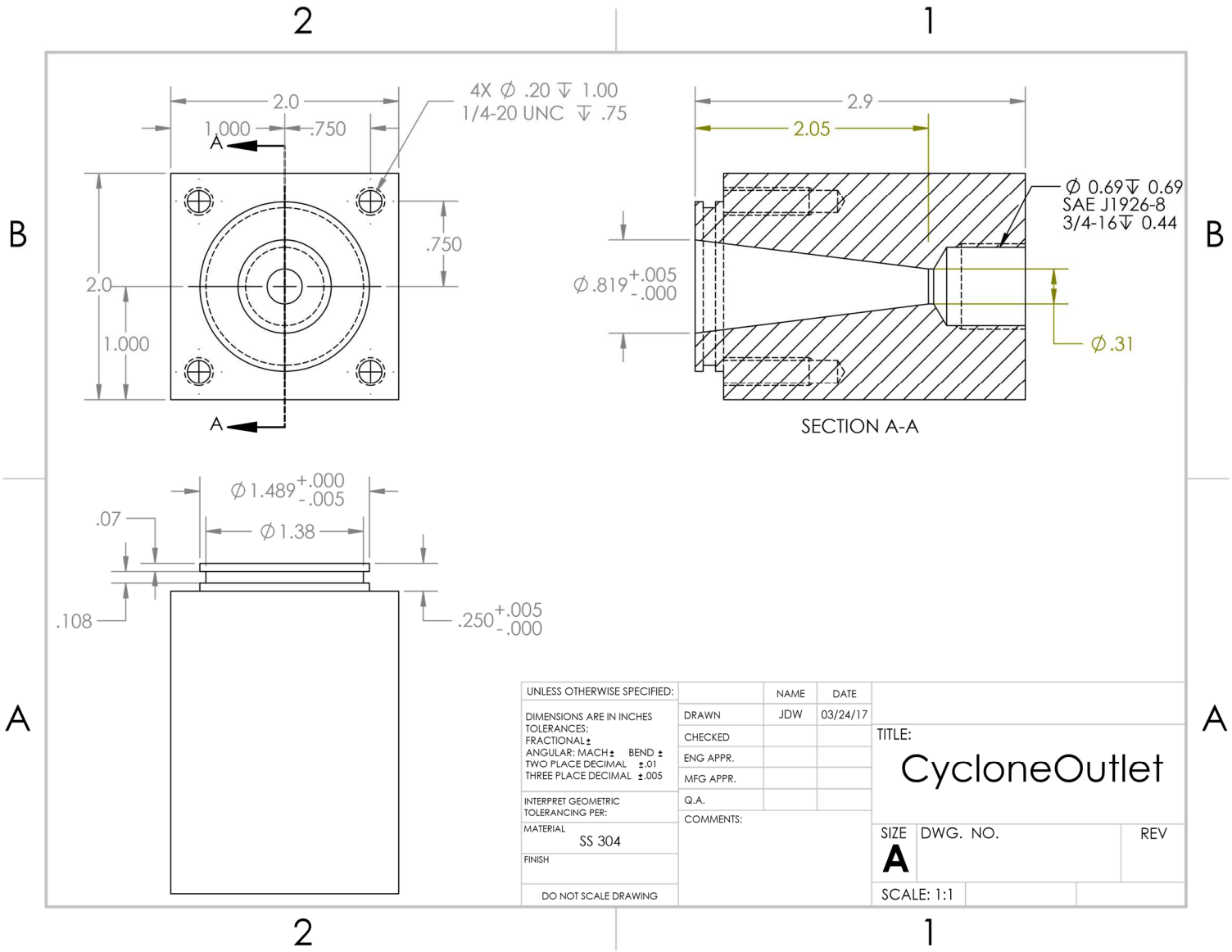

Figure 80. Cyclone Filter Cone Machine Drawings

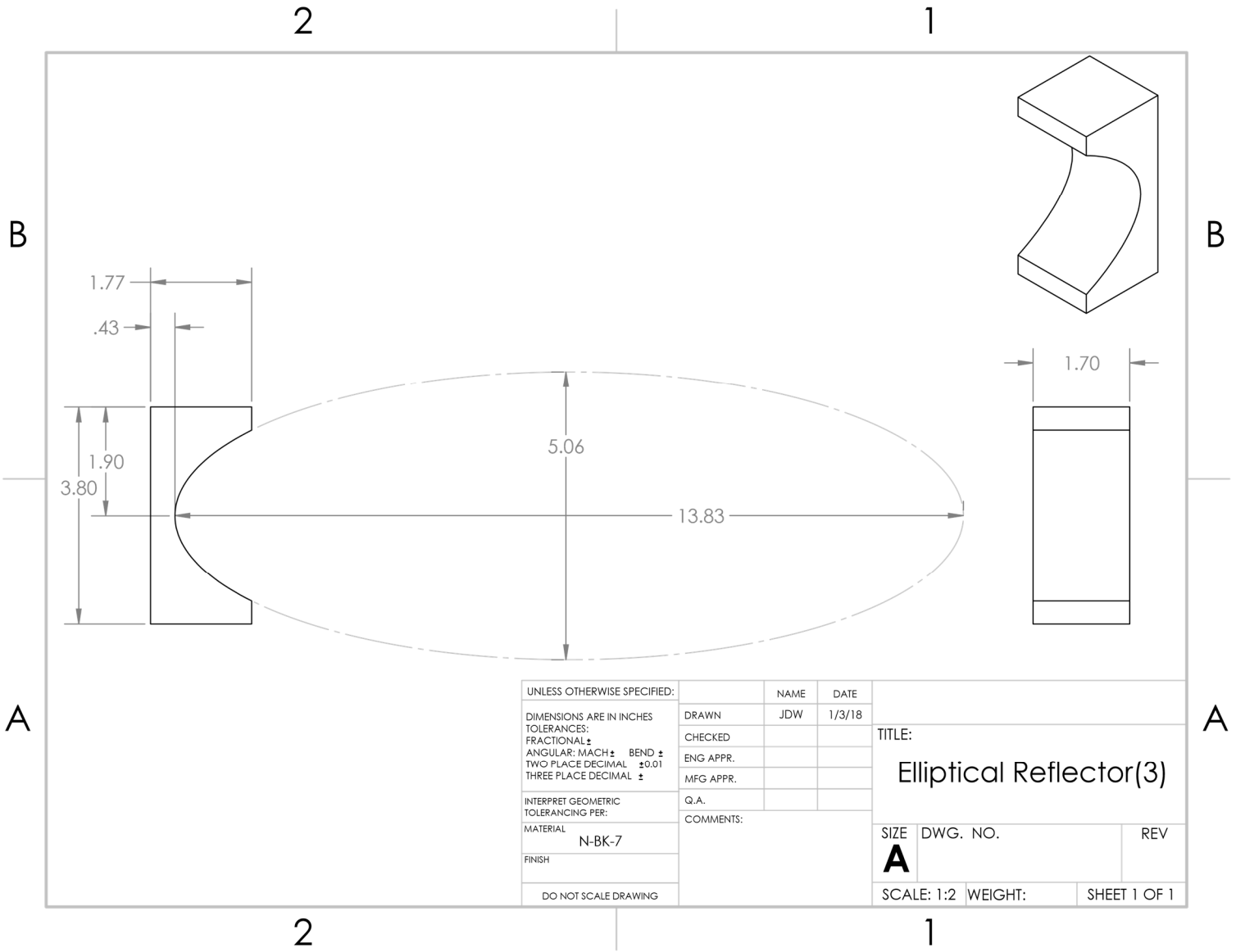

Figure 81. Flashlamp Elliptical reflector Machine Drawings

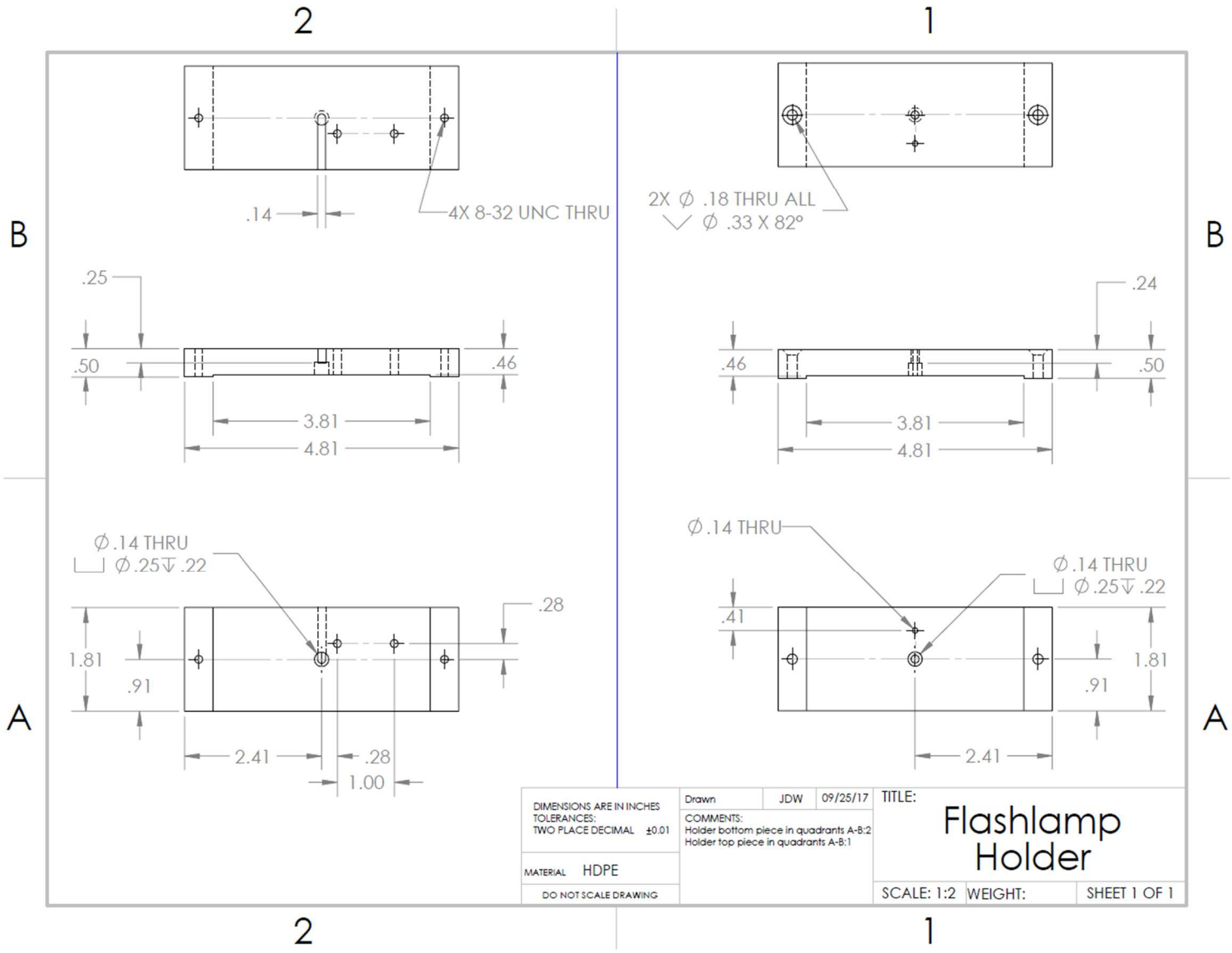

Figure 82. Flashlamp Holder Machine Drawings

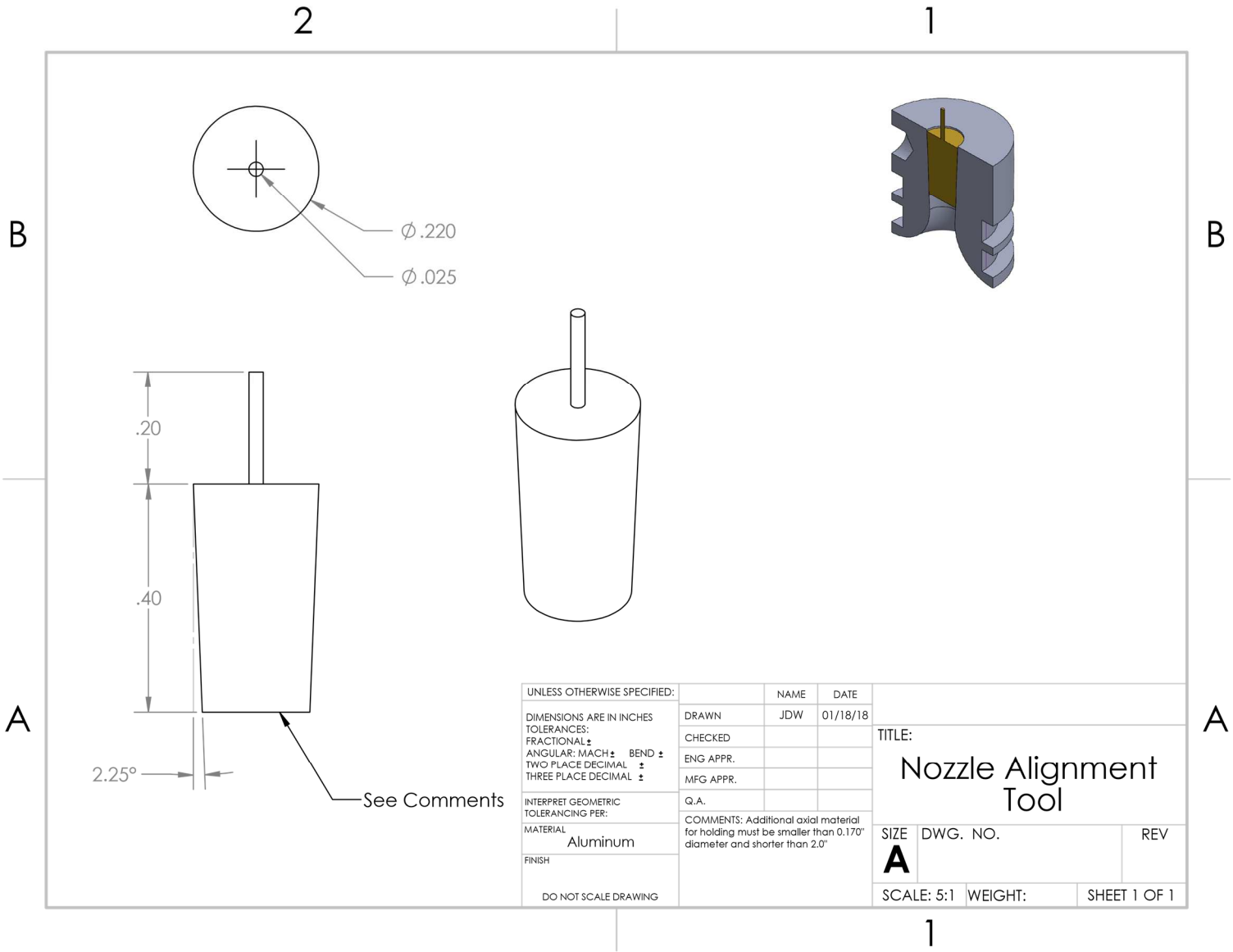

Figure 83. Nozzle Alignment Pin Machine Drawings

APPENDIX C. DERIVATION

Begin with Newton's second law:

$$F_D = m_p \ddot{x}_p$$

Define the particle as a sphere to find the mass:

$$m_p = \frac{\pi \rho_p d_p^3}{6}$$

Use Stokes drag to define the force imparted on the particle:

$$F_D = \frac{1}{2} \; _D \; _p \rho_f v_{rel} = \frac{_D \pi \rho_f d_p}{8} \left(v_f - \dot{x}_p\right)$$

$$_D = \frac{24\mu}{\rho_f \left(v_f - \dot{x}_p\right) d_p B}$$

Include a correction factor for higher Reynolds number:

$$B = \begin{cases} \dfrac{150}{175 Re^{\cdot \; 5} + 3Re}, & 1 < Re < 2000 \\ 1, & 1 \leq Re \end{cases}$$

Combine the definitions into the initial equation and reduce:

$$\frac{\pi \rho_p d_p^3}{6} \ddot{x}_p = \frac{3\pi d_p \mu}{B} \left(v_f - \dot{x}_p\right)$$

Define a time constant to simplify the equation:

$$\alpha \equiv \frac{B\rho d_p}{9\mu}$$

Assume a linearly accelerating flow velocity across the step over which the analysis is performed:

$$v_{f_{i+}} = v_{f_i} + \int_{x_i}^{x_{i+1}} \frac{dv_f}{dx} dx \approx v_{f_i} + \Delta x \frac{dv_f}{dx}\Big|_{x_i} \quad for\ sm\ \ ll \Delta x$$

$$v_f \approx v_{f_0} + c\ x$$

The following 2nd order differential equation is obtained:

$$\frac{\alpha}{2}\ddot{x} + \dot{x} - c\ x = v_{f_0}$$

The particular solution yields a constant:

$$x = x_{general} + x_{particular}$$

$$x_{particular} = c$$

$$\frac{\alpha\ddot{c}}{2} + \dot{c} - c\ c = v_{f_0} \rightarrow c = -\frac{v_{f_0}}{c}$$

The general solution has the following characteristic roots:

$$\frac{\alpha\ddot{x}_g}{2} + \dot{x}_g - c\ x_g = v_{f_0}$$

$$R = \frac{-1 \pm \sqrt{1 + 2\alpha c}}{\alpha}$$

Define another variable to simplify the equation

$$\Upsilon = \sqrt{1 + 2\alpha c}$$

The general solution is as follows:

$$x_g(t) = e^{-\frac{t}{\alpha}}\left(c_3 \cosh\left(\frac{t\Upsilon}{\alpha}\right) + c_4 \sinh\left(\frac{t\Upsilon}{\alpha}\right)\right)$$

Combining with the particular solution yields *x(t)* and its derivative:

$$x(t) = e^{-\frac{t}{\alpha}}\left(c_3 \cosh\left(\frac{t\Upsilon}{\alpha}\right) + c_4 \sinh\left(\frac{t\Upsilon}{\alpha}\right)\right) - \frac{v_{f_0}}{c}$$

$$\dot{x}(t) = \frac{e^{-\frac{t}{\alpha}}}{\alpha}\left([c_3\Upsilon - c_4] \sinh\left(\frac{t\Upsilon}{\alpha}\right) + [c_4\Upsilon - c_3] \cosh\left(\frac{t\Upsilon}{\alpha}\right)\right)$$

Evaluate the functions at zero to solve for the coefficients:

$$x(0) = 0 = c_3 - \frac{v_{f_0}}{c}$$

$$c_3 = \frac{v_{f_0}}{c}$$

$$\dot{x}(0) = v_{p_0} = \frac{c_4\Upsilon - c_3}{\alpha}$$

$$c_4 = \frac{1}{\Upsilon}\left(\alpha v_{p_0} + \frac{v_{f_0}}{c}\right) = \frac{v_{f_0}}{c\ \Upsilon}(\alpha c\ \phi + 1)$$

Recombine the coefficients with the 1st derivative and simplify to calculate the particle velocity:

$$\dot{x}(t) = v_{f_0} e^{-\frac{t}{\alpha}}\left(\phi \cosh\left(\frac{t\Upsilon}{\alpha}\right) + \frac{\Upsilon\ -(\alpha c\ \phi + 1)}{\alpha c\ \Upsilon} \sinh\left(\frac{t\Upsilon}{\alpha}\right)\right)$$

$$v_p = \dot{x}(t) = v_{f_0} e^{-\frac{t}{\alpha}}\left(\phi \cosh\left(\frac{t\Upsilon}{\alpha}\right) + \frac{2 - \phi}{\Upsilon} \sinh\left(\frac{t\Upsilon}{\alpha}\right)\right)$$

REFERENCES

[1] P. V. Ramachandran, A. S. Kulkarni, M. A. Pfeil, J. D. Dennis, J. D. Willits, S. D. Heister, S. F. Son and T. L. Pourpoint, "Amine-Boranes: Green Hypergolic Fuels with Low Ignition Delays," *Chemistry - A European Journal,* vol. 20, no. 51, pp. 16869-16872, 2014.

[2] M. A. Pfeil, J. D. Dennis, S. F. Son, S. D. Heister, T. L. Pourpoint and P. V. Ramachandran, "Characterization of Ethylenediamine Bisborane as a Hypergolic Hybrid Rocket Fuel Additive," *Journal of Propulsion and Power,* vol. 31, no. 1, pp. 365-372, 2015.

[3] J. D. Dennis, S. F. Son and T. L. Pourpoint, "Critical Ignition Criteria for Monomethylhydrazine and Red Fuming Nitric Acid in an Impinging Jet Apparatus," *Journal of Propulsion and Power,* vol. 31, no. 4, pp. 1184-1192, 2015.

[4] J. D. Dennis, J. D. Willits and T. L. Pourpoint, "Performance of Neat and Gelled Monomethylhydrazine and Red Fuming Nitric Acid in an Unlike-Doublet Combustor," *Combustion Science and Technology,* Accepted for Publication 12 Jan 2018.

[5] A. Ferri, "Review of SCRAMJET Propulsion Technology," *Journal of Aircraft,* vol. 5, no. 1, pp. 3-10, 1968.

[6] S. N. B. Murthy and E. T. Curran, Scramjet Propulsion, AIAA, 2001.

[7] F. A. Bykovski, S. A. Zhdan and E. F. Vedernikov, "Continuous Spin Detonations," *Journal of Propulsion and Power,* vol. 22, no. 6, pp. 1204-1216, 2006.

[8] M. N. Wendt, P. A. Jacobs and R. J. Stalker, "Displacement Effects and Scaling of Ducted, Supersonic Flames," *Combustion and Flame,* vol. 116, no. 4, pp. 593-604, 1999.

[9] G. D. Roy, S. M. Frolov, A. A. Borisov and D. W. Netzer, "Pulse Detonation Propulsion: Challenges, Current Status, and Future Perspective," *Progress in Energy and Combustion Science,* vol. 30, pp. 545-672, 2004.

[10] M. L. Fotia, F. Schauer, T. Kaemming and J. Hoke, "Experimental Study of the Performance of a Rotating Detonation Engine with Nozzle," *Journal of Propulsion and Power,* vol. 32, pp. 674-681, 2016.

[11] R. W. Ladenburg, B. Lewis, R. N. Pease and H. S. Taylor, "Physical Measurements in Gas Dynamics and Combustion," *High Speed Aerodynamics and Jet Propulsion,* vol. 9, 1954.

[12] D. Estruch, N. J. Lawson and K. P. Garry, "Application of Optical Measurement Techniques to Supersonic and Hypersonic Aerospace Flows," *Journal of Aerospace Engineering,* vol. 22, no. 4, pp. 383-395, 2009.

[13] P. Diodati, N. Paone, G. L. Rossi and E. P. Tomasini, "Comparison of Laser-Doppler Velocimetry, Hotwire Anemometry, and Particle Image Velocimetry for the Investigation of a Turbulent Jet," in *Fifth International Conference on Laser Anemometry*, Veldehoven, Netherlands, 1993.

[14] G. S. Settles, Schlieren and Shadowgraph Techniques, Springer, 2001.

[15] R. Schodl, I. Röhle, C. Willert, M. Fischer, J. Heinze, C. Laible and T. Schilling, "Doppler Global Velocimetry for the Analysis of Combustor Flows," *Aerospace Science and Technology,* vol. 6, pp. 481-493, 2002.

[16] A. Melling, "Tracer Particles and Seeding for Particle Image Velocimetry," *Measurement Science and Technology,* vol. 8, pp. 1406-1416, 1997.

[17] B. J. Balakumar and R. J. Adrian, "Particle-Image Velocimetry Measurement in the Exhaust of a Solid Rocket Motor," *Experiments in Fluids,* vol. 36, pp. 166-175, 2004.

[18] M. C. Ramsey, T. C. Folk, A. N. Perkins and R. W. Pitz, "Assessment of the Application of Hydroxyl Tagging Velocimetry to Rocket Engines," in *45th AIAA/ASME/SAE/ASEE Joint Propulsion Conference*, Denver, CO, 2009.

[19] M. C. Ramsey, R. W. Pitz, T. P. Jenkins, Y. Matsutomi, C. Yoon and W. E. Anderson, "Experimental Velocity Profiles in the Cap Shock Pattern of a Thrust Optimized Rocket Nozzle," in *49th AIAA Aerospae Sciences Meeting*, Orlando, FL, 2011.

[20] M. Raffel, C. Willert, S. Wereley and J. Kompenhans, "Image Evaluation Methods for PIV," in *Particle Image Velocimetry: A Practical Guide*, Springer, 2007, pp. 123-176.

[21] Vision Research, "Phantom UHS-12 Series," 2015.

[22] Photron, "FASTCAM SA-X2 High Performance High-Speed Camera System," 2015.

[23] LaVision, "Image sCMOS," 2015.

[24] F. F. J. Schrijer, F. Scarano and B. W. van Oudheusden, "Application of PIV in a Mach 7 Double-Ramp Flow," *Experiments in Fluids,* vol. 41, pp. 353-363, 2006.

[25] J. Haertig, M. Havermann, C. Rey and A. George, "Particle Image Velocimetry in Mach 3.5 and 4.5 Shock-Tunnel Flows," *AIAA Journal,* vol. 40, no. 6, pp. 1056-1060, 2002.

[26] P. Gnemmi, C. Rey, J. Srulijes, F. Seiler and J. Haertig, "Hypersonic Flow-Field Measurements by PIV," in *14th International Symposium on Flow Visualization*, Daegu, Korea, 2010.

[27] Hamamatsu Photonics, "Guide to Streak Cameras," 2008.

[28] H. Hidalgo, R. L. Taylor and J. C. Keck, "Transition in the Viscous Wakes of Blunt Bodies at Hypersonic Speeds," *Journal of the Aerospace Sciences,* vol. 29, no. 11, pp. 1306-1331, 1962.

[29] R. Knystautas, B. H. K. Lee and J. H. Lee, "Transmission of Detonation Waves through Orifices," *AIAA Journal,* vol. 4, no. 2, pp. 365-367, 1966.

[30] F. J. Goldin, B. T. Meehan, E. C. Hagen and P. R. Wilkins, "Time-Resolved Spectra of Dense Plasa Focus using Spectrometer, Streak Camera, and CCD Combination," *Review of Scientific Instruments,* vol. 81, no. 10, 2010.

[31] R. B. Lawhead, "Photographic Studies of Combustion Processes in Liquid Propellant Rockets," *Symposium (International) on Combustion,* vol. 8, no. 1, pp. 1140-1151, 1961.

[32] R. B. Lawhead and L. P. Combs, "Modeling Techniques for Liquid Propellant Rocket Combustion Processes," *Symposium (International) on Combustion,* vol. 9, no. 1, pp. 973-981, 1963.

[33] S. J. Beresh, J. L. Wagner, J. F. Henfling, R. W. Spillers and B. O. M. Pruett, "Temporal Evaluation of Turbulent Eddies in a Compressible Jet in Crossflow Measured using Pulse-Burst PIV," in *45th AIAA Fluid Dynamics Conference*, Dallas, TX, 2015.

[34] M. P. Wernet and A. B. Opalski, "Development and Application of a MHz Frame Rate Digital Particle Image Velocimetry System," in *24th AIAA Aerodynamic Measurement Technology and Ground Testing Conference*, Portland, OR, 2004.

[35] M. Voges, J. Klinner, C. Willert, M. Beversdorff and R. Schodl, "Assessment of Powder-Based Seeding Materials for PIV Applications in Transonic, Supersonic, and Reacting Flows".

[36] M. Gilbert, L. Davis and D. Altman, "Velocity Lag of Particles in Linearly Accelerated Combustion Gases," *Journal of Jet Propulsion,* vol. 25, no. 1, pp. 26-30, 1955.

[37] R. Paschotta, "Laser Diodes," in *Encyclopedia of Laser Physics and Technology*.

[38] H. Sun, "Chapter 2: Laser Diode Beam Basics," in *A Practical Guide to Handling Laser Diode Beams*, Springer, 2015, pp. 27-51.

[39] PerkinElmer Optoelectronics, "High Performance Flash and Arc Lamps".

[40] Excelitas, "Application Notes-Generation of Light by Xenon Discharge".

[41] V. Kostylev, "Chapter 10: Scattering Fundamentals," in *Bistatic Radar: Principles and Practice*, Wiley, 2007.

[42] C. F. Bohren and D. R. Huffman, "Chapter 4: Absorption and Scattering by a Sphere," in *Absorption and Scattering of Light by Small Particles*, Wiley, 2007, pp. 83-129.

[43] I. Malitson, "Interspecimen Comparison of the Refractive Index of Fused Silica," *Journal of Optical Society of America,* vol. 55, pp. 1205-1208, 1965.

[44] A. Zisserman, "2D Fourier Transforms and Applications," [Online]. Available: http://www.robots.ox.ac.uk/~az/lectures/ia/lect2.pdf. [Accessed June 2017].

[45] D. Ballard and C. Brown, in *Computer Vision*, Prentice-Hall, 1982, pp. 24-30.

[46] R. Gonzales and R. Woods, in *Digital Image Processing*, Addison-Wesley Publishing Company, 1991, pp. 81-125.

[47] B. Horn, in *Robot Vision*, MIT Press, 1986.

[48] A. Jain, in *Fundamentals of Digital Image Processing*, Prentice-Hall, 1989, pp. 15-20.

[49] A. Marion, in *An Introduction to Image Processing*, Chapman & Hall, 1991.

[50] Ag2gaeh, Artist, *Hyperbola: Features.* [Art]. 2017.

[51] The MathWorks, Inc., "Bioinformatics Toolbox User's Guide," 2018. [Online]. Available: https://www.mathworks.com/help/pdf_doc/bioinfo/bioinfo_ug.pdf. [Accessed 25 March 2018].

[52] J. D. Willits, J. D. Dennis, A. S. Kulkarni, P. V. Ramachandran and T. L. Pourpoint, "Combustion Characterization of Amine Borane Hypergolic Propellants," in *50th AIAA/ASME/SAE/ASEE Joint Propulsion Conference*, Cleveland, OH, 2014.

[53] C. Willert, G. Stockhausen, M. Voges, J. Klinner, R. Schodl, C. Hassa, B. Schürmans and F. Güthe, "Selected Applications of Planar Imaging Velocimetry in Combustion Test Facilities," in *Particle Image Velocimetry*, Springer, 2008, pp. 283-309.

[54] C. Willert and M. Jarius, "Planar Flow Field Measurements in Atmospheric and Pressurized Combustion Chambers," *Experiments in Fluids,* vol. 33, pp. 931-939, 2002.

[55] J. Dirgo and D. Leith, "Cyclone Collection Efficiency: Comparison of Experimenal Results with Theoretical Predictions," *Aerosol Science and Technology,* vol. 4, pp. 401-415, 1985.

[56] C. J. Stairmand, "The Design and Performance of Cyclone Separators," *Transactions of the Institution of Chemical Engineers,* vol. 29, p. 356, 1951.

[57] W. Barth, "Design and Layout of the Cyclone Separator on the Basis of New Investigations," *Brennstoff-Wärme-Kraft,* vol. 8, pp. 1-9, 1956.

[58] P. Bourgeois and P. Grenier, "The Ratio of Terminal Velocity to Minimum Fluidizing Velocity for Spherical Particles," *The Canadian Journal of Chemical Engineering,* vol. 46, pp. 325-328, 1968.

[59] Phenom-World BV, "Phenom User Manual ProX/Pro/Pure," in *ProX User Manual*, 2013.

[60] N. Garcia, "Power Inductors and Peak-Current Handling Capability," 2012.

[61] D. R. Schmitt, "Development of a 3-D Defocusing Liquid Crystal Particle Thermometry and Velocimetry (3DDLCPTV) System," University of Washington, 2007.

[62] Newport Corporation, "Tutorial: Light Collection and Systems Throughput," [Online]. Available: https://www.newport.com/t/light-collection-and-systems-throughput. [Accessed 16 March 2017].

[63] Sydor Instruments, "ROSS 2000 Operator's Manual Revision C," 2013.

[64] Sydor Instruments, "Test Data Summary: MCP and Streak Tube".

[65] Sydor Instruments, "System #46 Final Data Report: SI-400449," 2014.

[66] Max Levy, "Ronchi Rulings," [Online]. Available: http://www.maxlevy.com/category/ronchi-rulings.html. [Accessed 22 March 2018].

[67] P. Panigrahi and M. Krishnamurthy, "Laser Schlieren and Shadowgraph," in *Schlieren and Shadowgraph Mehods in Heat and Mass Transfer*, Springer, 2012.

[68] I. Malitson and M. Dodge, "Refractive Index and Birefringence of Synthetic Sapphire," *Journal of the Optical Society of America,* vol. 62, p. 1405, 1972.

[69] J. Devore, "Refractive Indices of Rutile and Sphalerite," *Journal of the Optical Society of America,* vol. 41, pp. 416-419, 1951.

[70] D. Wood and K. Nassau, "Refractive Index of Cubic Zirconia Stabilized with Yttria," *Journal of Applied Optics,* vol. 21, pp. 2978-2981, 1982.

VITA

Education: Purdue University, West Lafayette, IN

Ph.D., Aeronautical & Astronautical Engineering, May 2018

M.S., Aeronautical & Astronautical Engineering, Dec 2014

B.S., Aeronautical & Astronautical Engineering, May 2013

Work Experience:

Propulsion Engineer at SpaceX, Hawthorne, CA

April 2018 – Present

Research Assistant at Maurice J. Zucrow Laboratories, West Lafayette, IN

Aug 2013 – April 2018

NASA Space Technology Research Fellow at Marshall Space Flight Center, Huntsville, AL

Aug 2014 – April 2018

NASA Propulsion Academy Team Lead at Marshall Space Flight Center, Huntsville, AL

June 2013 – Aug 2013

Research Interests:

Liquid rocket propulsion

Hypergolic propellant characterization and development

Less-toxic, liquid monopropellants and bipropellants

Diagnostic techniques for combustion applications

PUBLICATIONS

J. D. Willits and T. L. Pourpoint, "Demonstration and Characterization of Particle Streak Velocimetry in Supersonic Nozzle Flows," in *54th AIAA/SAE/ASEE Joint Propulsion Conference*, Cincinnati, OH, 2018. Abstract Accepted.

J. D. Dennis, J. D. Willits and T. L. Pourpoint, "Performance of Neat and Gelled Monomethylhydrazine and Red Fuming Nitric Acid in an Unlike-Doublet Combustor," *Combustion Science and Technology*, published online: 04 Apr 2018.

J. D. Willits and T. L. Pourpoint, "Development of Particle Streak Velocimetry with a Cold Flow Supersonic Nozzle," in *53rd AIAA/SAE/ASEE Joint Propulsion Conference*, Atlanta, GA, 2017.

J. D. Willits and T. L. Pourpoint, "Particle Streak Velocimetry of Supersonic Nozzle Flows," in *63rd JANNAF Propulsion Meeting*, Newport News, VA, 2016, NASA Technical Report Server Document ID 20160007062.

J. D. Willits and T. L. Pourpoint, "System and Method for Measuring Exhaust Flow Velocity of Supersonic Nozzles", USPTO Utility Patent 15/600,700, May 19, 2017.

J. D. Willits, J. D. Dennis, A. S. Kulkarni, P.V. Ramachandran and T. L. Pourpoint, "Combustion Characterization of Amine Borane Hypergolic Propellants", in *50th AIAA/ASME/SAE/ASEE Joint Propulsion Conference*, Cleveland, OH, 2014.

P. V. Ramachandran, A. S. Kulkarni, M. A. Pfeil, J. D. Dennis, J. D. Willits, S. D. Heister, S. F. Son and T. L. Pourpoint, "Amine-Boranes: Green Hypergolic Fuels with Consistently Low Ignition Delays," *Chemistry: A European Journal*, vol. 20, no. 51, pp. 16869-16872, 2014.